Obtaining ultracold molecules through Stark deceleration and laser cooling

Meinema, Jacoba Roelien

Obtaining ultracold molecules through Stark deceleration and laser cooling

rijksuniversiteit groningen

faculteit wiskunde en natuurwetenschappen

van swinderen institute for particle physics and gravity

Nederlandse Organisatie voor Wetenschappelijk Onderzoek

Dit werk maakt deel uit van het onderzoekprogramma van de Stichting voor Fundamenteel Onderzoek der Materie (FOM), die deel uitmaakt van de Nederlandse Organisatie voor Wetenschappelijk Onderzoek (NWO).

ISBN: 978-90-367-8787-1 (gedrukte versie)
ISBN: 978-90-367-8786-4 (elektronische versie)
Druk: Ipskamp Drukkers, Enschede, 2016

rijksuniversiteit
groningen

Obtaining ultracold molecules through Stark deceleration and laser cooling

Proefschrift

ter verkrijging van de graad van doctor aan de
Rijksuniversiteit Groningen
op gezag van de
rector magnificus prof. dr. E. Sterken
en volgens besluit van het College voor Promoties

De openbare verdediging zal plaatsvinden op

vrijdag 13 mei 2016 om 16.15 uur

door

Jacoba Roelien Meinema

geboren op 2 mei 1986
te Groningen

Promotores
Prof. dr. S. Hoekstra
Prof. dr. K. H. K. J. Jungmann

Beoordelingscommissie
Prof. dr. A. M. van den Berg
Prof. dr. B. Noheda Pinuaga
Prof. dr. P. van der Straten

Contents

1 | Introduction

The Standard Model (SM) of particle physics [1, 2, 3, 4, 5, 6] successfully describes the elementary particles of nature and their interactions. The SM provides an excellent description of all confirmed observations, however, it does not provide explanations for many facts that are found. For example, we do not understand the hierarchy of masses of elementary particles, the reason for three particle generations, or the origin of symmetry violations, such as parity violation. Furthermore, it remains to be seen whether dark matter, for which there is strong cosmological evidence, will fit into the framework of the SM with minor modifications to it. Extensions to the Standard Model have been proposed in an attempt to explain the features that are not well understood, such as supersymmetry (SUSY) and many more. String theory tries to include gravity and the SM in one coherent picture [7]. Some observables are predicted to be several orders of magnitude larger in some extensions compared to the SM itself, for example the permanent electron electric dipole moment (eEDM) [8, 9, 10, 11]. The validity of such extensions can be established in precise measurements. Relatively new are precision tests with cold molecules [12, 13]. Alkaline-earth halide molecules are in this context very promising systems due to their particularly suited energy level structures and experimental accessibility.

The most important examples of the use of molecules to test the SM will be described next: parity violation, electron EDM and time variation of fundamental constants. Following this, several possible experimental techniques for achieving cold molecules are discussed. We finish this introduction with an explanation of our chosen experimental approach.

Parity violation

The Standard Model is based on three discrete symmetries: parity (P), time reversal (T), charge conjugation (C), and their combinations (CT, CPT, etc.). All mentioned symmetries are broken, except for CPT. Parity violation is observed because the weak force has an even and an odd parity part. The SM unifies the electromagnetic and the weak force [2, 3, 14]. This unification implies the existence of neutral current interactions via neutral, heavy Z^0 bosons that are only effective at a short range. The Z^0 boson couples not only to the weak charge of fermions but also to their spin: it couples both to vector and to axial-vector currents. Due to the smallness of the weak force, a very sensitive measurement is required. The first observation of parity violation was by Wu et al.[15] in 1957, in the radioactive β-decay of ^{60}Co. Parity violation in the quantum structure of atoms has been an important observation by Bouchiat et al.[16]. When it was established it confirmed that the Standard Model is a powerful description of particle physics at all accessible energy scales. The latest and most accurate measurement has been performed with atomic Cs [17] in 1997 by Wieman et al. Besides measuring the important Weinberg angle ($\sin^2\theta_W$) which determines, e.g., the ratio of the $W^{\pm}$ and Z^0 particle masses, it also identified a new element in the nuclear structure: the anapole moment, that describes toroidal currents of nucleons on the nuclear surface. The parity-violating term scales with the inverse of the energy difference between two states with opposite parity [18, 19]. The parity violation effect can be enhanced by a factor up to 10^5 for molecules compared to atoms, because such effects mix states of opposite parity and in molecules such states can be rather close as compared to atoms in general [20]. In atoms with many electrons [21, 22, 23], and molecules [24, 25], the parity violation effect scales faster than the nuclear charge to the third power. Heavy diatomic molecules are beneficial for a PV measurement due to relativistic enhancements. A possible way to perform a parity violation measurement is the so called Stark interference technique [19, 26]. Currently only one experiment at Yale University has tested the systematics of several rotational level-crossings [27]. This was done in preparation for a parity violation measurement with BaF.

In addition, particularly interesting in molecules is the predicted energy difference between mirror forms of chiral molecules, called enantiomers, that might arise from parity violating effects. Because fluctuations are larger

that those minuscule energy differences, the question has been addressed frequently in the past decades, whether this energy difference might explain the preference of one handedness over the other in for example sugar molecules and perhaps in biological processes [28, 29, 30, 31, 32, 33]. Yet, no convincing conclusion has been reached whether this effect, or just spontaneous symmetry breaking, are primarily responsible for the apparent observed asymmetries.

Electron EDM

The search for the permanent eEDM can be exploited to exclude or confirm theories beyond the SM. The permanent eEDM can only be non-zero if parity and time-reversal invariance are violated. The SM predicts very small values of the permanent eEDM ($\sim 10^{-38}$ e cm), while extensions predict much larger values. Some of the models can already be rejected, others are at the edge of the current experimental limit set on the permanent eEDM. In Figure 1.1 several theoretical predictions are shown together with the current experimental limit. The current best limit is $|d_e| < 8.7 \times 10^{-29}$ e cm with 90% confidence, measured with ThO [13]. The high internal effective electric field of heavy molecules enhances the sensitivity for the permanent eEDM. The advantages of molecules for EDM searches have been appreciated already in 1969 [34]. Recently, molecules have been employed for searches of permanent eEDMs with YbF [12] ($|d_e| < 10.5 \times 10^{-28}$ e cm) and ThO [13]. Also experiments with molecular ions such as HfF^+ in ion traps are challenging measurements with neutral systems and have reached results within one order of magnitude of the record [35]. Measuring the permanent eEDM on molecules is not new [36], but due to relatively new cooling techniques this is very promising for the future. For the permanent eEDM measurement with YbF the plan is to increase the interaction time by using colder molecules and a vertical beam arrangement resulting in a molecular fountain [37]. For this experiment laser cooling is essential to increase the phase space density of the molecular beam.

Time variation of fundamental constants

The SM has free parameters whose value can only be determined by measurements. Theories that unify gravity with the other interactions are extensions to the SM [7, 39, 40]. Some extensions of the SM predict variation

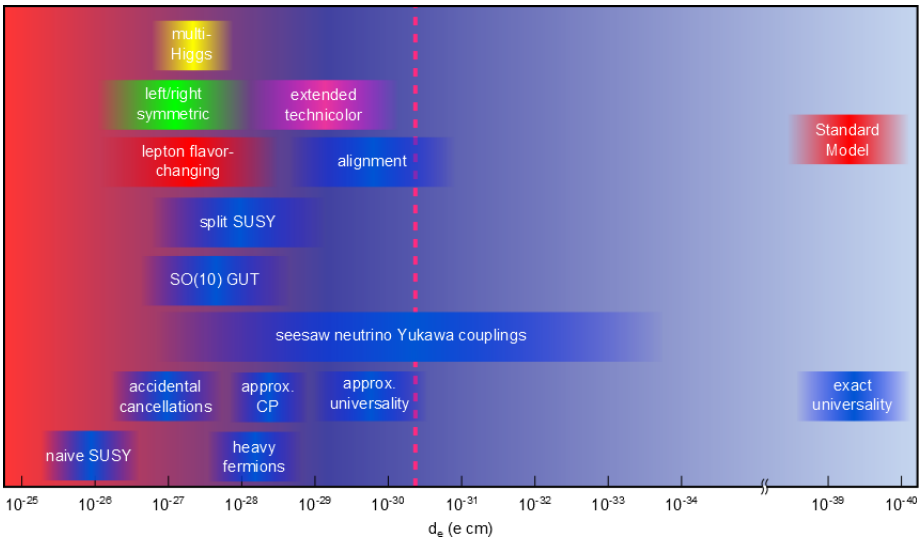

Figure 1.1: *The predictions of the permanent eEDM from several theories. The red area is excluded by the ThO measurement [13], the dashed line is the accuracy of the proposed experiment with the YbF fountain [37]. The picture is based on an original version of DeMille [38].*

in time or in space of some of the 'constants'. The idea of varying constants dates back to Dirac, who suggested that the gravitational constant might vary on basis of a model that assumes a dimensionless universal constant [41].

Two possible ways to look for a variation of constants are mostly exploited: observations of the red-shifted spectra of stars in the early universe and time dependent precision measurements in the energy level structure of atoms or molecules. Examples of dimensionless constants that can be investigated using molecules are the fine-structure constant $\alpha = e^2/4\pi\epsilon_0\hbar c$, which characterizes the strength of the electromagnetic interaction, and the electron-to-proton mass ratio $\mu = m_e/m_p$, which characterizes the strength of strong interactions with respect to electroweak interactions. Molecules with accidental degeneracies between rotational levels are very sensitive for variations in μ. Amongst others, the group of Bethlem of the VU university

in Amsterdam is preparing a very precise measurement with cold ammonia molecules to measure possible time variations in μ [42, 43].

1.1 Precision measurements

Compared to atoms, molecules are often more sensitive probes for precision measurements to test the SM, due to their internal level structure and associated rather large enhancements in sensitivity to a variety of observables that could indicate new physics. An example is the search for permanent electric dipole moments on the electron and other elementary particles, because close proximity of molecular states of opposite parity causes in some molecules the highest possible enhancements of the sensitivity that have been identified so far [8]. For ultimate precision, excellent control over the molecules is beneficial: a long interaction time of the measurements boosts the measurement accuracy and a very well defined electric and magnetic field is easier to achieve for a smaller interaction zone. Also important is that all molecules can be prepared in the same quantum state. For precision measurements which exploit spin precession in external fields, the statistical uncertainty of one single measurement is

$$\sigma \propto \frac{1}{\xi\tau\sqrt{N}}, \tag{1.1}$$

where ξ is the sensitivity of the system, τ is the coherent interaction time and N the number of detected molecules in the experiment. The factor ξ depends on details of particular experiments such as the polarization of the sample and external electric fields that are applied, as well as on enhancement factors which may exist in composed systems. The number of detected molecules depends on the density of the molecules as well as on their temperature. A combination of these two quantities is called the *phase space density*. In order to increase the phase space density, full control over the velocity is beneficial, preferably that molecules are trapped. Another option is a slow beam of molecules with low transverse velocity, for example in a fountain [37, 42, 43]. Also, in (slow) beam experiments the molecules need to be cold, for keeping a large density. During the past 15 years many techniques have been developed to control, decelerate, and/or cool molecules. However, this issue remains a challenge, especially for the molecules that are best suited to test the SM.

The goal of our experiments is to prepare sensitive molecules for tests of the SM. Our experimental approach is a combination of traveling-wave Stark deceleration [44] and laser cooling [45, 46]. The most interesting molecules for parity violation (PV) and eEDM tests are heavy diatomic molecules [47]. Heavy molecules need a long traveling-wave Stark decelerator for slowing down to standstill. We have chosen SrF because this molecule is bridging the gap between light molecules that can be Stark decelerated and heavy molecules where the enhancement factors are large. SrF has an intrinsic electric dipole moment of 3.5 Debye (D) and a decelerator of 5 meter length is required to decelerate them from 300 m/s to standstill [48]. SrF can also be laser cooled in order to reduce the velocity spread after the decelerator even more. This is not self-evident for molecules. Figure 1.2 shows the masses for decelerated light molecules, SrF, and heavy molecules on which precision tests have been performed [13, 49, 50] or are proposed [27, 37, 51].

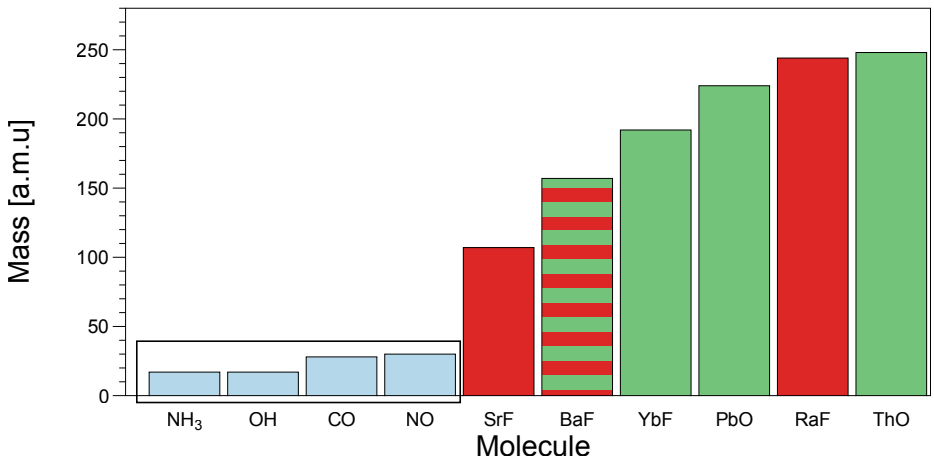

Figure 1.2: *The masses of several molecules. The lighter molecules (in the box) have been decelerated and stopped by a multistage Stark decelerator [42, 43, 54, 55, 56], the heavier molecules (>100 amu) have a large enhancement factor for parity violation tests (red) and eEDM tests (green). The mass of SrF is in the middle of the decelerated and stopped molecules and the heavier molecules. SrF [57] and YbF [58] have been decelerated but not yet stopped in a traveling-wave Stark decelerator.*

Deceleration of the molecules in a Stark decelerator does not increase the phase space density [47, 52]. Laser cooling at the end of the decelerator, however, does. Longitudinal laser slowing of the fast beam directly after the source is accompanied by large losses due to the transverse velocity spread [53]. The final number of molecules that could be stopped is therefore limited. The combination of a traveling-wave decelerator with laser cooling solves the problem of the transverse losses, since during the deceleration the molecules are kept together by the electric fields of the decelerator. A final, short storage of laser cooling can reduce the temperature with minimal extra losses.

1.2 Experimental techniques for making cold molecules

There are various techniques to prepare cold and/or slow molecules [20, 59]. All (current) techniques have their own advantages and disadvantages, and can only be used for a selected group of molecules. In Figure 1.3 an overview of the several techniques and possible applications are shown for a range of temperatures and densities.

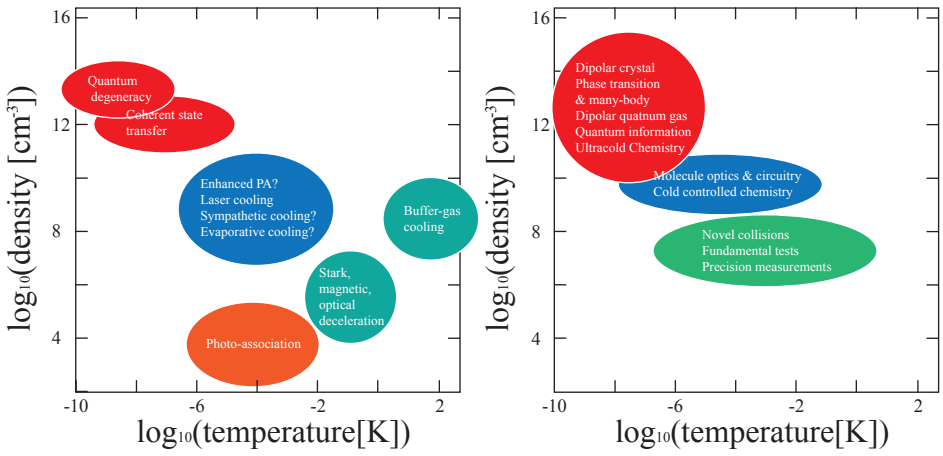

Figure 1.3: *An overview of the techniques to make cold molecules with a certain temperature and density compared to the applications. This picture is adapted from [20].*

1.2.1 Beams of internally cold molecules

Samples of molecules in the gas phase are usually at room temperature. Or, if free radicals are of interest, they have to be created at the moment of the experiment, for example by laser ablation. At the corresponding temperatures most molecules are not in the rovibrational ground state. The fraction of molecules in the ground state can be increased by cooling the beam of molecules, for example by supersonic expansion or a cryogenic buffer gas cell.

Supersonic expansion

In a supersonic expansion, a carrier gas, usually a noble gas, is expanded from a high pressure reservoir into the vacuum. During this expansion the gas gains a high forward velocity (a few hundred m/s) and cools down internally. Molecules can be picked up by the carrier gas. Through collisions with the carrier gas the molecules obtain the same forward velocity and are cooled internally. The lowest velocity is obtained for a heavy carrier gas and a cooled valve [60]. Free radicals can be injected into the expanding beam by laser ablation off a solid target close to the nozzle of the valve. The size of the molecular packet is determined by the ablation spot and the velocity spread of the beam. The size is typically a few millimeter. The transverse velocity is around 10% of the forward velocity. The forward velocity is much higher ($\sim$ 300 m/s) compared to cryogenic buffer gas cooling. Supersonic expansion can be combined with Stark [57] or Zeeman decelerators, due to the small longitudinal size of the molecular packet. The combination with laser cooling is not very successful due to the high longitudinal velocity.

Cryogenic buffer gas cooling

Another method for producing a beam of slow molecules uses a cryogenic buffer gas cell [61]. Molecules are produced in a buffer gas cell and thermalize through collisions with cold He atoms. The molecules escape through a small opening in the cell. This produces a cold molecular beam with a temperature of a few Kelvin with a high flux density ($10^{15}/\mathrm{cm}^3$) and low velocity ($\sim$ 60 – 150 m/s) [62], with a transverse velocity around 30 m/s. Smaller transverse velocity spreads, 15 % of the forward velocity [45], are possible with higher forward velocities (200 m/s). The duration of such a

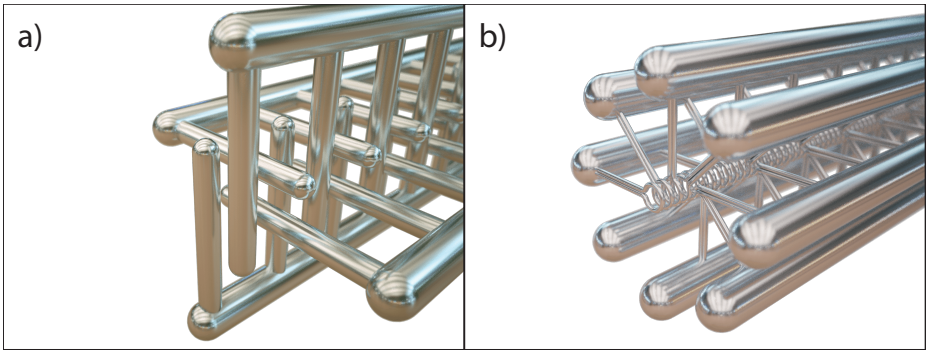

Figure 1.4: *The configurations of a traditional Stark decelerator (left) and a traveling-wave Stark decelerator (right).*

pulse is rather long, 5 ms or $\sim 0.3 - 0.8$ m. In a Stark or Zeeman decelerator the molecules are spread out longitudinally and deceleration works less efficiently. Such a beam can however be combined with laser cooling [45] very well.

1.2.2 Stark deceleration

Stark decelerators, not surprisingly, make use of the Stark effect to remove the kinetic energy from a packet of molecules. Figure 1.4 shows a traditional Stark decelerator and a traveling-wave Stark decelerator. The Stark decelerator has electrodes to which high voltages can be applied. Polar molecules have an intrinsic, body-fixed dipole moment that interacts with an external field. If a beam of molecules feels the electric field of the electrodes, the molecules in the low-field seeking state are decelerated.

In the traditional form, the Stark decelerator consists of electrode pairs placed left/right and up/down to focus the molecules. When the low-field seeking molecules reach the center of an electrode pair, the voltage is switched to the next pair of electrodes. The electric field gradient inside the decelerator can be used to decelerate molecules. A repetition of this procedure can decelerate light molecules such as OH very efficiently, typically from ~ 300 m/s to ~ 100 m/s in one meter. Lower end velocities are possible but losses are relatively high due to the over-focusing effects [63, 64]. Such decelerators are particularly suited for light molecules with

(large) electric dipole moments, i.e. a large Stark shift at the low-field seeking states. Examples of decelerated molecules are: CO [54], NH_3 [42, 43], NO [55], NH [65], OH [56] and CH_3F [66]. This technique has enabled a new generation of high-resolution (cold) collision experiments [67, 68].

For the deceleration to standstill of heavy molecules that starts at the same velocity, a longer decelerator is required. Besides the mass, the Stark shift for the lowest rotational states exhibits a turning point at relatively low electric field strengths. As a result, only a small force can be applied to these molecules. For this reason, if one were to use use a traditional Stark decelerator for such molecules the achieved number of cold molecules would be very small.

The solution to these challenges is the use of a traveling-wave Stark decelerator, which is a central part of our experimental approach, to produce cold molecules for precision experiments. The traveling-wave Stark decelerator consists of a long series of ring-shaped electrodes. A sinusoidal high-voltage can be applied to the electrodes. Thereby a three dimensional trap is created for molecules in low-field seeking states. The high voltages vary in time. Initially the electric trap is given the same speed as the molecules, and when the trap is slowed down, the molecules are decelerated. This type of Stark decelerator is stable till standstill and there are no losses due to the exposure to high electric fields. More details are given in [42, 43, 57, 69, 70] and section 4.2.

1.2.3 Zeeman deceleration

Besides electric fields, also the interaction with magnetic fields can be used to decelerate molecules [71, 72]. Molecules with a magnetic dipole moment but not necessarily an electric dipole moment, can be decelerated with a Zeeman decelerator. Examples are O_2 [73, 74], and CH_3 [75].

1.2.4 Laser slowing and cooling

Laser slowing and cooling is based on the transfer of momentum during the repeated absorption and emission of photons. With the absorption of photons, momentum is transferred to the molecules. During the following spontaneous emission step, photons are emitted in random directions. The

net momentum transfer in the repetition of this absorption-emission cycle therefore results in a net force on the molecules in the direction of the laser beam.

As long as the molecules decay to a state that can be resonantly excited by laser light, the scattering process removes kinetic energy from the molecules. Laser slowing causes a large velocity spread in the transverse direction. Barry et al.[53] slowed down SrF molecules from 140 m/s and only 6% of the molecules was slowed below 50 m/s in 10^4 photon scatterings.

For laser cooling in a process called optical molasses, two counter-propagating laser beams are used, slightly red-detuned from a resonant transition. Due to the Doppler effect the scattering force in the direction opposite to the velocity is stronger than the force in same direction as the velocity. The scattering force therefore reduces the molecular velocity in the cooling axis until the random nature of the absorption and emission processes prevents further removal of energy, at which point the Doppler temperature is reached.

By applying a spatially varying magnetic field in combination with properly chosen laser light polarization, the laser cooling force can also be made position dependent. This is the basis of the magneto-optical trap. Laser cooling of atoms is a powerful technique that has been used to reach record-low temperatures, far below the Doppler limit mentioned above, culminating in the creation of a new state of matter, the Bose-Einstein Condensate [76].

As it turns out, most molecules are not suitable for laser cooling: besides electronic states they also have long-lived rotational and vibrational states to decay to, and during the development of atomic laser cooling there were no attempts to even try to do molecular laser cooling. However, in 2004 DiRosa [77] was the first to suggest that laser cooling might be possible for a select number of diatomic molecules with highly diagonal Franck-Condon (FC) factors. A highly diagonal FC factor indicates a relatively small branching ratio (at best on the order of 10^{-3}) to other vibrational states, allowing to keep the molecules in a closed cooling cycle for some time. Soon after, Stuhl et al.[78] showed that, by exploiting selection rules for specific electronic transitions, in such molecules a cooling cycle can be

created without leaks to rotationally excited states. By making use of two repumping lasers to keep the molecules in the lowest three vibrational states, it became clear that selected molecules can be kept in the absorption-cooling cycle for $\sim 10^4$ photons scatterings, which is enough to be cooled.

In recent years experiments have been started on the laser cooling of several molecules: SrF [45, 53, 79], YO [80] and CaF [81]. Recently the first magneto-optical traps have been realized with YO (2D) [80] and SrF (3D) [46, 82, 83].

1.2.5 Single-photon cooling

A conceptually different way in which laser light can be used to remove energy from molecules is single-photon cooling. In contrast to the laser cooling as described above, where small recoil kicks from the absorption of photons in the laser cooling lead to a net force, here a large amount of kinetic energy is removed in a single photon absorption and emission step. This is done by optically pumping the molecules, in the presence of an external electric or magnetic field, from a state with a large energy shift to a state that experiences a much smaller energy shift in the external field. The single photon that is emitted following the excitation step can therefore carry away a large amount of kinetic energy [84, 85, 86]. A rather general implementation of this principle that can be applied to molecules with a particular electronic structure has been demonstrated by Zeppenfeld et al.[86]. CH_3F molecules are electrically trapped, such that the potential energy depends on the position of the molecule. Using infrared laser light, the trapped molecules are vibrationally excited, from which they will subsequently decay to a number of lower lying rotational states. If the trapped molecules are at the position where an externally applied electric trapping field is high, the rotational energy splitting is large and stimulated emission pumps them to the lower rotational level. When the molecules return to the trap center, which is provided with an homogenous electric field, they have lost kinetic energy. Figure 1.5 shows the energy shifts of the used levels as a function of position. The energy removed per cycle is relatively large, so only a few cycles are required to cool the sample by a factor 13.5 to reach a temperature of 29 mK. Since the vibrational lifetime is long compared to the electronic lifetime, the cooling rate is modest. The loss of molecules per cycle is about 10% [87].

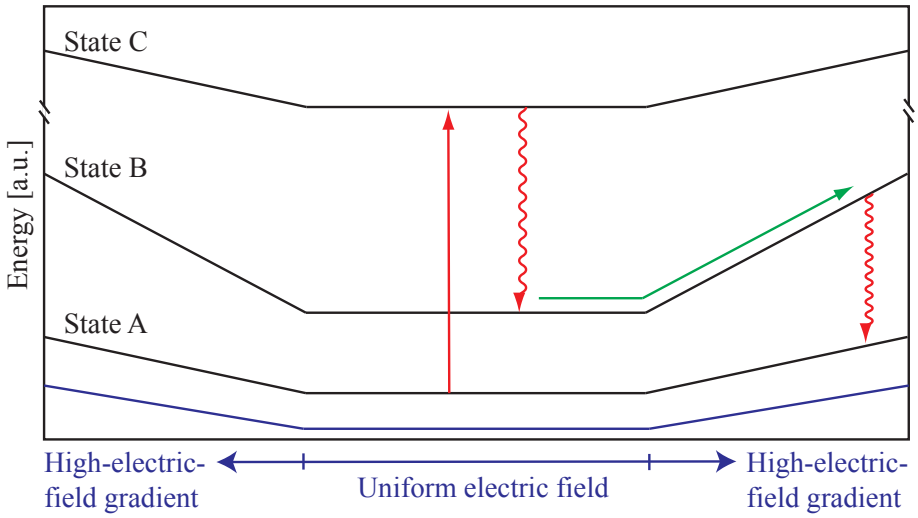

Figure 1.5: *The position dependent energy levels for opto-electric cooling. Molecules climb up the hill in the high-electric field region and decay. The net Stark shift in state B is higher than in ground state A so the molecule has lost kinetic energy. This picture is adapted from [87].*

1.2.6 Sympathetic and evaporative cooling

In sympathetic cooling a sample of molecules is cooled through collisions with a cold atom cloud. The lowest possible temperatures are predicted to be in the $\sim 100\mu$K regime [88, 89]. In practice it is still a challenge because the internal state of the molecules can change by collisions. For high enough densities the temperature of the sample can be decreased further by evaporative cooling [90]. If the potential of the trap decreases, molecules with high velocities can escape and this is experimentally done by Stuhl et al.[91] in combination with a Stark decelerator. The molecular sample has been cooled to 5.1 mK. The velocities of the left-over molecules will be redistributed and this results in a lower temperature for them if the potential is decreased very slowly. The goal is to produce quantum degenerate gasses with strong dipolar interactions [92]. These two collisional cooling schemes have two requirements: the thermalization should be faster than the trap lifetime, i.e. the density has to be high enough. Because the sample is already cold, collisions are also less probable. As a second requirement the inelastic collision rate should be small. This can cause a problem because

most of the traps (electric and magnetic) make use of low-field seeking states, which are not the absolute ground state.

1.2.7 Photo-association of cold atoms

An indirect method of creating cold molecules is to start with cold atoms and to bind them into molecules. Only a limited range of atoms can be cooled and trapped to ultracold temperatures, mostly alkali atoms. In this process, called photo-association, atoms in an unbound state absorb a photon and are transferred to a molecular bound (excited) state. Another method uses Feshbach resonances. The energies of the bound and unbound states become equal due to a magnetic field and the scattering length changes. The atom pair can be driven into the (loosely) bound molecular state [59]. An effective method to obtain molecules in the ground (or deeply bound) state is via Stimulated Raman Adiabatic Passages (STIRAP): by stimulated emission the molecules decay into a deeply bound state. This was the first method to reach temperatures below 1 mK [93].

1.2.8 Molecular ions

Molecular ions are easy to trap due to their charge. Temperatures less than 100 mK are achieved by sympathetic cooling of laser-cooled atomic ions in a trap [94, 95]. It is a challenge to cool the internal states. Due to the Coulomb interactions the molecules do not have inelastic collisions with the atomic ions but there might be collisions with neutral gas atoms. Because the trapping time is large, spontaneous decay to lower vibrational levels is also possible. Precision measurements to test for example parity violation, can benefit from the long trapping time [96, 97].

1.3 Applications

Besides testing fundamental interactions and measuring molecular properties, cold molecules can be exploited in a wider area of scientific fields.

1.3.1 Cold and controlled chemistry

A Stark or Zeeman decelerator, or a combination of the two, can create an almost perfect quantum state purity, a tunable velocity and a narrow

velocity distribution [98]. Chemical reactions at ultralow collision energies can be studied. In the ultracold domain (μK) quantum phenomena will dominate chemical reactions and collisions. This leads to new quantum phenomena and control possibilities [99].

1.3.2 Quantum information processing

Due to their electric dipole moment and long-living rovibrational states, (ultra)cold polar molecules can be used for quantum information processing [100]. Molecules can be trapped in an optical lattice and the long-range dipole-dipole interactions can be used as quantum memory for quantum computing.

1.4 Experimental approach

Our experimental approach to make a cold sample of molecules is a combination of traveling-wave Stark deceleration and laser cooling. SrF molecules are formed in a source chamber. They leave the chamber through a skimmer as a molecular beam. Due to cooling in a supersonic expansion, a large fraction of the molecules will be in the lowest rovibrational state. We decelerate these molecules with a traveling-wave Stark decelerator and we are planning to apply laser cooling to reduce the temperature further. We are using SrF because of its predicted sensitivity as a probe for parity violation effects and because it is amenable to the techniques we are using. A schematic overview of the complete setup is shown in Figure 1.6.

In the source chamber a powerful Nd:YAG-laser ablates different kinds of molecules, ions and atoms, including SrF, from a tablet of SrF_2. Together with xenon gas a pulsed molecular beam is formed which expands into the decelerator chamber. If the valve for the Xe gas is cooled, the beam velocity can be lowered to typically 300 m/s. The traveling-wave decelerator slows down a fraction of the molecules from 300 m/s to a computer-programmable end velocity. When decelerating to standstill, this should result in a trapped sample at a temperature that corresponds to 150 mK. The temperature can be reduced further when laser cooling is applied after the decelerator.

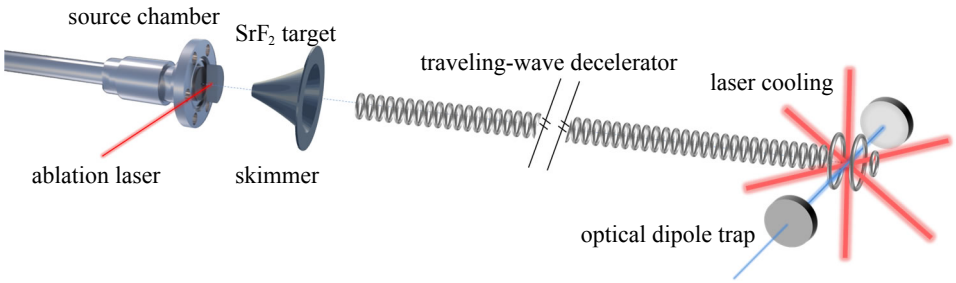

Figure 1.6: *A schematic overview of the setup to decelerate and trap SrF.*

A problem of directly laser cooling a fast beam of molecules is that the scattering force is relatively weak and many photons have to be scattered in random directions. This results in a divergent beam [53, 79]. By combining Stark deceleration with laser cooling, the sample of molecules at standstill is already cold when we start laser cooling. The transverse velocity due to the decelerator acceptance is small (max. 2 m/s) and molecules have to scatter only $\sim 3 \times 10^3$ photons in ~ 1 ms to reach the Doppler temperature. With this rather small number of cycles, we only need one repump laser for molecules that decay to the first vibrational states. The loss to other vibrational states is negligibly low, namely $\sim 7.2\%$ (see Chapter 3).

After laser cooling we aim to trap the molecules in an optical dipole trap, which creates an environment that is especially well suited for precision measurements. It is however a major challenge to load the molecules into the small volume of the dipole trap [101], a process for which a compression stage, such as offered by a magneto-optical trap, is probably required.

1.5 Thesis outline

In view of the background sketched in this chapter we have been setting up an apparatus for producing, slowing and cooling molecules, in particular SrF, in a traveling-wave Stark decelerator. We describe in Chapter 2 the properties of molecules in general and of SrF in particular as far as they are relevant for our purpose. In Chapter 3 we describe laser cooling in multilevel systems. Here in particular laser cooling of SrF is discussed with its

strengths and principal limitations. Chapter 4 describes the experimental setup in detail. We have employed this machine for deceleration of SrF and we report the achieved results. Further, we present the design of a separate trap at the end of the decelerator. Our description includes the laser system that has been set up to generate the necessary light for the laser cooling as well as the measurements of the deceleration of molecules. In Chapter 5 we present the results of experiments and calculations that were performed in order to achieve a higher yield of low field seeking states. In Chapter 6 we summarize and we provide an outlook towards precise measurements with cooled molecules at rest.

2 | Molecular properties

In this chapter the properties of molecules in general and of SrF in particular are described with emphasis on their relevance for decelerating them and cooling them. SrF has almost closed vibrational transitions and closed rotational transitions, which makes this molecule suitable for laser cooling. The electronic, vibrational, rotational and the hyperfine states of SrF are described. The transitions between the states that are exploited for laser cooling are discussed and the influence of magnetic and electric fields on the levels is given.

2.1 Molecular structure

The energy levels of a diatomic molecule can be described by the Born-Oppenheimer approximation [102, 103]. This model separates the wave function of electrons (fast) and the nuclei (relatively slow). Also the rotational motions occur relatively fast compared to the vibrational motion. Typical energy splittings of the electronic states are $\sim 10^{-5}$–10^{-6} cm^{-1}. The energy spacing of vibrational levels is in the order of $\sim 10^{-3}$–10^{-4} cm^{-1} and the rotational energy splitting is in the order of 0.1–10 cm^{-1} [102]. From now on I will call the electronically excited state the excited state and the electronic ground state the ground state. In Figure 2.1 the energy levels of a typical diatomic molecule are schematically depicted.

Molecules can vibrate in these electronic states like an anharmonic oscillator. Rotational states act like a rigid rotor with perturbations. This is described in some textbooks [102, 103, 104].

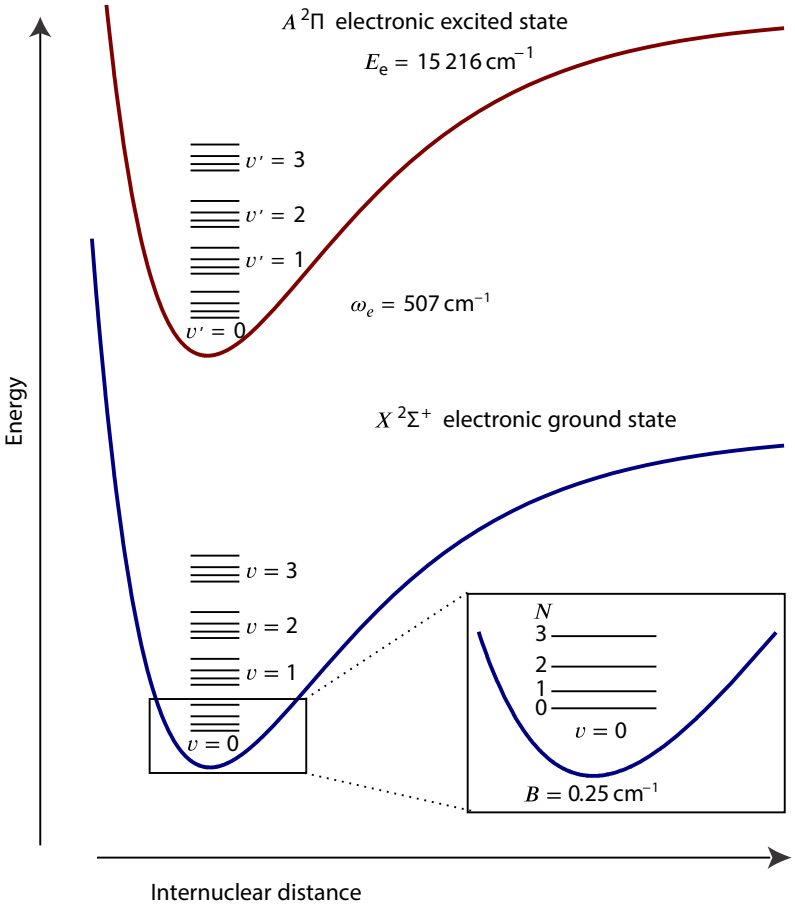

Figure 2.1: *A schematic representation of the ground and an excited state of a diatomic molecule, for example SrF. Vibrational (v) energy differences are significantly smaller than electronic energy differences. Rotational energy differences are much smaller than vibrational energy differences.*

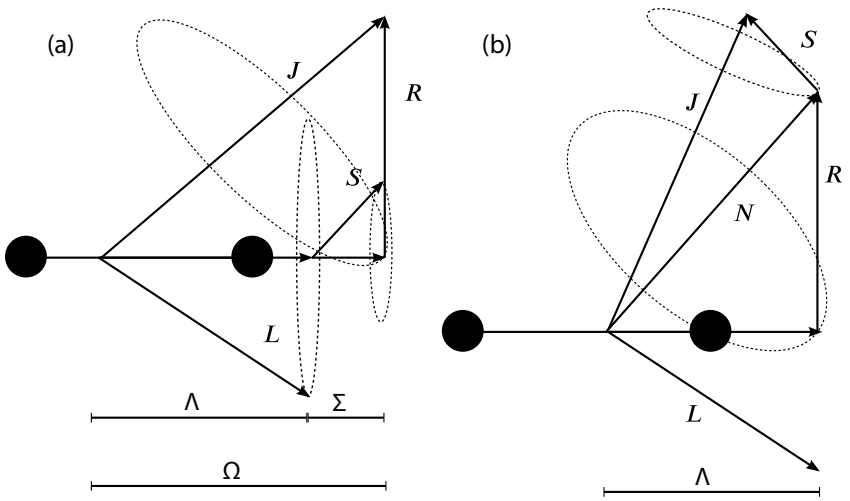

Figure 2.2: *a) Hund's case a and b) Hund's case b for the excited state and the ground state of SrF respectively. The angular momenta quantum numbers are explained in the text.*

Like atoms, molecules have orbital angular momentum $\vec{L}$, total electron spin $\vec{S}$ and nuclear spin $\vec{I}$. Molecules have a quantized rotation, labeled $\vec{R}$. For diatomics there is one molecular axis. The projections of $\vec{L}$ and $\vec{S}$ on the molecular axis are called Λ and Σ, respectively. There are several ways for angular momenta to couple to each other. The Hund's cases [103] are the most general coupling schemes.

The ground state $X^2\Sigma^+$ of SrF is best described by Hund's case b). The excited state $A^2\Pi_{1/2}$ is best described by Hund's case a) [104]. The couplings are shown in Figure 2.2. In the ground state $\vec{R}$ and $\vec{\Lambda}$ couple to form $\vec{N}$ ($\vec{N} = \vec{R} + \vec{\Lambda}$). $\vec{N}$ and $\vec{I}$ couple to form $\vec{J}$ ($\vec{J} = \vec{N} + \vec{S}$). The nuclear spin of $^{88}Sr^{19}F$ comes from the ^{19}F-atom. The nuclear spin is $I = 1/2$ and this couples $\vec{J}$ to $\vec{F}$ ($\vec{F} = \vec{J} + \vec{I}$). For laser cooling we use the $N = 1$ rotational state. This splits into two J-states ($J = 3/2, 1/2$) and four hyperfine states ($F = 2, 1$ for $J = 3/2$ and $F = 0, 1$ for $J = 1/2$). The parity is even for even N and odd for odd N. Figure 2.3 shows the level structure of the ground state.

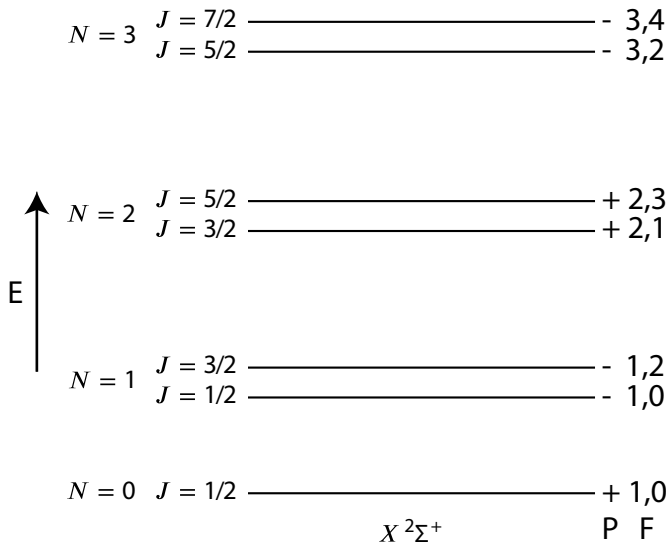

Figure 2.3: *Rotational states with (hyper)fine splitting in the ground state of SrF.*

In the excited state all quantum numbers are primed. The first excited state of SrF is the $A^2\Pi_{\Omega'}$. Here Π indicates $\Lambda = 1$. Ω' is the result of the coupling between Λ' and Σ' and can be parallel ($\Omega' = 3/2$) and anti-parallel ($\Omega' = 1/2$). We focus on $\Omega' = 1/2$ because this is used for laser cooling. Ω' and R' couple to J' ($\vec{J'} = \vec{\Omega'} + \vec{R'}$). J' and I' couple to F' ($\vec{F'} = \vec{J'} + \vec{I'}$). For laser cooling the level $J' = 1/2$ is used with $F = 0, 1$. These hyperfine levels are close together ($\sim$ 3 MHz) so the states are unresolved by the natural linewidth ($1/2\pi\tau$, where τ is the natural lifetime) of the transition. Figure 2.4 shows the level splitting of the excited state.

In the case of $^{87}Sr^{19}F$, both nuclei have a nuclear spin. ^{87}Sr has a nuclear spin of I_{Sr}=9/2. For low rotational numbers, the nuclear spin of Sr couples to S [105]. I_F is only weakly coupled to the system, so the quantum numbers will be:

$$S + I_{Sr} = G; N + G = F_1; F_1 + I_F = F. \tag{2.1}$$

The energy difference for the intermediate quantum number G, with $G = 4$ and 5, is almost 0.1 cm^{-1}. For $N = 0$ there will be 4 hyperfine states, for

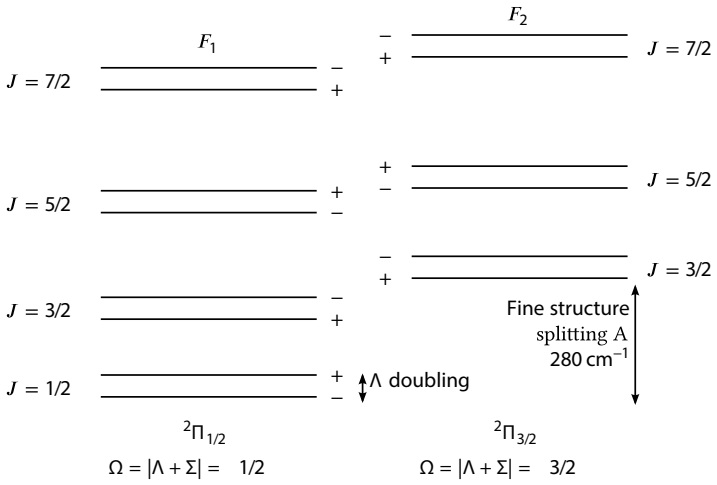

Figure 2.4: *The rotational states with (hyper)fine splitting for the excited state of SrF.*

$N = 1$ there will be 8. The hyperfine states of the lowest rotational states in the ground and excited states are shown in Figure 2.5

2.2 Transitions between levels

The interaction of photons and molecules is mainly described by the matrix elements of the electric dipole operator. The electric dipole operator d_{ij} depends on a radial and angular part [106]

$$d_{ij} = eR_{F',m'_F,J,F,m_F} I_{F',m'_F,J,F,m_F}, \tag{2.2}$$

where e is the electron charge. The radial part R_{F',m'_F,J,F,m_F} depends on the overlap in wave functions and determines only the magnitude of the coupling. The angular part I_{F',m'_F,J,F,m_F} is only non-zero if the polarization of the light can couple to the angular momentum of that state. The selection rules follow from this.

2.2.1 Vibrational states: Franck-Condon factors

Molecules in the excited state and vibrational state v' can decay to any vibrational state v in the ground state. The probability of which v it de-

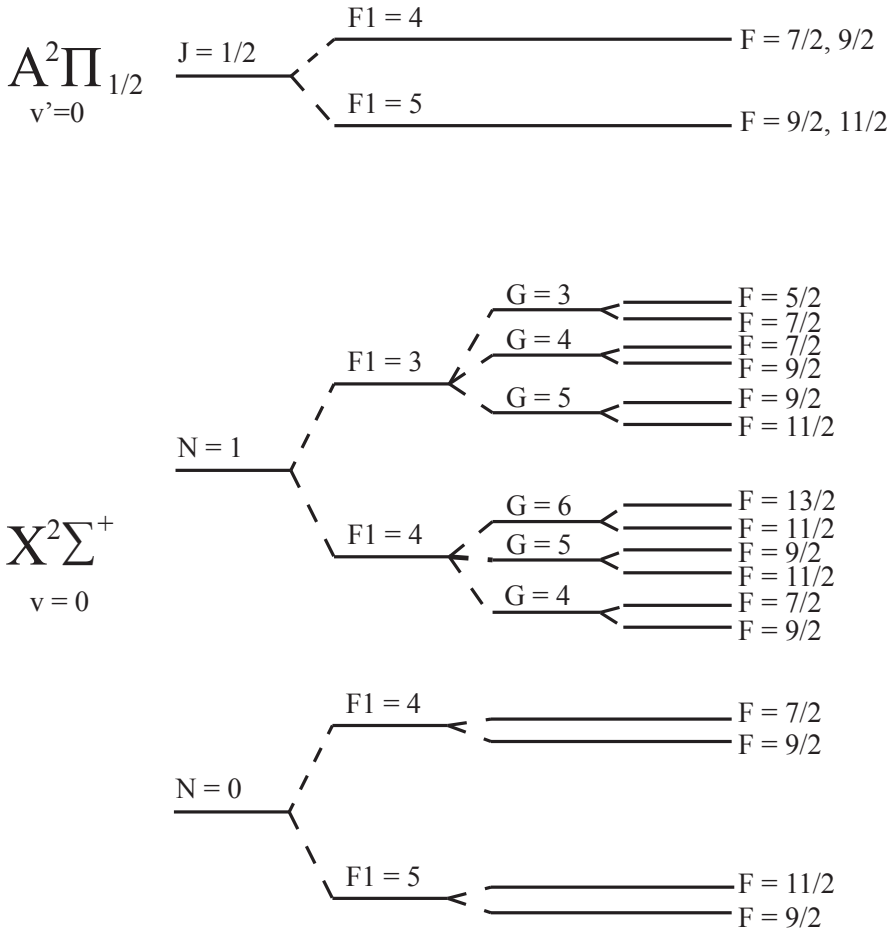

Figure 2.5: *Schematic overview of the hyperfine splitting of the lowest rotational levels in the ground and excited state of* $^{87}Sr^{19}F$.

cays to depends on the overlap of wave functions (Ψ) between v' and v. The Franck-Condon factors are defined as $q_{v',v} = |\langle\Psi(v')|\Psi(v)\rangle|^2$ Combined with the energy difference ($\omega_{v',v}$) this gives the vibrational branching ratio:

$$f_{v',v} = \frac{q_{v',v} \cdot \omega^3_{v',v}}{\sum_k q_{v',k} \cdot \omega^3_{v',k}} \tag{2.3}$$

For some molecules, for example SrF, the potentials of the ground and excited state are similar. One of the two valence electrons in Sr is attracted to the electronegative fluorine nucleus. The second electron will be mostly ($> 96\%$) around the Sr-atom [107]. The system is highly ionic. In the excited state it has a high probability to decay to the same vibrational state: 98 % of the molecules in the $v' = 0$ decay to the $v = 0$, only 2% to the $v = 1$ and 4 $\times 10^{-4}$ to the $v = 2$. The relevant Franck-Condon factors are shown in Figure 2.6 [45]. Due to the highly diagonal Franck-Condon factors of SrF an almost closed vibrational transition can be made with a limited amount of (re)pump lasers.

2.2.2 Rotational levels: selection rules

For laser cooling also a closed rotational transition is required. Due to the parity and selection rules there are some transitions where only one or a few decay possibilities are allowed. In general for molecules the selection rules for an electric dipole transition are: $\Delta J = 0, \pm 1$, and the parity of the wave function has to change sign. Figure 2.7 shows all possible transitions for $A^2\Pi \rightarrow X^2\Sigma^+$, $v' = 0 \rightarrow v = 0$ for the lowest rotational states. Magnetic dipole and electric quadrupole transitions are less probable. Their selection rules are different and can cause leaks in the laser cooling system.

2.2.3 Allowed rotational transitions for SrF

For SrF a closed transition can be made when the excited state has $J' = 1/2$ with positive parity and molecules can only decay to the $N = 1$ state with negative parity. The decay time is 24 ns [45]. The closed transition is shown in Figure 2.8.

The chance that a molecule in state $L'S'J'F'M'_F$ decays to state $LSJFM_F$ is determined by the Hönl-London factors. It can be calculated by the 6j symbols [106]. J.F. Barry has calculated them [108] and the ratios are

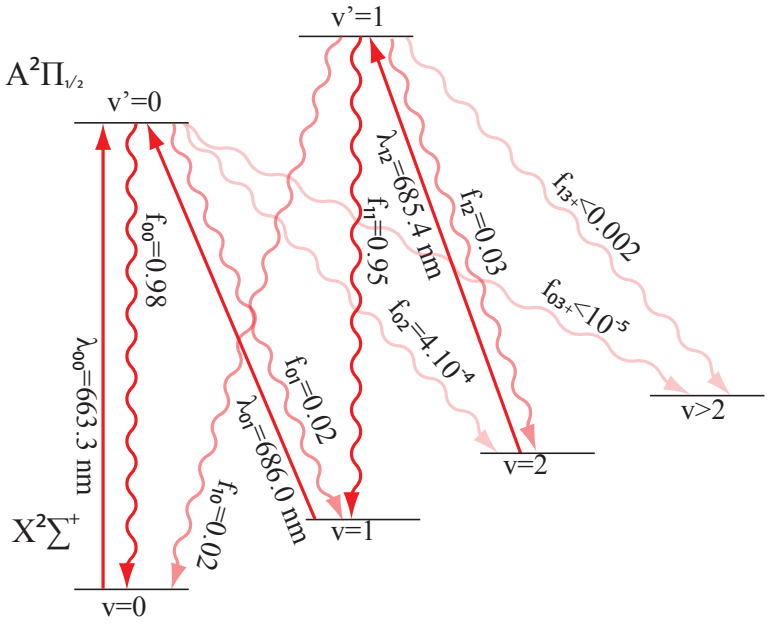

Figure 2.6: *The highest Franck-Condon factors of the vibrational states $v' = 0$ and $v' = 1$ for the SrF molecule [45].*

shown in Table 2.1. All possible electric dipole transitions are shown in Figure 2.7. The hyperfine splittings in the higher vibrational levels are slightly different and can be found in [108].

2.3 Transitions in other molecules

We have explained the properties of the $A^2\Pi \rightarrow X^2\Sigma^+$ transition, in particular for those in SrF. There are more molecules which are suitable for laser cooling and some of these molecules have other electronic transitions than SrF. In this section the selection rules for rotational decay for other molecules with highly diagonal Franck Condon Factors are discussed. There are no selection rules for the vibrational decay. In Chapter 3 about laser cooling there is a list of molecules with properties that are relevant for laser cooling.

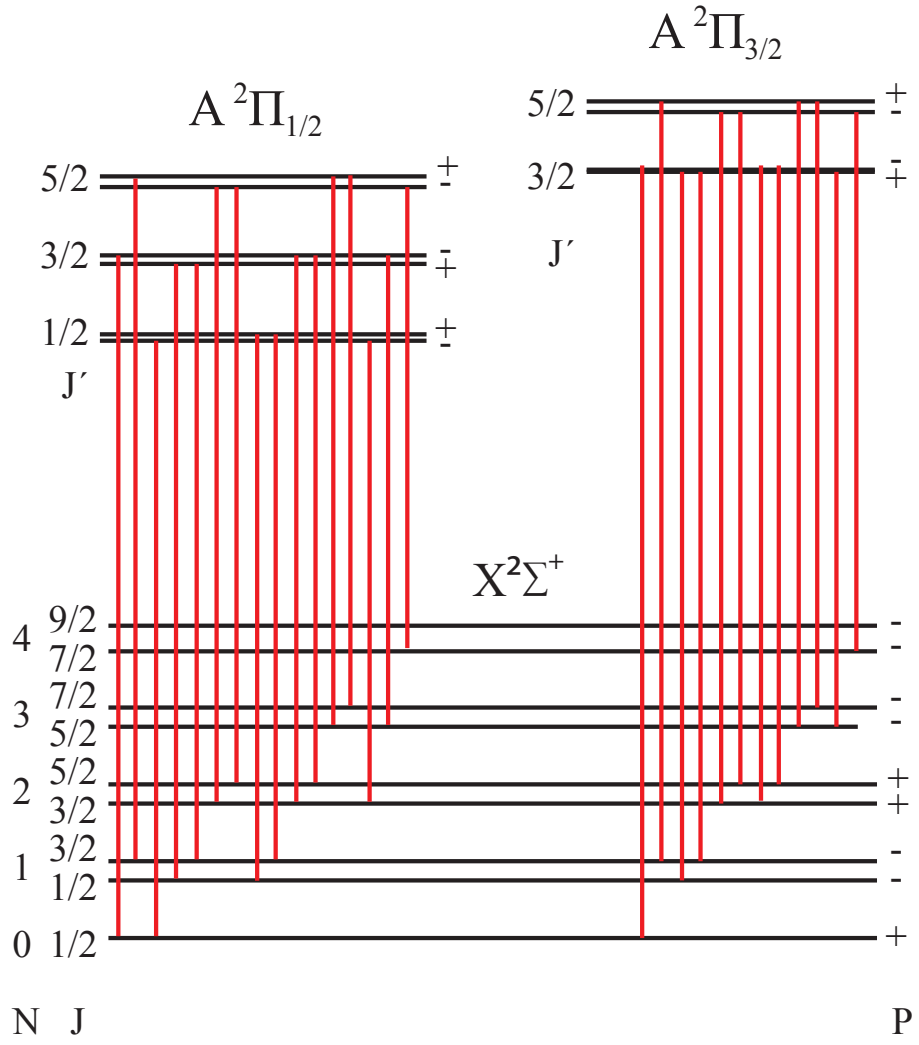

Figure 2.7: *The transitions from the lowest rotational levels of the $A^2\Pi_{3/2}$ and $A^2\Pi_{1/2}$ to the $X^2\Sigma^+$ state of SrF.*

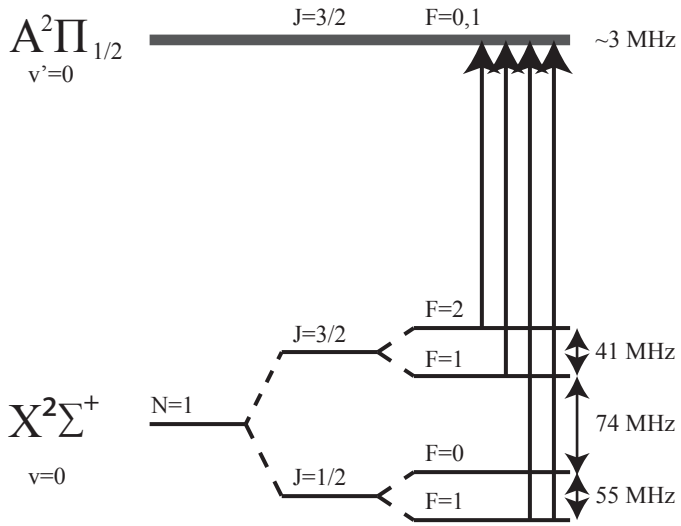

Figure 2.8: *The transitions in the hyperfine structure in the ground and excited state for SrF [45].*

Table 2.1: *The branching ratios of the ground and excited state for SrF [108].*

			$F'=0$	$F'=1$		
J	F	m_F	$m'_F=0$	$m'_F=-1$	$m'_F=0$	$m'_F=1$
		-2	0	.1667	0	0
		-1	0	.0833	.0833	0
$3/2$	2	0	0	.0278	.1111	.0278
		1	0	0	.0833	.0833
		2	0	0	0	.1667
		-1	.0063	.1330	.1330	0
$3/2$	1	0	.0063	.1330	0	.1330
		1	.0063	0	.1330	.1330
$1/2$	0	0	0	.2222	.2222	.2222
		-1	.3271	.1170	.1170	0
$1/2$	1	0	.3271	.1170	0	.1170
		1	.3271	0	.1170	.1170

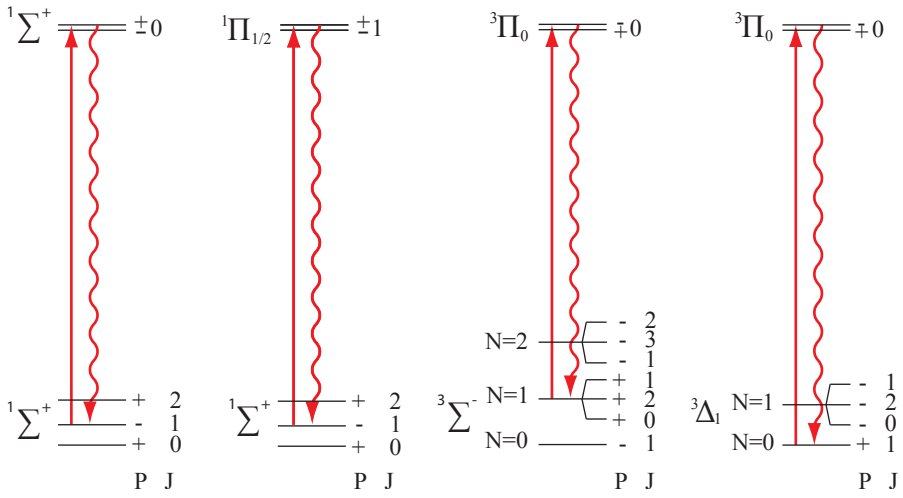

Figure 2.9: *Rotational transitions for other molecules that might be interesting for laser cooling.*

I only look at the electric dipole allowed decays, because for laser cooling the decay time has to be small. Therefore we neglect possible mixing of states, unless candidates for laser cooling have been proposed. Most electronic states with low rotational levels act like Hund's cases a) and b) or a mixture [104]. In Hund's case a) and b) there is the selection rule: $\Delta S = 0$ [104]. As mentioned in 2.2.2., other selection rules are $\Delta J = 0, \pm 1$ and parity has to switch sign.

Looking at other molecules with highly diagonal Franck-Condon factors, I found another four rotational transitions. More is explained in Chapter 3. Figure 2.9 shows four possibilities with the least amount of decays, which is in all cases from the lowest J' to the second lowest J or N. Examples given with Σ^+ have the same transitions with opposite parity for Σ^-. The $^1\Sigma \rightarrow ^1\Sigma$ transition is found in HfO. The $^1\Pi \rightarrow ^1\Sigma$ transition is found in many molecules that are proposed for laser cooling: BH [109, 110], GaF [110], AlF [111], AlCl and AlH [111]. This is a transition with just one dark state because J and J' are the same. The transition $^3\Sigma \rightarrow ^3\Sigma$ is found in NH and $^3\Pi_0 \rightarrow ^3\Delta_1$ is found in TiO.

2.4 External fields

External fields are used to manipulate the molecules: for the traveling-wave Stark decelerator electric fields are used. Magnetic fields are used for remixing of the dark states in a magneto-optical trap, and can be used for a Zeeman decelerator.

2.4.1 Magnetic field

A general way to trap particles that are laser coolable, is to use a magneto-optical trap (MOT). Due to red-detuned laser beams, there is a velocity-dependent force. Due to the magnetic field and the Zeeman shift, the force is also position dependent. In chapter 3 about laser cooling I will give more details about the MOT.

The energy shifts in the ground state are proportional to F and M_F in small magnetic fields (a few Gauss), following:

$$E = g_F \mu_B B m_F, \tag{2.4}$$

where g_F denotes the Landé g-factor. In the ground state of SrF the g_F-factors are 3/2, 5/4, 0, 1, respectively [112]. The Zeeman shift of the ground and excited states is shown in Figure 2.10. The shift of the $^2\Pi_{1/2}$-state is almost zero: Λ and Σ are anti-parallel and $g_L = 1$ and $g_S \approx 2$ [102]. The non-zero value is mostly the contribution of the g-factor from the remixing with the close-lying $B^2\Sigma^+$-state [113].

2.4.2 Electric field

The traveling-wave Stark decelerator makes use of electric fields. Polar molecules have an intrinsic body-fixed electric dipole moment, $\vec{\mu}_e$, that interacts with an external electric field $\vec{E}$. For SrF $\vec{\mu}_e$=3.4676(10) D [114]. The external electric field influences the induced electric dipole moment $\vec{\mu}_{\text{eff}}$ and will cause an energy shift $W(E) = -\mu_{\text{eff}}|E|$. This results in a force $\vec{F} = -\vec{\nabla}W(E)$ on the molecule. The orientation of the molecular dipole with respect to the field determines if the molecule is seeking a high or a low electric field. Low field seeking states can be trapped in the decelerator. In the chapter Experimental approach the decelerator is described in more detail.

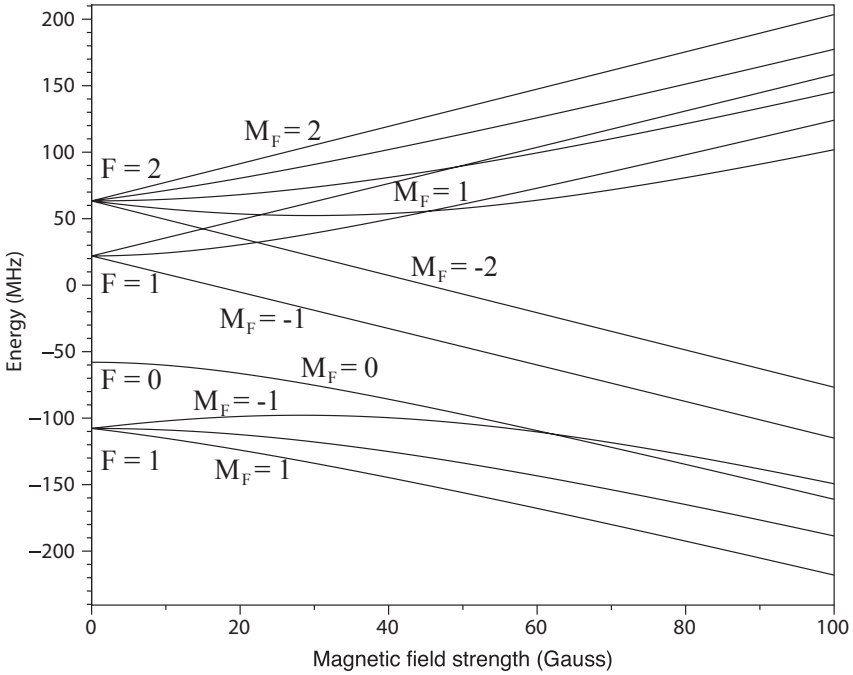

Figure 2.10: *The Zeeman splittings of the lowest rotational lines (ground and excited state) in SrF. The energy is zero at the rotational level $N = 1$ without (hyper)fine splitting. Only the highest and lowest M_F state are mentioned per F. The picture is from the program* PGOPHER *[116].*

For small electric fields second order perturbation theory can be used to calculate the energy shift. For higher electric field strengths the full Hamiltonian has to be diagonalized to solve the Schrödinger equation. This is shown in [44]. In Figure 2.11 the Stark shifts for the first rotational levels in the SrF ground state are shown. This is calculated by PGOPHER [116], a program that simulates molecular spectra.

If electric fields are applied, the quantum states are mixed and the quantum numbers are not a good description anymore. States do not have a defined parity anymore. For laser cooling this means that molecules can leak to higher rotational levels [45, 77, 78].

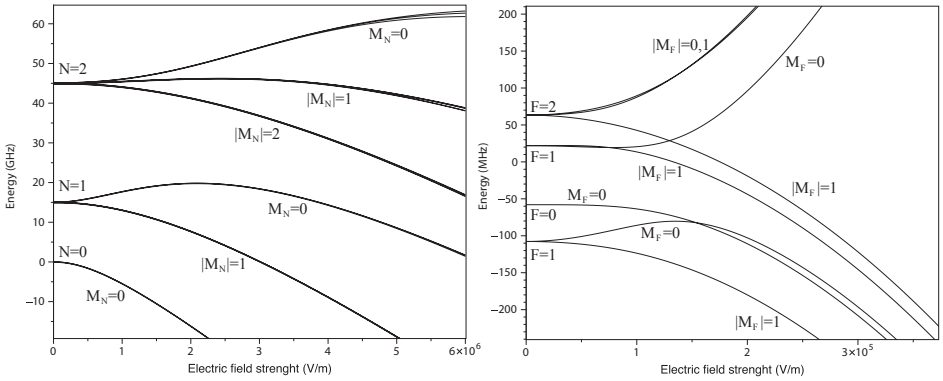

Figure 2.11: *The Stark shift of the lowest rotational lines in SrF (left) and the Stark shift of the hyperfine states of $N = 1$ (right). The calculation of the Zeeman shift is done using the program* PGOPHER *and the molecular constants from literature [115].*

2.5 Summary

This background knowledge is used in the rest of the chapters of this thesis. The highly diagonal Franck-Condon factors and rotational branching ratios make it possible to scatter $\sim 10^3$ photons with a limited amount of laser frequencies. Therefore we can conclude that SrF has suitable properties for laser cooling. The magnetic field is used to destabilize the dark states and the traveling-wave decelerator makes use of the Stark shift of the SrF molecules.

3 | Laser cooling of molecules

In this Chapter we focus on the laser cooling of SrF at the end of our decelerator, where molecules already have a low velocity. Due to the low velocity only a few thousand photon scatterings are required to reach the Doppler temperature. We first discuss laser cooling for an ideal two-level system. Then we go to an extension with multiple levels, described by the multi-level rate equations (MLRE). We use the MLRE to model the interaction of the molecules with light. For laser cooling of SrF it is important to include the effects of repump lasers and magnetic fields in order to avoid ending up in dark states. With this model the number of scattered photons is obtained for various numbers of repump lasers and with/without a magnetic field. This allows us to predict the detection efficiency of the molecules at the end of the decelerator for a range of conditions. The scattering force in 1D, 2D and 3D is obtained for optical molasses for molecules with a velocity of 2 m/s, which is the maximum velocity that molecules have after deceleration to standstill. We model the laser cooling downstream of the decelerator using the Monte-Carlo method: the initial conditions are randomly chosen and the molecules are tracked for the time laser cooling is applied. Besides the simulations, the magneto-optical trap and other possibilities of applying laser light at our traveling-wave Stark decelerator are discussed. We end with comparing SrF to other molecules for laser cooling.

Molecules are, compared to atoms, much more difficult to laser cool due to the decay to several long-lived rotational and vibrational states [77]. However, very recently the first steps have been taken towards molecular laser cooling [45, 46, 80, 81]. Some molecules, such as alkaline-earth monohalides, have properties that are particularly favorable for laser cooling: the Franck-Condon factors are highly diagonal so that a large fraction decays

to only one vibrational level. Molecules are lost from the laser cooling cycle if they are not pumped back into the system again. Rotationally the transition can be closed. Due to parity and selection rules the decay possibilities are limited [78].

In this chapter the focus is on the laser cooling properties of SrF, unless mentioned otherwise. Decay from the $A^2\Pi_{1/2}, J' = 1/2$-state is only allowed to the $X^2\Sigma^+, N = 1$. Due to spin-rotation coupling the $N = 1$ is split up into $J = 1/2$ and $J = 3/2$. These states are split up into the hyperfine levels $F = 1, 0$ for $J = 1/2$ and $F = 1, 2$ for $J = 3/2$. Figure 2.8 shows a schematic overview and more details are given in Chapter 2. The laser cooling cycle has 12 hyperfine substates per vibrational state in the ground state and 4 hyperfine substates per vibrational state in the excited state. In this chapter the interaction between laser light and molecules is simulated. Because of the complex vibrational, rotational and hyperfine structure, a simple two-level model quickly breaks down for simulations of laser cooling of molecules. We model the system using the multiple level rate equations (MLRE). In this model every transition is treated as a two-level system, but the population of the states also depends on all other transitions. The MLRE are valid when the coherence lifetime is much smaller than the population lifetime [117, 118]. Coherence effects are small when the population in the excited state is negligible and saturation does not play a (significant) role [119]. Alternatively, one could use the optical Bloch equations (OBE). This is a good model for the complete system that takes into account all laser fields, but the model is more complicated and less intuitive. The OBE do take into account the coherent dark states, the MLRE do not. The MLRE have been used by other groups for the laser cooling of molecules [37, 108, 113, 120].

3.1 Two-level system

Einstein developed a theory of the interaction between particles and light. A good description can be found in many textbooks [103, 106, 112]. The interaction of a photon with a two level system can be: stimulated absorption, stimulated emission and spontaneous emission. Stimulated emission and absorptions alternate very rapidly, depending on the intensity of the light. This happens at a frequency $\Omega \equiv \frac{-eE_0 d_{ij}}{\hbar}$ [106], where E_0 is the

amplitude of the light field, e the elementary charge and d_{ij} is the electric dipole operator $d_{ij} = \langle j| r |i\rangle$, where r is the electron coordinate. This is called the Rabi frequency [112]. The electric dipole operator gives the strength of the transition between states i and j. The spontaneous emission depends on the lifetime of the excited state and for a two-level system the decay depends on the electric dipole moment and the energy difference ω_{ij} between the two states [106]:

$$\Gamma \equiv \frac{1}{\tau} = \frac{1}{3\pi\epsilon_0\hbar c^3}\omega_{ij}^3 d_{ij}^2. \tag{3.1}$$

In [112] a derivation of the absorption cross section is shown. The cross section for a photon to excite the particle is

$$\sigma(\omega) = 3\frac{\pi^2 c^2}{\omega_0^2}\Gamma g_H(\omega), \tag{3.2}$$

where ω_0 is the laser frequency and g_H the Lorentzian linewidth,

$$g_H(\omega) = \frac{1}{2\pi}\frac{\Gamma}{(\omega-\omega_0)^2 + \Gamma^2/4}. \tag{3.3}$$

The saturation intensity for the transition between state i and j is

$$I_s = \frac{\pi h c \Gamma}{3\lambda^3}. \tag{3.4}$$

The scattering rate is the rate of spontaneous emission from the excited state, which is the same as the cross section times the population difference between states i and j [120]:

$$R_{ij} = \Gamma\frac{s_0/2}{1 + 4\Delta^2/\Gamma^2} \times (n_j - n_i), \tag{3.5}$$

where $s_0 = I/I_s$, I is the laser intensity and the detuning Δ is the difference between the laser frequency and the transition frequency. For a two-level system in equilibrium the scattering rate follows from the previous equation and is given by [103, 106, 112]:

$$R_{\text{scatt}} = \frac{\Gamma}{2} \times \frac{s_0}{1 + s_0 + 4\Delta^2/\Gamma^2}, \tag{3.6}$$

with the maximum scattering rate being $\mathrm{R}_{\max} = \Gamma/2$, at infinite laser power.

The effective force on a particle is then [106, 112]:

$$\mathbf{F} = \hbar \mathbf{k} R_{\mathrm{scatt}}, \tag{3.7}$$

where $\mathbf{k}$ is the wave vector ($\frac{2\pi}{\lambda}$). Particles with velocity $\vec{v}$ observe the incoming photons Doppler shifted by an amount $\omega_D = -\vec{k} \cdot \vec{v}$.

For two red-detuned and counter propagating laser beams, there is a net force anti-parallel to the velocity of the particle along the laser beam axis. This is called optical molasses. For a two-level system the force is:

$$\vec{F}_{\pm} = \pm \frac{\hbar \vec{k} \Gamma}{2} \frac{s_0}{1 + s_0 + [2(\Delta \mp |\omega_D|)/\Gamma]^2}. \tag{3.8}$$

The force is proportional to the velocity for small velocities and low intensities [106]:

$$\vec{F}_{\mathrm{OM}} = \frac{8\hbar k^2 \Delta s_0 \vec{v}}{\Gamma(1 + s_0 + (2\Delta/\Gamma)^2)^2} = -\alpha \vec{v}. \tag{3.9}$$

This is only valid for low laser powers, where saturation does not play a role. The capture velocity is in the range $v_{\mathrm{cap}} \simeq \Gamma/k$.

3.2 Multi-level rate equations (MLRE)

The two-level system cannot describe the interaction of light with the rich level structure of a molecule. The scattering rate depends on the cross section and the population of the states. The population of the states is different for a multi-level system. Furthermore, the excited state can decay to more than one ground state. There is a distinction between Γ, which is the spontaneous decay rate ($\Gamma \equiv 1/\tau$), and Γ_{ij}, which is linearly proportional to the transition strength between two levels. The saturation intensity per transition is:

$$I_s = \frac{\pi h c \Gamma}{3\lambda^3} \frac{\Gamma_{ij}}{\Gamma}. \tag{3.10}$$

The MLRE models the evolution of the states depending on all interactions [108, 120]. The MLRE are:

$$\frac{dn_i}{dt} = \sum_j \Gamma_{ij} n_j - \sum_j R_{ij}(n_i - n_j) - \sum_{k \neq i} M_{ik}(n_i - n_k), \tag{3.11}$$

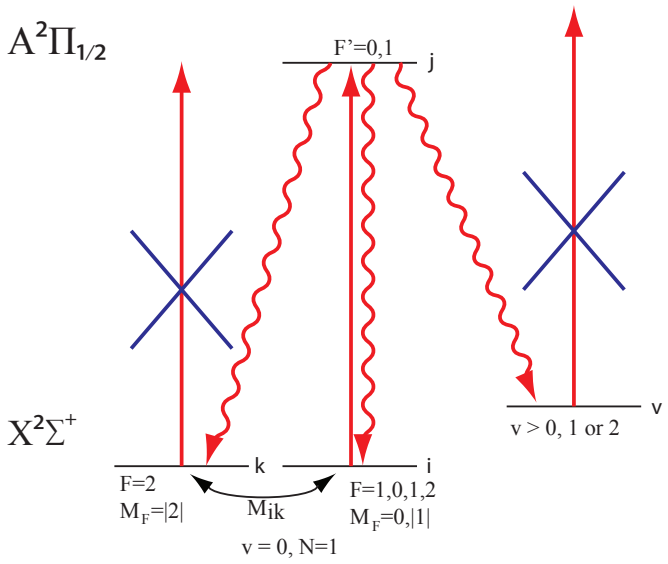

Figure 3.1: *The bright ground states, i, the excited states, j, the dark states, k, and the loss to higher vibrational states v are schematically shown in this figure.*

$$\frac{dn_j}{dt} = -\sum_i \Gamma_{ij} n_j + \sum_i R_{ij}(n_i - n_j) - \sum_{k \notin i} \Gamma_{kj} n_j - \sum_v \Gamma_{vj} n_j, \tag{3.12}$$

$$\frac{dn_{(k \notin i)}}{dt} = \sum_{k \notin i} \Gamma_{kj} n_j + \sum_{k \neq i} M_{ik}(n_i - n_k), \tag{3.13}$$

and

$$\frac{dn_v}{dt} = \sum_v \Gamma_{vj} n_j. \tag{3.14}$$

States i denote the ground states, j the excited states, v the vibrational states that are not resonant with laser light and k the dark states. M_{ik} is the remixing rate between dark and bright states and this is discussed below. A schematic overview of the states is shown in Figure 3.1.

3.3 Dark states

In the laser cooling cycle, the excited state has a lower total angular momentum quantum number, F, than the ground state [78]. In such a configuration there are always two states which cannot be excited regardless

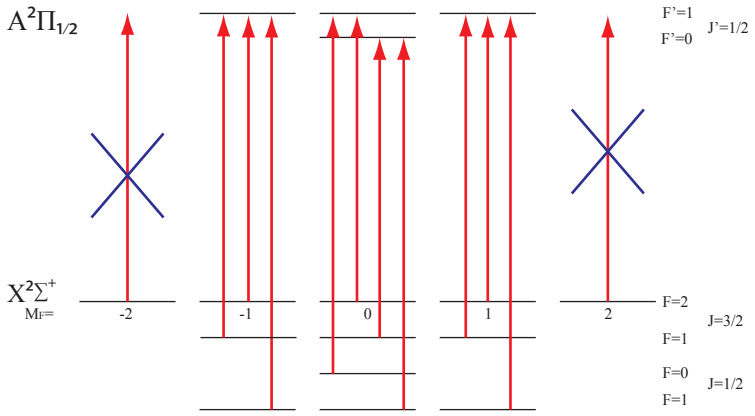

Figure 3.2: *There are dark states when the quantum numbers in the excited state are lower than in the ground state. For all polarizations (↕, ↻, ↺) there are states which can not be excited by laser light. In this picture the transition between the ground and excited state of SrF is shown with linearly polarized light: only* $|m_F| = 2$ *are dark.*

of the polarization [121]. Figure 3.2 shows the dark states of SrF for linear polarization. There are several ways to bring these states back to the cycle. The two most convenient ones are: remixing of the states by a magnetic field [45] or switching the handedness of circularly polarized light [80].

3.3.1 Magnetic field

By applying a magnetic field [45, 79] the different projections of the states can be remixed. The frequency of the remixing is the Larmor-frequency:

$$\omega = \frac{e g_F B}{2 m_e}, \tag{3.15}$$

where e is the charge, B the applied field perpendicular to the linear polarization, g_F the Landé g-factor [112] and m_e the electron mass. There is an optimum, depending on the laser power. Too high magnetic fields cause a large Zeeman shift so that laser frequencies are off-resonant but at too low magnetic fields the dark states are limiting the scattering rate.

3.3.2 Polarization switching

Another way to remix the dark states is to switch rapidly between two types of circularly polarized light. After a few cooling cycles most of the molecules will be in the highest (lowest) m_F dark states. When the polarization is changed, the states become bright and all molecules will be pumped to the lowest (highest) m_F state. This has been used for the 1D and 2D magneto-optical trap for YO [80] and very recently for the improved 3D MOT for SrF [46].

3.4 Simulation results

In the next sections we show simulations with the MLRE of the interaction of light with SrF molecules. With the MLRE the population in every state and the average number of scattered photons can be calculated. The decay time is the average time that a molecule is in the excited state before it decays, including stimulated emission and absorption. The number of scattered photons is the integral of the average excited state population in time, in units of decay time.

The effective scattering rate has been calculated, the number of scattered photons per molecule is discussed, and the detection of molecules at the end of the decelerator is simulated. For the scattering force, the force in optical molasses of the laser cooling is simulated and this is also applied to our experimental setup: laser cooling at the end of the decelerator. The Monte Carlo method is used to track the molecules.

3.4.1 Effective scattering rate

When the system is in equilibrium, an effective scattering rate can be calculated [122]. Scanning over the detuning this has a Lorenzian shape with a height and width, which has different values than the two-level system. The effective scattering rate for SrF with a pump and one vibrational repump laser, is

$$R_{\mathrm{scatt,tot}} \simeq \frac{\Gamma}{7.2} \times \frac{s_{\mathrm{eff}}}{1 + s_{\mathrm{eff}} + 4\Delta^2/\Gamma^2}, \tag{3.16}$$

where s_{eff} is the total saturation parameter, $s_{\mathrm{eff}} \simeq I/(5I_s)$, which is explained in [46]. The maximum effective scattering rate is $\Gamma/7.2$. The maxi-

mum population in the excited state is expected to be $\frac{N_e}{N_e+N_g}$, where N_e and N_g are the number of resp. excited and ground states. For the transitions we are using, $N_e = 4$ and $N_g = 24$, and therefore a maximum effective scattering rate of $\frac{\Gamma}{7}$ is expected. The effective scattering rate obtained from the MLRE is slightly lower due to the remixing of dark states. This formula is obtained for a steady state, when the losses to higher vibrational states ($v \geq 2$) are neglected and a magnetic field remixes the dark states. The four laser frequencies have the same intervals as the four hyperfine transitions. To obtain a Lorenzian shape, every hyperfine state is excited by one laser frequency, which is the frequency on resonance when $\Delta = 0$. With only the pump laser the simulations give an effective scattering rate of $R_{\text{scatt,tot}} \simeq \frac{\Gamma}{4.1} \times \frac{s_{\text{eff}}}{1+s_{\text{eff}}+4\Delta^2/\Gamma^2}$. Here $N_g = 12$, which explains the factor $\frac{\Gamma}{4}$. With the pump and two vibrational repump lasers, the second repump laser makes a transition between the $v = 2$ and the $v' = 1$ vibrational states. This transition is not connected to the transitions of the other two lasers so the number of states in these two vibrational states are not added to N_e and N_g. The scattering rate is $R_{\text{scatt,tot}} \simeq \frac{\Gamma}{7.3} \times \frac{s}{1+s_{\text{eff}}+4\Delta^2/\Gamma^2}$. s_{eff} is the same in these three cases.

3.4.2 Number of scattered photons

The effective scattering rate is simulated for a system in equilibrium: a magnetic field is applied to mix dark and bright states and the vibrational leak is neglected. In the rest of the simulations the vibrational leaks are included and not in all cases a magnetic field is applied. The population of all the hyperfine substates evolves. An example is shown in Figure 3.3. In this example there is no magnetic field and only one pump laser with an intensity of 150 W/m^2 per sideband.

The number of scattered photons depends on the interaction time, the laser power, the number of repump lasers and the applied magnetic field. Figure 3.4 shows the total number of scattered photons as function of time for several number of repump lasers when an intensity of 30 W/m^2 per sideband is used and a magnetic field of 1 Gauss. When linearly polarized light is used, one pump laser and no remixing of the dark states by a magnetic field is applied, 86% of the molecules end up in the $|m_F| = 2$ hyperfine substate, the other 14% goes to the $v = 1$. On average the number of scattered pho-

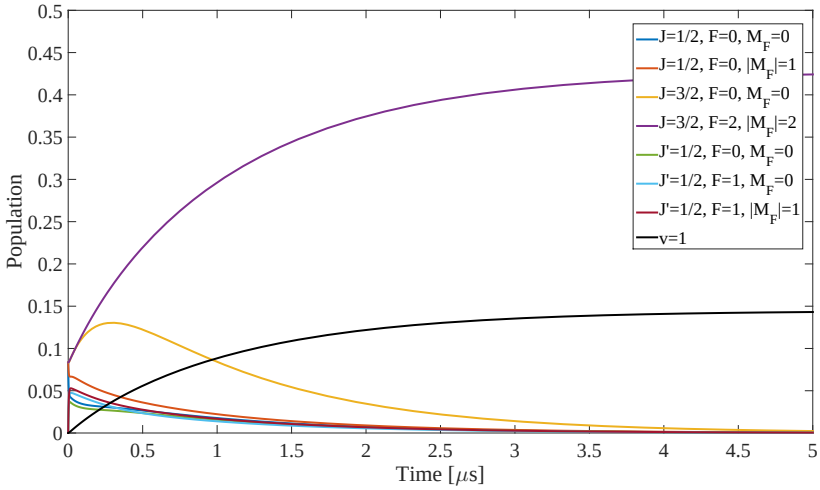

Figure 3.3: *The evolving population of hyperfine substates as function of time. There is no magnetic field and one pump laser with intensities of 150 W/m^2 per sideband.*

tons is 7.8 and after 5.8 μs, 90% of the molecules ends up in a dark state. When a magnetic field of 1 Gauss is applied, most of the molecules will end up in the $v = 1$ vibrational state after 54 scatterings, which is expected from the Franck-Condon factors. 90% of the molecules has reached higher vibrational states in 21 μs. Using one repump laser, most molecules end up in the $v = 2$ after $1.4{\times}10^4$ scatterings. 90% of the molecules will be in the $v = 2$ and higher states in 11 ms. The second repump laser pumps molecules from the $v = 2$ vibrational state into the $v' = 1$ state. With two repump lasers it takes $2.3{\times}10^4$ photon scatterings for the molecules to get lost mainly to the $v = 3$. After 17 ms, 90% of the molecules are lost from this laser cooling cycle.

In the previous simulation the laser intensity was kept constant. When the laser intensity is changed, the evolution of the population changes: for higher intensities the system is faster in equilibrium than for lower intensities. The maximum number of scatterings on average before the molecule ends in a dark states is independent on the laser intensity. Figure 3.5 shows the total number of scatterings after 1 ms as function of the laser intensity.

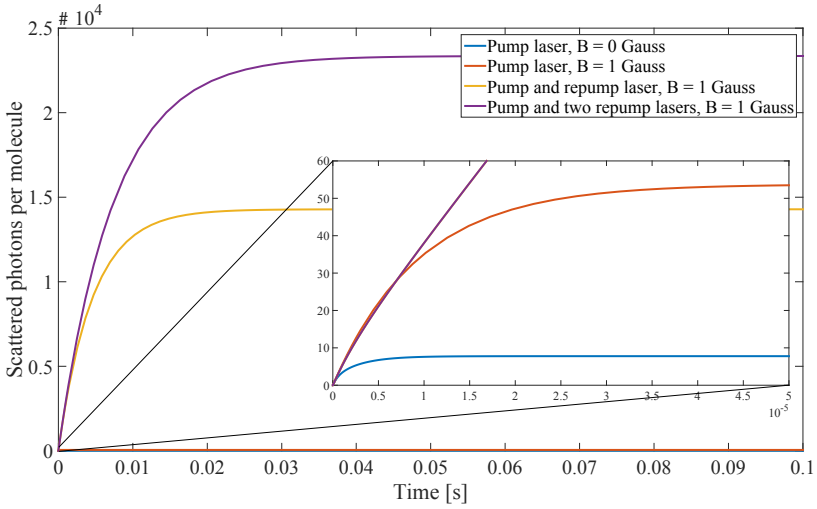

Figure 3.4: *The total scattering of light for several situations is shown. This is with a total intensity of 30 W/m^2 for every sideband.*

For the intensities up to 1 W/m^2, the loss to $v = 2$ and $v = 3$ is so small that there is no difference between the system with one and with two repump lasers.

These simulations were all done with a constant laser intensity, to obtain the number of scattered photons as function of magnetic field and number of repump lasers.

3.4.3 Simulations of the detection

For the detection of molecules at the end of the decelerator we used Laser Induced Fluorescence (LIF), the details of which are described in Chapter 4, section 4.4. We have a detection laser beam with a $1/e^2$ diameter of 2.4 mm. We calculated the number of scattered photons per molecule for the molecules at the detection zone downstream of the decelerator, using the parameters of the laser beam used in the experiments. We assumed that only low-field seeking molecules reach the end of the decelerator. Unless mentioned otherwise we used a sinusoidal input for the EOM at 41.8 MHz to create 4 frequency sidebands with the same power distribution in the first

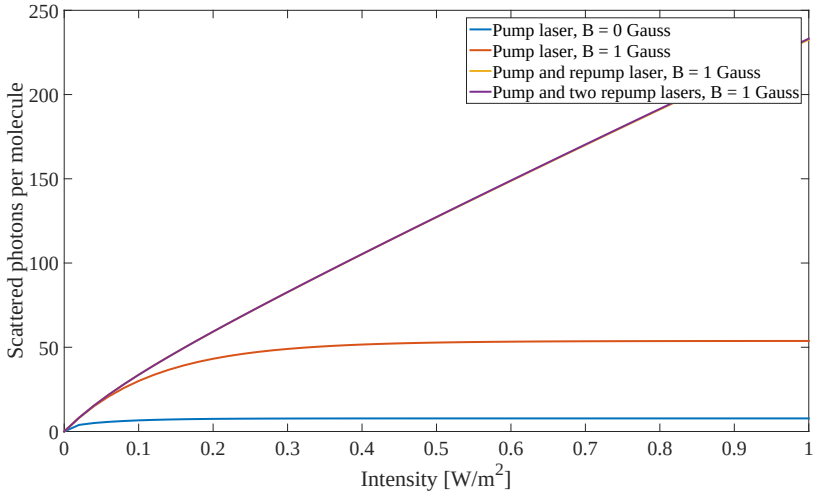

Figure 3.5: *The total scattering of photons after 1 ms as function of the laser intensity. The yellow and purple lines are nearly overlapping.*

and second order. The detuning of the lowest frequency is +4 MHz from resonance, such that the overlap between the sidebands and the hyperfine splittings is the best. Some examples with velocities of 560 m/s are given in the next paragraphs. This is the molecular velocity when Ar is used as carrier gas and molecules are guided through the decelerator.

Number of scattered photons per molecule

In the previous paragraph we have used a fixed laser intensity. For the detection of the molecules at the end of the decelerator, the laser beam has a Gaussian power distribution. In the experiments we mostly used 0.5 mW of detection power. The number of scattered photons per molecule as they pass the detection zone at a velocity of 560 m/s is simulated in Figure 3.6. In the simulations there is no difference in the number of scattered photons per molecule without repump lasers and with one or two repump lasers. Due to the small size of the laser beam and the large velocity of the molecules, the number of scattered photons is limited by the small interaction time. Therefore, an extra repump laser does not increase the number of scattered photons, while a magnetic field does.

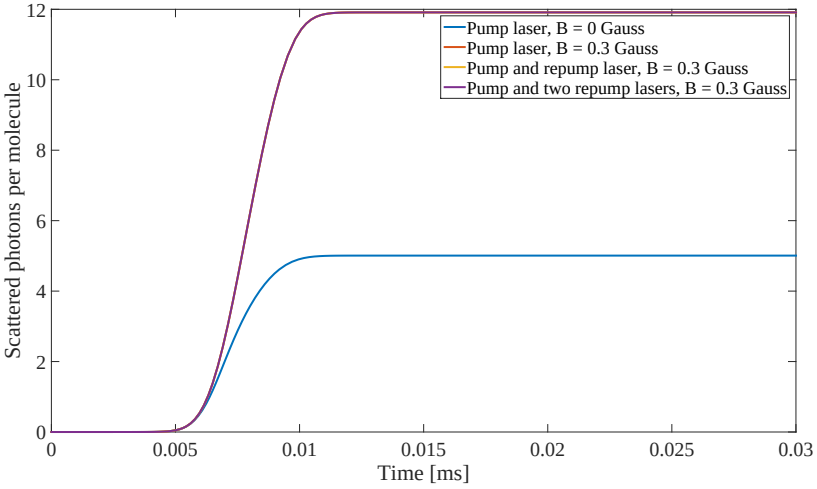

Figure 3.6: *The total scattering of photons with a Gaussian power distribution with an $1/e^2$ diameter of 2.4 mm and a velocity of the molecules of 560 m/s. The red, yellow and purple line are overlapping, due to the short interaction time. Also the maximum number of scattered photons per molecule has not been reached due to the short interaction time.*

Signal to noise optimization

In this section we determine the laser power that leads to the optimal signal-to-noise. The number of scattered photons from a molecule depends on the laser power. The background signal from stray light is assumed to be linearly proportional to the laser power. Additionally, there is a background, i.e. the dark counts from the PMT, that is independent of the laser power, which corresponds to ~ 6 μW of laser power. The statistical uncertainty on the number of detected photons is proportional to $\frac{1}{\sqrt{N}}$, where N is the number of detected photons. From Poissonian statistics the accuracy of the number of detected molecules is the number of scattered photons per molecule divided by the square root of the background. Figure 3.7 gives an example of the accuracy as function of the detection power to obtain the optimal detection power. For molecules with a velocity of 560 m/s the optimal detection power is 0.4 mW without additional magnetic field. With a magnetic field of 1.1 Gauss the optimal detection power is 0.8 mW. For 20 m/s the optimal magnetic field is 0.5 Gauss. The two different magnetic

fields are shown to see the relatively small dependencies on the magnetic fields in this velocity range.

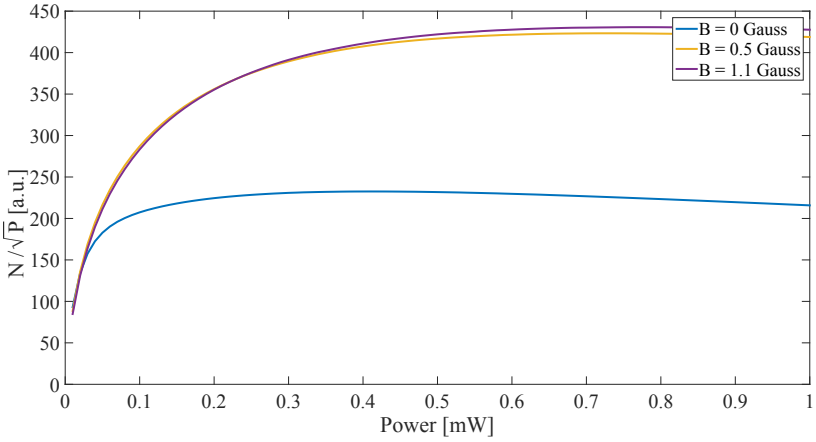

Figure 3.7: *The accuracy of the detection of molecules as function of detection power. In this example molecules have a velocity of 560 m/s and the optimal detection power is 0.4 mW without magnetic field and 0.8 mW with the optimal magnetic field of 1.1 Gauss. The error bar is expected to be 10%, mainly because in reality the laser is locked within 2 MHz.*

Figure 3.8 shows the optimal detection power as function of the velocity of the molecules, with and without magnetic fields. For low velocities the interaction time is relatively long so a low detection power is optimal. For lower powers the optimal magnetic field is also lower than for higher powers. For higher velocities the optimal detection power is higher in order to scatter more photons per molecule.

Single molecule detection

In this section we go through the requirements that would enable us to detect sufficient fluorescence from a single molecule so that we can count them while they travel through our detection system. An optimized system for the collection of fluorescence has typically an efficiency of 1%, which includes the transmission of the optical system and the quantum efficiency of the photon detector. If we would be able to detect on the order of 100

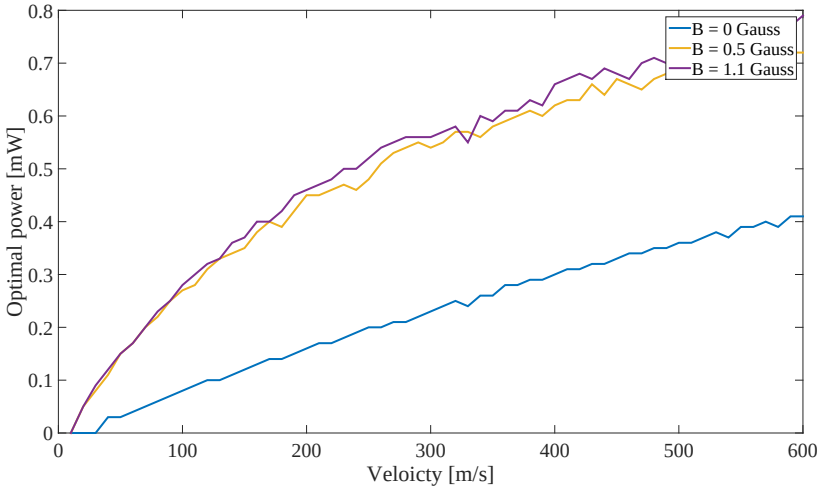

Figure 3.8: *The optimal power for the highest accuracy as function of the velocity of the molecules at the end of the decelerator.*

photons per molecule, we should be able to clearly separate the fluorescence of two molecules from that of one, since $\frac{\sqrt{N}}{N} = \frac{1}{\sqrt{N}}$is 0.1 in this case. We therefore require about 10k photons to be scattered per molecule. These photons should ideally be scattered from a small volume, if we want to be able to collect them with 1% efficiency. With a lifetime of 23 ns, and a maximal effective scattering rate of $\Gamma/7$, we have a maximum scattering rate of $6{\times}10^6$ photons/s. The 10k photons can therefore be scattered in 1.6 ms. If we require the fluorescence to be emitted from a volume of 1 mm^3 then this corresponds to a velocity of 0.6 m/s. Reducing the number of photons to be detected by an order of magnitude also increases this velocity by an order of magnitude to 6 m/s. This all is assuming that the number of background photons is negligible. In conclusion, we would be able to detect molecules with a single molecule resolution if they are cooled close to the Doppler temperature ($\sim$0.2 m/s) but not from a fast moving beam. For molecules with velocities on the order of 60 m/s a more elaborate excitation and fluorescence collection system would have to be designed in order to collect photons along a 10 cm long path.

Symmetric versus asymmetric sidebands

We compare the detection of the four sidebands using a sinusoidal input for the EOM, which is called the symmetric sidebands, to four sidebands made by a sawtooth as input for the EOM, the asymmetric sidebands. In Chapter 4 more is described about the sinusoidal and sawtooth input for the EOM. Assumed is that the asymmetric frequencies made with the sawtooth input are perfectly overlapping with the four hyperfine frequencies of SrF. With the sinusoidal sidebands the frequency spacing is symmetric and the frequencies do not address the four hyperfine frequencies exactly. Experimentally the asymmetric sidebands have imperfections and some laser power is lost to other frequencies. Nevertheless, the model assumes the perfectly addressed frequencies. Figure 3.9 shows the number of scattered photons per molecule as function of laser power for both cases. The molecules have a velocity of 560 m/s. According to the simulations the scattering rate is 19% better using the asymmetric instead of the symmetric sidebands at 0.5 mW of laser power and no magnetic field. For higher powers the improvement is less because of power broadening. The asymmetric sidebands have the maximum number of scattered photons per molecule for that laser power.

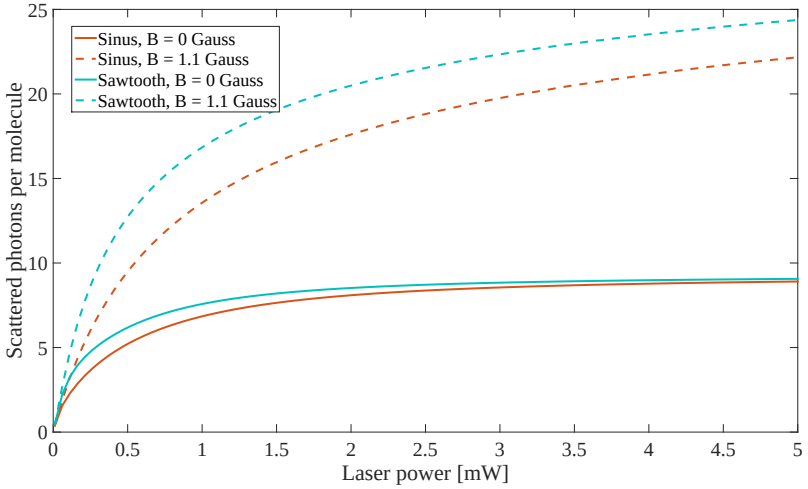

Figure 3.9: *The number of scattered photons per molecule with and without magnetic field for the sinusoidal and sawtooth input to the EOM as function of laser power. The molecules have a velocity of 560 m/s.*

3.4.4 The scattering force in 3D optical molasses

In this section we investigate the scattering force. In the next sections we use the scattering force to investigate 2D and 3D optical molasses at the end of the decelerator. When the end trap is switched off, molecules have a maximum velocity of 2 m/s in all directions. Therefore we focus on molecules with small velocities.

The scattering force for a two-level system is proportional to $\vec{v}$ and is described in Equation 3.9. Using the effective scattering rate of Equation 3.16, α can be described by [37]:

$$\alpha = \frac{8 s_{\text{eff}} \hbar k^2 \delta_0 \Gamma_{\text{eff}}}{m(1 + s_{\text{eff}} + 4\delta_0^2/\Gamma^2)^2 \Gamma^2}, \tag{3.17}$$

where $\Gamma_{\text{eff}} = \frac{2}{7.3}\Gamma$ when two repump lasers are used.

In the MLRE all 24 states are used, not the effective scattering rate. The acceleration is [113]:

$$\frac{dv}{dt} = \frac{\hbar k}{m} \sum_{i,j} R_{ij}(N_j - N_i)\hat{k}. \tag{3.18}$$

In Figures 3.10 – 3.12 the acceleration of the molecules is shown as a function of velocity, detuning and laser intensity. This is the acceleration in 3 dimensions with two repump lasers. The intensity is kept constant, in contrast to the next section where the intensity depends on the position of the molecule. The Figure shows the acceleration for both the asymmetric and symmetric inputs for the EOM. The power is 30 W/m^2 per sideband ($s_{\text{eff}} = 0.2$) and besides the four sidebands per laser, power losses to other frequencies due to imperfections are neglected.

The Figures show the dependence on the detuning of the pump laser. The detunings of the two repump lasers are -0.2 MHz and -0.1 MHz for resp. state $v = 1$ and the $v = 2$. The laser frequencies are almost resonant with the transitions because the saturation parameter is $\sim 50\times$ lower: the two repump lasers are mainly used to repump the molecules into the system, not to apply a scattering force on the molecules. The magnetic field perpendicular to the polarization is 0.6 Gauss.

The frequency spacings of the sidebands in the symmetric case for the pump and two repump lasers are resp. 42.7 MHz, 42.3 MHz and 40.9 MHz with a detuning of the repump lasers of 1.2 MHz and 1.7 MHz with respect to the $J = 1/2, F = 1$ state. The hyperfine splittings in the $v = 1$ and $v = 2$ are slightly different than in the $v = 0$ [108]. The optimal magnetic field with 30 W/m^2 is $B = 0.7$ Gauss. Unless mentioned otherwise, the acceleration is given for a velocity of 2 m/s.

Figure 3.10 shows the dependence of the acceleration on the detuning of the pump laser for several velocities. Figure 3.11 shows the acceleration for several detunings of the pump laser as function of velocity. For the asymmetric input the optimal detuning at 2 m/s is -3.0 MHz, for the symmetric input this is also -3.0 MHz with respect to the transition from the $J = 1, F = 1$ to the excited state. For lower velocities the optimal detuning is slightly less. Figure 3.12 shows the dependence on the laser intensity. For higher powers coherences play a role in the scattering rate, which are neglected in the model.

In this section the scattering force in 3 dimensions is simulated with a constant intensity, when $s_{\text{eff}} = 0.2$. The maximum acceleration is 3.4 km/s^2 and 2.1 km/s^2 for $v = 2$ m/s for laser frequencies made by a sawtooth resp. sinusoidal input for the EOM.

Also simulations with zero, one or two repump lasers and for 1D, 2D and 3D are done to compare the different situations. The decay to higher order vibrational states is neglected, so that the system reaches a steady state. Table 3.1 shows the accelerations (in km/s^2) for $v = 2$ m/s, $I = 30$ W/m^2 and sidebands obtained from an asymmetric input to the EOM. The other parameters (magnetic field and detunings) are optimized and similar to 3D laser cooling with two repump lasers.

The difference between 1D, 2D and 3D cooling comes from the saturation of the excited state. For high powers, when the system is saturated, the force is inversely proportional to the number of laser beams. For low powers the scattering force is almost equal for the three cases. The acceleration with one and two repump lasers does not differ, which is also expected from the

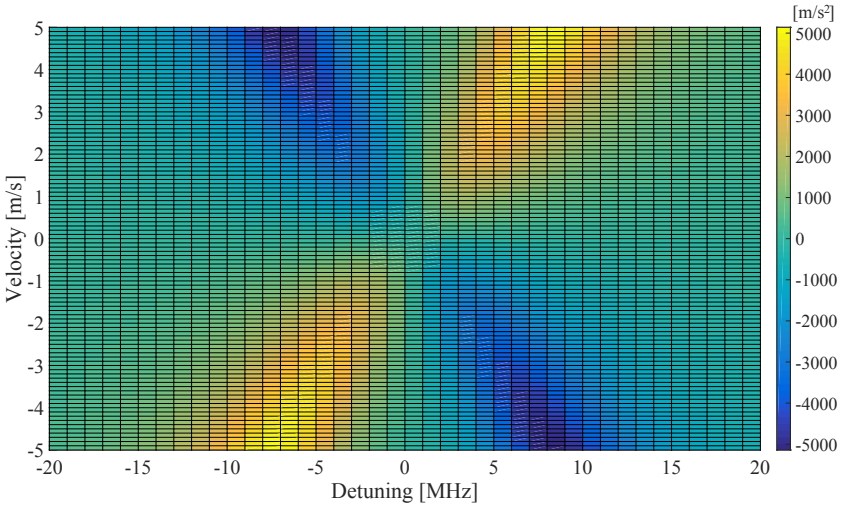

(a)

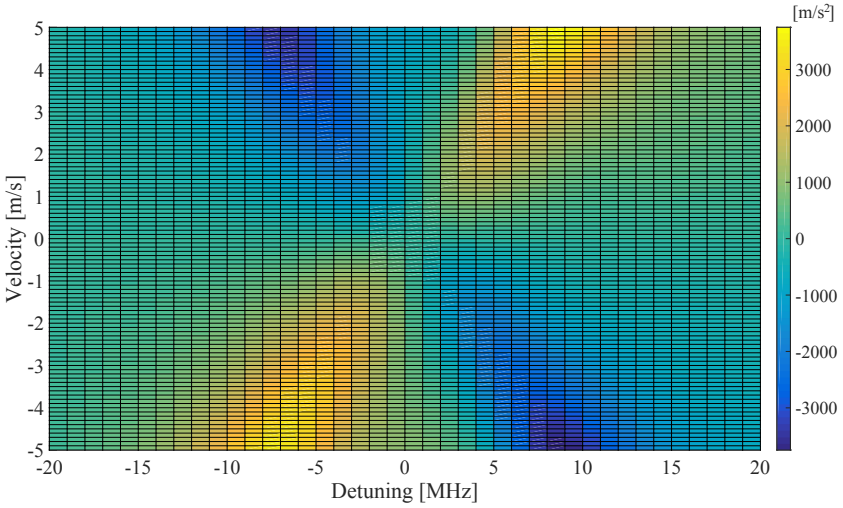

(b)

Figure 3.10: *The acceleration due to the laser cooling force in three dimensions. Two repump lasers are used. The upper graph shows the acceleration for the laser frequencies with the asymmetric sidebands, while the lower graph shows simulations with symmetric sidebands. The acceleration is a function of the pump laser detuning, while the detunings of the repump lasers are fixed. The parameters are described in section 3.5.2.*

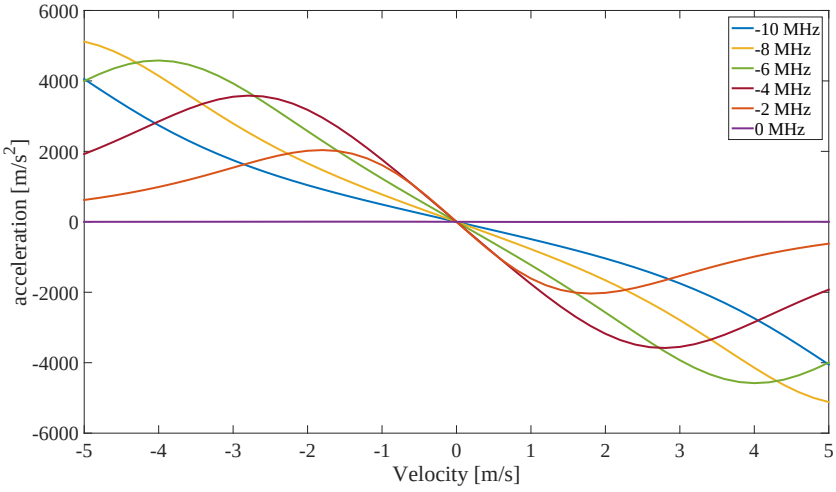

(a)

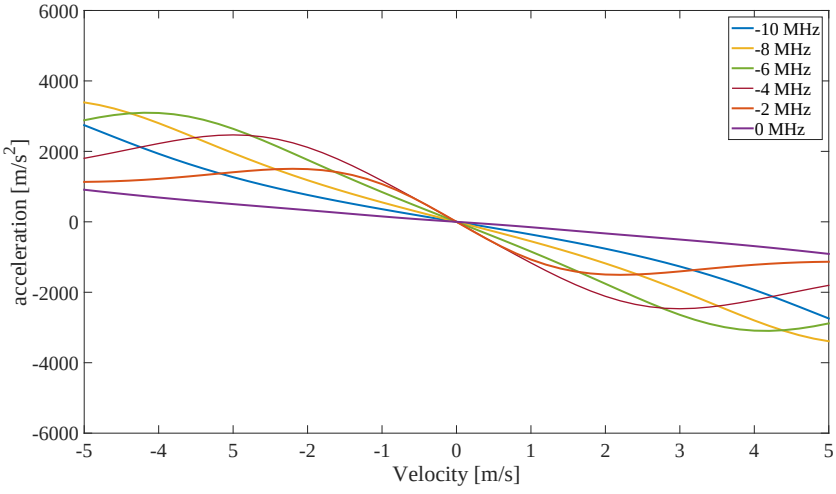

(b)

Figure 3.11: *The acceleration as function of velocity for several detunings. The upper graph shows the acceleration for the asymmetric sidebands, while the lower graph for symmetric sidebands. For velocities close to zero the highest acceleration is at -3 MHz detuning for both situations.*

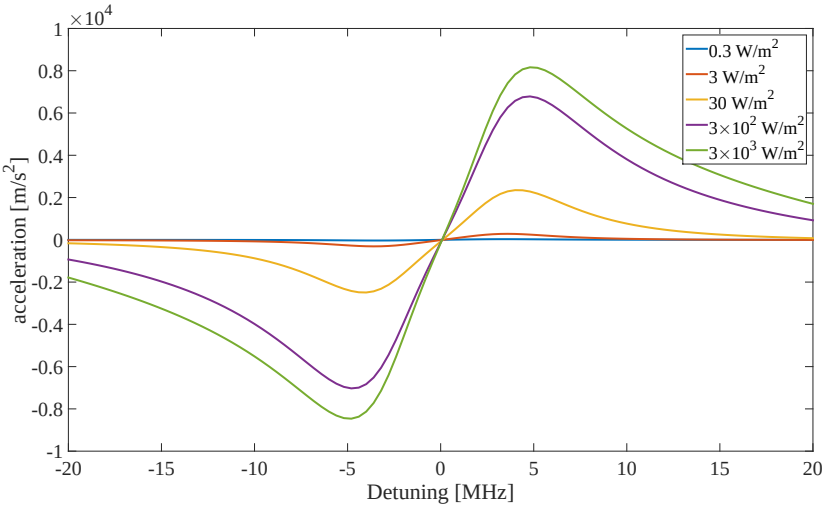

(a)

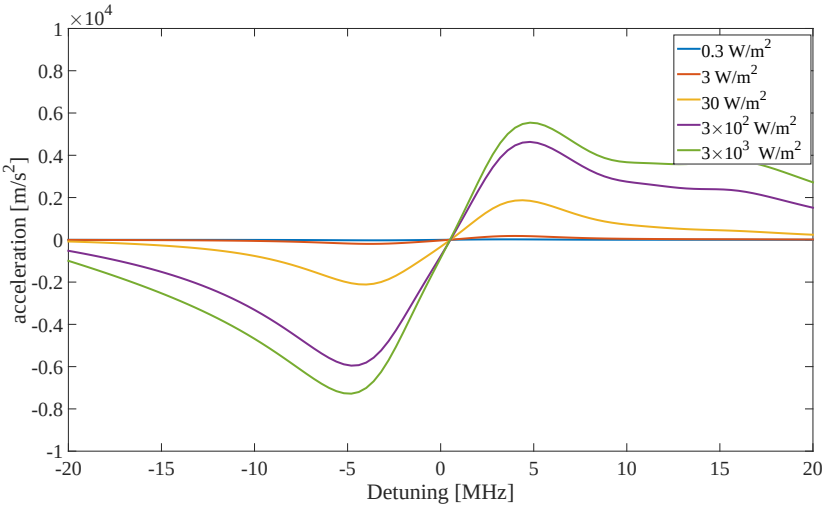

(b)

Figure 3.12: *The acceleration for laser intensities varying over several orders of magnitude as function of detuning for the asymmetric sidebands (top) and symmetric sidebands (bottom). For high intensities ($\gg$30 W/m^2) coherences start playing a role, which are not included in the MLRE model.*

Table 3.1: *The maximum acceleration in km/s^2 resulting from the scattering force at $v = 2$ m/s for laser beams in 1, 2 and 3 dimensions, without vibrational repump laser and with 1 or 2 repump lasers.*

# repump lasers	1D	2D	3D
0	-7.6	-6.4	-5.5
1	-3.8	-3.7	-3.3
2	-3.8	-3.8	-3.4

effective scattering rate in Equation 3.16. The acceleration with only the pump laser is stronger, but the leak to the $v = 1$ and higher vibrational states is also high.

The maximum acceleration for 1D with two repump lasers occurs at $\Delta_0 = 2\pi\times$ 3.8 MHz. Using Equation 3.17, $\alpha/m = 2.2 \times 10^3$ s^{-1}. From the simulations $\alpha/m = 1.9\times10^3$s^{-1}. The effective scattering rate ignores transitions other than the laser frequency that is on resonance when the detuning is zero. This explains the difference.

For $\alpha/m = 2 \times 10^3$s^{-1}, the acceleration is $a = F/m = \alpha v/m$. For an average velocity $v = 1$ m/s, $a = 2 \times 10^3$ m/s^2 and it will take 0.5 ms to decelerate to $v = 0$ m/s, when the random scattering is neglected.

3.4.5 Laser cooling of CaF and BaF

The molecular structure of CaF and BaF is similar to SrF. These molecules are also suitable for laser cooling on the transition from the $X^2\Sigma^+$ to the $A^2\Pi_{1/2}$ state. Table 3.2 shows the used input parameters and the simulated α for $s_{\text{eff}} = 1$ per sideband. The scattering force is expected to be proportional to the momentum kick $\hbar k$ ($k = \frac{2\pi}{\lambda}$) and the decay rate ($\Gamma = 1/\tau$). This is given in the table and $\alpha \times \tau \times \lambda$ is almost similar in the three cases. Small differences are from the hyperfine structure and the Franck-Condon factors.

Table 3.2: *The input parameters used to obtain α/m for laser cooling of CaF and BaF. The laser cooling force is proportional to v for small velocities: $F = \alpha v$.*

	CaF	SrF	BaF
τ [ns]	19 [120]	24 [123]	56 [124]
λ [nm]	606 [81]	663 [45]	860 [125]
m [amu]	59	107	157
hfs [MHz]	76, 47, 25 [81]	55,74,41 [45]	27, 90, 34
f_{00}	0.979 [81]	0.983 [108]	0.953 [126]
f_{01}	0.0219	1.6×10^{-2}	0.044
f_{02}	2.7×10^{-5}	3.5×10^{-4}	0.003
f_{10}	0.023	2.0×10^{-2}	0.045
f_{11}	0.937	0.95	0.869
f_{12}	0.041	3.2×10^{-2}	0.086
α/m [s^{-1}]	14×10^{3}	6.4×10^{3}	1.3×10^{3}
$(\alpha\times\tau\times\lambda)/h$	2.3×10^{-2}	2.6×10^{-2}	2.4×10^{-2}

3.4.6 2D laser cooling

In the previous sections, the scattering force for a fixed intensity was simulated for several parameters. In this section and especially the next section about 3D laser cooling, the molecular dynamics are also included.

2D laser cooling can be used to do cold beam experiments [13, 37] for eEDM and PV experiments. Molecules fly through an interaction zone and are detected afterwards. This can also be done in a fountain arrangement. The product of the interaction time and the number of the molecules ($\tau\sqrt{N}$) should be optimized to increase the experimental sensitivity. A longer interaction time during which the sample expands does not increase the sensitivity. However, making the beam colder increases the sensitivity. Figure 3.13 shows a schematic overview of the 2D laser cooling and interaction zone afterward. A reasonable size for the interaction zone is ~ 50 cm. At the end of the decelerator, the molecular packet has a certain velocity v_x and a cross sectional area $A1$. After laser cooling the area is slightly larger, called $A2$. After expansion while flying through the interaction zone the molecules occupy an area $A3$. The molecules will be detected within area $A3$ and realistically the diameter of $A3$ should be ≤ 5 cm.

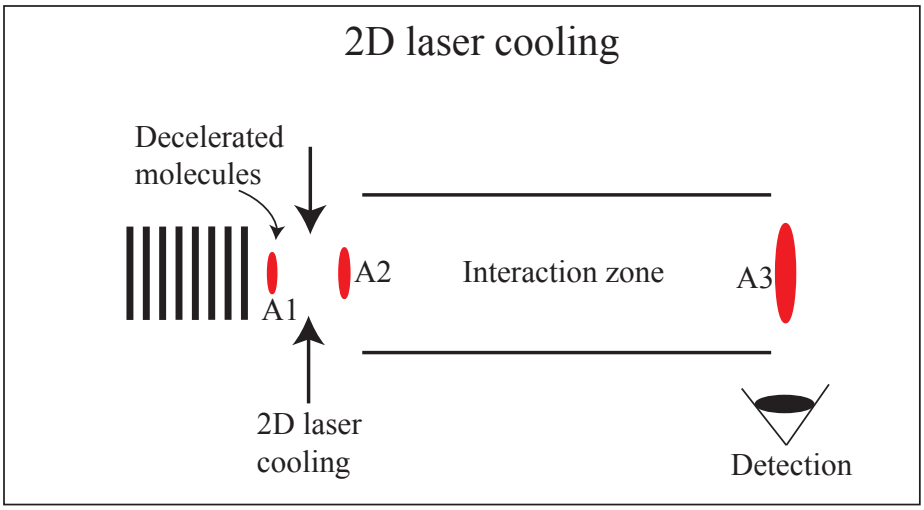

Figure 3.13: *A schematic overview of the 2D laser cooling experiment that could be done behind the decelerator. A1, A2 and A3 are the molecular beam sizes at several positions in the experiment.*

We can choose the longitudinal velocity at the end of the decelerator. The interaction time for SrF to reach the Doppler limit is ~ 0.5 ms when the laser is power 150 mW per sideband and a $1/e^2$ beam diameter of 4 cm is used. The maximum intensity is at $s_{\text{eff}} = 1$. Figure 3.14 shows the velocity of a molecule as function of time when one of the transverse directions starts at 2 m/s. If we restrict ourselves to the geometry of the designed end trap, the maximum laser beam diameter is 5 mm so v_x should be maximally 10 m/s for optimal laser cooling. When the Doppler temperature can be reached, the RMS speed is $v_{LC} = 0.2$ m/s. With a transverse velocity of 0.2 m/s, the molecule is 2.5 cm away from the center in 0.125 s so the molecule should have a minimal longitudinal velocity of 4 m/s in order to reach $A3$. The longitudinal velocity has to be higher in order to capture also the molecules that have a higher transverse velocity than 0.2 m/s. The longitudinal velocity at the end of the decelerator should be between 4 m/s and 10 m/s for optimal beam experiments. For velocities lower than ~ 4 m/s the spread of the molecules becomes too large, for velocities higher than 10 m/s the interaction time of laser cooling is too short to cool the molecules to the Doppler limit. This limited velocity range could be easily

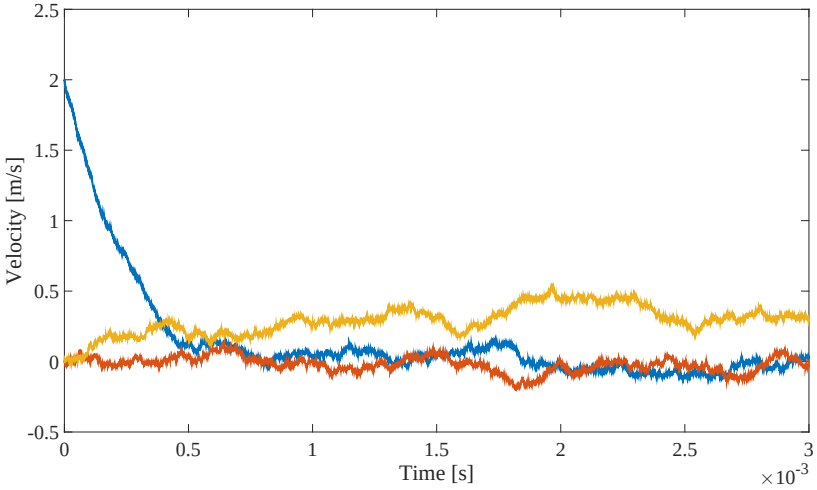

Figure 3.14: *The velocity in time for 2D cooling with a laser power of 150 mW per sideband and a $1/e^2$ beam diameter of 4 cm. One of the transverse velocities (blue) starts at 2 m/s and slows down to the final velocity in around 0.5 ms. The other two directions have an initial velocity of 0 m/s and spread out due to photon scatterings in random directions.*

significantly extended for a dedicated slow molecular beam experiment by increasing the length of the laser cooling zone.

3.4.7 3D laser cooling

In section 3.5.2 the acceleration of molecules for a given laser power is shown, to see the dependence on all the other parameters. For the simulations of the acceleration of the molecules at the end trap, the molecular dynamics must be included. The molecule is moving in space, the velocity decreases and the laser intensity is a function of the position of the molecule. The Monte Carlo method is used for the initial spatial and velocity distribution of molecules and the molecules are tracked in space and time during the laser cooling. The initial spatial distribution is based on the dimensions of the end trap. The molecules have an initial velocity between 0 m/s and 2 m/s in all three directions. The initial position is a circle with a distance of max. 0.875 mm in the direction of the decelerator and 1.87 mm in the other directions. The average velocity distribution corresponds to a temperature

of 12 mK. The internal state of the molecules is calculated with the MLRE and is the average for that position and velocity.

Laser frequencies that exactly match the hyperfine structure (as can be made with the asymmetric input of the EOM) are used. The $1/e^2$ diameter of the Gaussian distribution of the laser beam is 4 cm, the optimal detuning of the pump and repump lasers are resp. -2.8 MHz, -0.3 MHz, 0 MHz. The optimal magnetic field at an angle of 45 degrees is 0.6 Gauss. The parameters are slightly different than for 2 m/s: on average the velocity in one direction is lower than 2 m/s. The dependence on the parameters are shown in the Figures 3.15–3.18 and the optimal parameters were used for the other figures. To save a lot of computer time, first the random scattering is neglected to obtain the parameters for the optimal scattering force. I stopped the simulations after the time where around 50% of the molecules would have had a velocity below the recoil kick at these optimal settings.

The optimal detuning for the pump lasers is set at 2.8 MHz, which is close to $\delta = \Gamma/2 = 2\pi \times 7/2$ MHz [112]. The dependence on the detuning is mainly due to the velocity spread of the molecules. The optimal detuning for the repump lasers is close to 0. The saturation intensity of these transitions is 50× smaller. This transition mainly is used for pumping the molecules back into the system and not for cooling.

3.4.8 Velocity spread

To obtain the velocity spread, the random scattering of the spontaneous emission is taken into account. There is a velocity kick of $\hbar k/m$, where m is the mass of the molecule. This happens randomly with an average rate equal to the excited state population multiplied by Γ. The simulation takes a longer calculation time, so this is done to get the velocity distribution at the end of the laser cooling. With the optimal parameters from section 3.6.2 the RMS velocity in time for several laser powers is simulated. This is shown in Figure 3.19. In this model 10 mW corresponds to a maximum intensity of 30 W/m^2 per sideband and $s_{\text{eff}} = 0.2$. The coherences are neglected in this model.

Figure 3.19 shows the decrease in velocity spread, which reaches an equilibrium. It shows that for high powers the corresponding final temperature

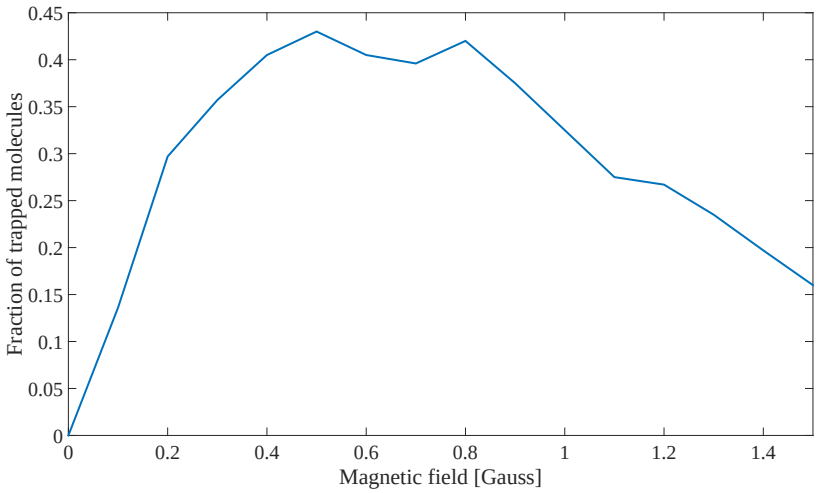

Figure 3.15: *The fraction of molecules that reach the recoil velocity as function of the magnetic field strength. The random momentum kicks from scattering are neglected. The magnetic field is aligned at an angle of 45 degrees with respect to the laser beams. A magnetic field of 0.6 Gauss is used for the other simulations.*

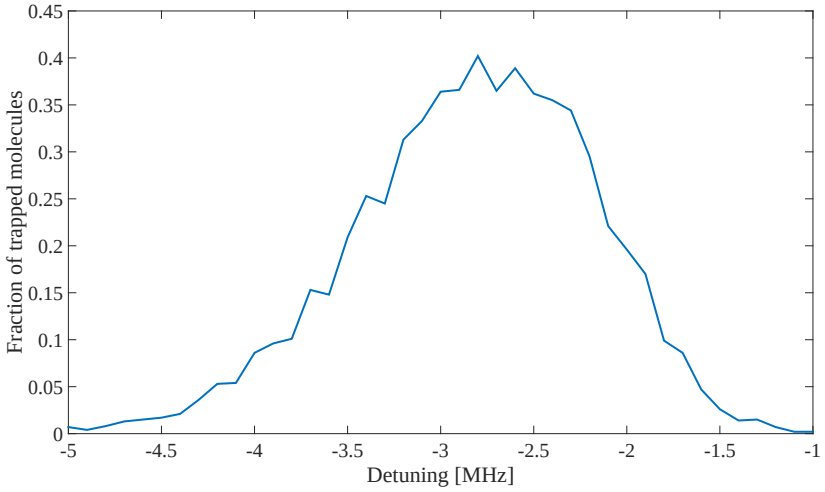

Figure 3.16: *The fraction of molecules that reach the recoil velocity, as function of the detuning of the pump laser. The random momentum kicks from scattering are neglected. The value -2.8 MHz is used as optimal parameter.*

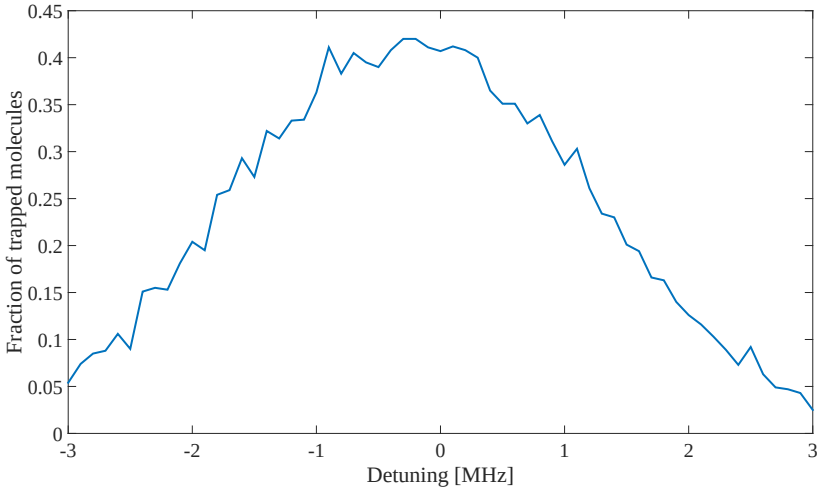

Figure 3.17: *The fraction of molecules that reach the recoil velocity, as function of the detuning of the first repump laser. The random momentum kicks from scattering are neglected. The value -0.3 MHz is used as optimal parameter.*

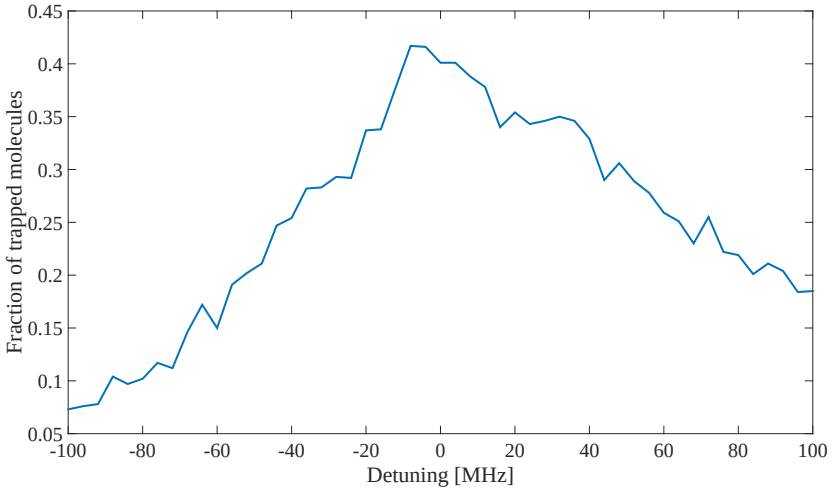

Figure 3.18: *The fraction of molecules that reach the recoil velocity, as function of the detuning of the second repump laser. The random momentum kicks from scattering are neglected. The value 0 MHz is used as optimal parameter.*

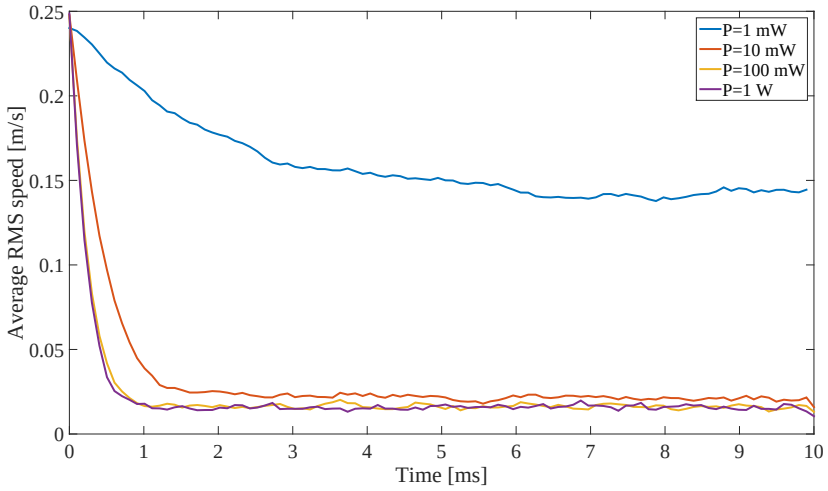

Figure 3.19: *The decrease in velocity for several powers per sideband of the laser beam.*

is very low, lower than the Doppler limit. The model makes use of an average laser cooling force and a velocity kick in random directions for the spontaneous decay. In reality the scattering force is not an average force but a kick with a higher probability in the anti-parallel direction than the parallel direction. Probably here the model goes wrong. When the velocity is cooled down close to the Doppler limit ($v_{\text{mean}} = 0.2$ m/s), the random scatterings become more important and here the model might be wrong. In my model the lower powers obtain a higher temperature than the higher powers. In theory [37, 46] the Doppler limit can only be reached for low powers.

The average laser cooling force for velocities much higher than the Doppler limit is valid so the model is useful for obtaining the time needed to reach the laser cooling limit. For 10 mW this is around 1 ms and it took 2.8×10^3 scatterings. The chance to loose a molecule to the $v \geq 3$ is 5.1×10^{-3}%. Without the second pump laser the loss to the $v = 2$ is 7.2%.

Figure 3.20 shows a histogram of the number of molecules at their average distance (RMS) to the center at 0 ms, 1 ms, 2 ms and 3 ms for 10 mW laer

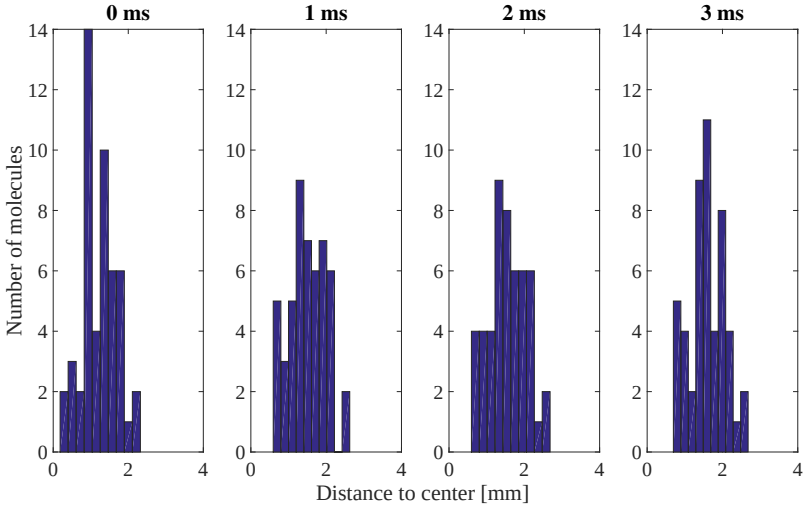

Figure 3.20: *The average distance (RMS) for a sample of 50 molecules to the center during laser cooling at 0 ms, 1 ms, 2 ms and 3 ms. This is for a laser power of 10 mW. The average distance to the center of the trap for all molecules did not increase after 3 ms.*

power. In the first millisecond the molecular sample is expanding but when the final temperature is reached, the cloud size remains constant. Because we already start with a low velocity spread before laser cooling is applied, all molecules will be cooled and the diameter of the molecular sample is very small. Other experiments where laser cooling is applied directly after a cryogenic buffer gas cell have more problems with a very divergent beam diameter [45, 53, 79]. Recently the first 3D MOTs have been established [46, 82, 83]. This is also a way to decrease the volume of our molecular sample.

3.5 Magneto-optical trap

A magnetic field can be applied to the optical molasses to create a position dependent trap: a magneto-optical trap (MOT). Two coils in anti-Helmholtz configuration create a magnetic field with $B = 0$ at the center. The Zeeman effect causes a position dependent energy shift. Particles that move away from the trap center can be excited by circularly polarized, red-detuned,

counter-propagating laser light. The force on the molecule depends on the magnetic field and the velocity. The force in one direction is given by [80, 113]:

$$F_{\pm} = \frac{\hbar k \Gamma}{2} \frac{s}{1 + s + 4(\Delta_0 \pm kv \pm 2\mu A r/\hbar)^2/\Gamma^2}, \tag{3.19}$$

where A is the gradient of the magnetic field, μ is the differential magnetic moment between the ground and excited state, and r the distance between the particle and the center. Adding the two forces, for low laser intensities this will be [80]:

$$\vec{F}_{OM} = -\alpha v - \omega^2 r, \tag{3.20}$$

where

$$\alpha = \frac{8 s \hbar k^2 \Delta_0}{\Gamma(1 + s + 4\Delta_0^2/\Gamma)^2} \tag{3.21}$$

and

$$\omega^2 = \frac{16 k s A \mu \Delta_0 m}{\Gamma(1 + s + 4\Delta_0^2\Gamma^2)^2}. \tag{3.22}$$

In traditional atomic MOTs (called type-I) the excited states have a higher quantum number than the ground states. Most laser coolable molecules have this the other way around [77], so dark states have to be remixed. Also the number of ground states is therefore higher, which decreases the laser cooling force. Most laser coolable molecules use the $A^2\Pi_{1/2}$ excited state, which has a very small g-factor. Due to this the laser cooling force is very small [113]. Also for the laser cooling of molecules there is always a leak to higher vibrational states.

The first molecular MOT was made in 1D and 2D using YO [80]. Dark states are coupled to bright states by switching the polarization of the light and the magnetic field synchronously at a rate of 2 MHz. Due to the 1D MOT trapping force the temperature decreased from 25 mK to 2 mK. For 2D the force is lower because the scattering rate has to be divided over two directions. The limitation in temperature is due to the interaction time.

Barry et al.[82] made the first 3D-molecular MOT for SrF in 2013. The final temperature they obtained is approximately 2.5 mK and there were around 300 molecules in the MOT. They used four laser sidebands with

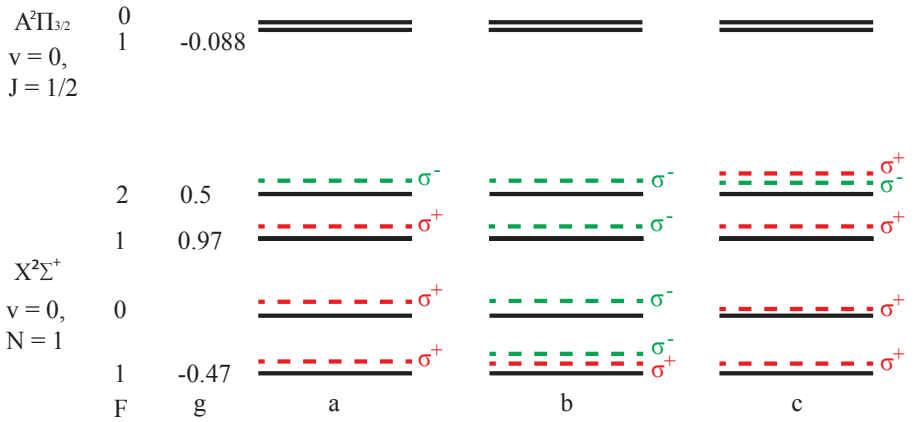

Figure 3.21: *(a)The ideal polarizations of the laser beams for a MOT of SrF. (b) The polarization used for the first MOT [82]. (c) A better way to use the polarizations in a relatively simple experimental setup. This Figure is adapted from Tarbutt [113].*

one circular polarization, and an extra laser beam with opposite circular polarization for the $|J, F\rangle = \left|1/2, 1\right\rangle$ state, see Figure 3.21 (ii). Simulations of Tarbutt [113] show that the Zeeman splitting in the excited state is very important. For SrF the Zeeman shift in the $A^2\Pi_{1/2}$-state is very small because the Λ and Σ part of the g-factor have the same size and are in opposite direction [82] (see also Chapter 2). Due to mixing of the $A^2\Pi$ state with the $B^2\Sigma^+$-state a small magnetic field dependence is induced in the excited state, which causes a weak trapping force. Tarbutt [113] suggested to make a stronger MOT force by using opposite polarization for the $\left|3/2, 2\right\rangle$-state, see Figure 3.21. McCarron et al. [83] followed up on this and the number of molecules increased to ~ 500. However, this resulted in a temperature increase to 12(2) mK, caused by unknown effects. Stronger MOT-forces could be obtained by using only the required polarization for every separate laser sideband. This is more difficult in practice. A good solution for the lack of Zeeman shift in the excited state is to use the polarization switching of Hummon et al. [80]. Norrgard et al. [46] followed up on this, which has resulted in the demonstration of a significantly improved MOT. The lowest temperature obtained is ~ 400 μK and the number of trapped molecules has increased to around 2000.

3.6 Losses

Except for the main losses to vibrational levels and dark states, molecules can be lost from the optical cycle in many other ways [108]. With one repump laser (see chapter 4) the decay to the $v = 2$ vibrational state has a probability of $4{\times}10^{-4}$. The magnetic dipole transitions of the $A^2\Pi \rightarrow X^2\Sigma$ system are only three orders of magnitude smaller than the electric dipole transitions [68]. This is not included in my model but should not be neglected if more scatterings are required. Magnetic dipole transitions have other selection rules, so there are decay possibilities to the $N = 0$ and $N = 2$. Microwave transitions between these states and the $N = 1$ can pump the molecules back into the laser cooling cycle. Thereby the number of ground states increases and the laser cooling force decreases.

Barry [108] calculated also that losses to other rotational numbers can occur because of the (small) magnetic fields, for off-resonant excitation, level-mixing due to stray magnetic fields, hyperfine and spin-rotation level-mixing, stimulated absorption of black-body photons, spontaneous vibrational decay and due to light-assisted collisions and quadrupole decays. These losses are very small ($< 10^{-7}$). Also level-mixing due to stray electric fields causes losses to other rotational states.

3.7 Other experiments combining the traveling-wave decelerator with lasers

We can make use of the almost closed cycle of SrF in other ways than only applying laser cooling at the end of the decelerator. We have considered various options, which are summarized in the following sections.

3.7.1 Reduced velocity spread in the source chamber

By performing numerical simulations, Aernout van der Poel [127] investigated the possibility to use laser cooling for the reduction of the transverse velocity spread of the molecular beam in between the source chamber and the decelerator. Potentially, more molecules could make it through the skimmer and would be decelerated. The conclusion of this research was that a maximum gain of about 50% could be achieved. The main reason for this

modest estimated increase in the number of molecules is the limited scattering rate in combination with the longitudinal velocity of the molecular beam. As a result, the molecular beam would spread out in the transverse direction significantly during laser cooling. The transversely cooled beam would simply be too large to be captured efficiently by the decelerator.

The application of transverse laser cooling *following* the deceleration is much more attractive, since the reduced velocity makes that the required interaction time to cool the transverse velocity happens in a much more compact interaction zone. The resulting slow molecular beams with high brightness are expected to enable a next generation of precision measurement to test the Standard Model of particle physics. The reason is that these beams open the way to long coherence-time measurements with minimal losses in particle number, which is highly promising for example in measurements of the electric dipole moment of the electron (eEDM) [128].

3.7.2 Laser beam longitudinal to the decelerator

It is natural to consider the combination of deceleration and longitudinal laser cooling. However, we quickly see that in it is simplest implementation, this combination will not work. The molecules are kept together by the electric fields during deceleration only as long as they remain in a low-field seeking state. If we would apply a counter-propagating laser beam to assist in the removal of kinetic energy *during* the deceleration process, the molecules would quickly be optically pumped to high-field seeking states, resulting in major losses in the number of molecules, and a very limited reduction of the kinetic energy. Both laser cooling and the deceleration would cease to work. Furthermore, laser cooling during the deceleration process is challenging because the electric fields of the decelerator shift and broaden the resonance frequency of the cooling transition. In the next section on Sisyphus cooling we discuss an option to turn these shifts into an advantage and exploit them for a new cooling mechanism.

The special properties of the molecular beams that are created by the decelerator might nonetheless be of interest for laser cooling. The decelerator can be seen as a device that 'purifies' the molecular beam, since it is very selective for the quantum state (down to the hyperfine level) and the velocity of the beam. The localized packets of molecules that are created

by the decelerator even if the average velocity of the beam is not changed (during guiding operation) are ideal starting points for experiments to quantify the effects of photon scattering. It is clear from recent results on the laser cooling and trapping of SrF molecules [46] that even though great progress has been made, aspects of the main cooling mechanisms (such as the correct prediction of the temperatures reached) are still far from fully understood. It is worthwhile to consider a series of carefully controlled experiments, using these packets of molecules with a tunable velocity, to reach an understanding of the light-molecule interaction at a quantitative level.

3.7.3 Sisyphus cooling

When static electric fields are applied to the decelerator electrodes a sinusoidally varying electric field can be created along the decelerator axis. Using an intense counter propagating laser beam, molecules could be pumped into a high-field seeking state at an electric field maximum, and into a low-field seeking state at an electric field minimum. If the internal state is switching in this way the molecules will always have to climb a potential hill, and as a result they will continuously loose kinetic energy. Inspired by the presentation of the magnetic equivalent of this process at a Zeeman deceleration workshop in Zürich by Daniel Comparat in april 2012, A.P.P. van der Poel [127] and T.H. Nijbroek [129] have performed numerical simulations of this process. In [127] the simulations indicated that a small deceleration could be achieved when the loss due to the transverse momentum spread was neglected. In [129] other waveforms were tried and more realistic laser powers were taken into account. One of the most challenging aspects turned out to be the loss of molecules from the beam due to the transverse velocity spread. Only for very specific electric field configurations the transverse instability was found to be sufficiently small, and still then, only molecules with a transverse velocity below 1 m/s would make it through a 5 meter long Sisyphus decelerator, while their longitudinal velocity for our typical field strengths was reduced from 370 m/s to 290 m/s. This challenge of the stability turns out to be much smaller in the magnetic version, experiments on which are currently underway in Paris [130] and London [131].

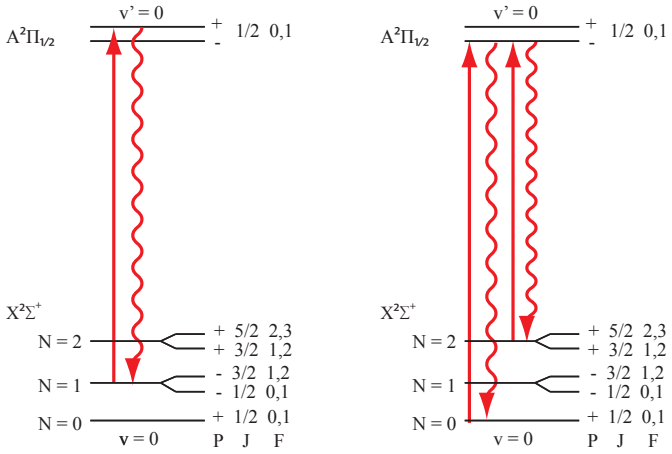

Figure 3.22: *The rotationally closed cycles for $N = 1$ and the $N = 0$ with $N = 2$ cycle.*

3.7.4 Laser cooling from $N = 0$ and $N = 2$ to $J' = 1/2$

Another (almost) closed transition can be made when using the $N = 0$ rotational line [120]. This line has the opposite parity to the $N = 1$. From the excited state ($J' = 1/2$) a part ($1/3$) will decay to the $N = 2$. A picture of both cycles is shown in Figure 3.22. There are in total 5 hyperfine states involved, the decay to $J = 5/2, F = 3$ is forbidden. The two $F = 2$ states mix with each other because the hyperfine interaction is not diagonal in J. Laser cooling using the $N = 1$ rotational level is at first sight easier because only four hyperfine states are involved. For other molecules with different energy splittings this might be useful to keep in mind.

3.7.5 Laser cooling from the $A^2\Pi_{3/2}$-state

MOT forces on the $A^2\Pi_{1/2} \rightarrow X^2\Sigma^+$ transition are very weak because the Zeeman shift of the excited state is very small [113]. The Zeeman shift in the $A^2\Pi_{3/2}$-state is larger ($g \sim 2$) so for the MOT this is better. The potential curve of the $A^2\Pi_{3/2}$-state is very similar to the $A^2\Pi_{1/2}$-state, so the Franck-Condon factors are almost the same. The energy of the $\Pi_{3/2}$ is slightly higher, so there is a very small leak to the $A^2\Pi_{1/2}$. The lowest

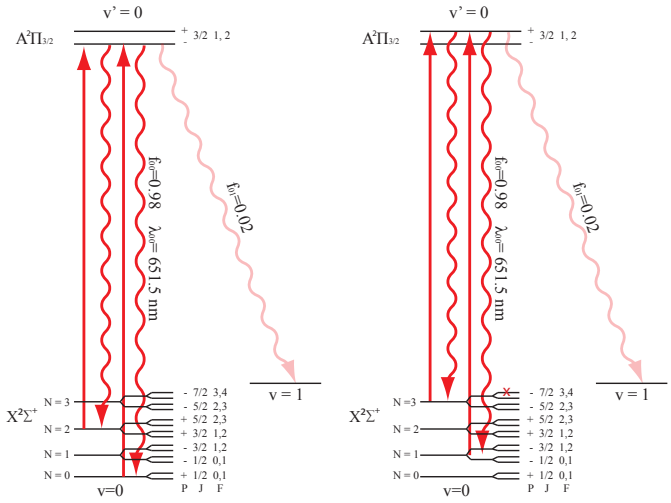

Figure 3.23: *The rotationally closed cycles for the* $^2\Pi_{3/2}$*-state. The molecules can decay to the N=1 but also to the N=3 level. The cycle is closed with an additional laser.*

rotational number has $J' = 3/2$. This decays to the $N = 1$ states but also to the $N = 3$, $|J, F\rangle = \left|5/2, 3\right\rangle$, $\left|5/2, 2\right\rangle$and $\left|7/2, 3\right\rangle$ state. An extra laser beam is required to close the cycle. For SrF the Λ-doubling in this state is very small. Hereby the parity is mixed and the parity selection rules are not working. Rotationally the system can leak to other states. For other molecules this might be interesting.

3.7.6 Repumping from $v = 1$ to $v' = 1$

When the molecules in the $v = 1$ state are pumped to the $v' = 1$ level instead of the $v' = 0$ level, the scattering rate will increase (from $R_{\max} = \Gamma/7$ to $\mathrm{R}_{\max} = \Gamma/4$) and the loss will be 25 times higher than before (3.29×10^{-5} vs $3.29 \times 10^{-5} + 0.0205 \times 0.0405 = 8.6 \times 10^{-4}$). The saturation intensity is $\sim 50\times$ higher the transitions are weaker.

3.7.7 Laser cooling with π-pulses

Another way to use laser cooling, is to apply optical bichromatic forces (BCF) [132, 133]. π-pulses make exactly half a Rabi-oscillation, so that all molecules are pumped into the excited state. This gives a momentum kick. From the other side, at the right time comes another π-pulse to pump all molecules back into the ground state. The Rabi-cycle is much faster than the spontaneous decay of 'normal' laser cooling and the force of the laser beam is higher than in 'normal' laser cooling: $F_{BCF} = \hbar k\delta/\pi$ in stead of $F_{rad} = \hbar k\gamma/7$. The limiting factor of the detuning will be the laser power: $I_b = 3(\delta/\gamma)^2 I_s$. The capture velocity can be a lot higher: $v_b \simeq \delta/k$. For CaF the required power will be 60 W/cm^2 per sideband for a capture velocity of $v_{\rm cap} = 150$ m/s. For SrF most numbers are more or less the same.

3.8 Laser cooling of other molecules

There are more molecules than only SrF which can make many laser cooling cycles. There are many molecules that have highly-diagonal Franck-Condon Factors. Not all of these molecules are suitable for laser cooling, due to their transition rates, wavelength, losses to other electronic states, hyperfine splitting, available lasers for that wavelength, production difficulties of the molecules etc. This section gives an overview of possible molecules for laser cooling.

The maximum force for laser cooling is:

$$\mathbf{F} = \hbar \mathbf{k} R_{\rm scatt} \propto \frac{\Gamma}{m\lambda} \times \frac{N_e}{N_g + N_e}. \tag{3.23}$$

The acceleration is maximally [112] eq. 9.5:

$$a_{\rm max} = \frac{h}{2\tau\lambda M}, \tag{3.24}$$

where M is the mass of the molecule. For simplicity the hyperfine splitting is neglected in this formula. The hyperfine splitting is a big disadvantage when a wavelength is red-detuned for one hyperfine state and blue-detuned for another level. When the splitting is so small that it does not effect the Doppler temperature or smaller than the natural linewidth, it is not a

problem. This importance also depends on the velocity of the molecules before laser cooling and that depends on the used experimental techniques. Some molecules have leaks to forbidden states. In the first place such a leak causes unwanted losses in the laser cooling cycle, but when the molecules are maximally laser cooled by the allowed transition, lower temperatures can be achieved using this leak [134].

Table 3.9 shows properties for laser cooling several molecules. The Franck-Condon factors are mostly theoretical predictions. The g-factors of the excited state are also important for a molecular MOT, but there is no simple relationship with the force. The molecules can be divided into a few groups: the alkaline-earth hydrides, the alkaline-earth monohalides, the atoms of group 13 with H or F, some chlorides and bromide and atoms in group 3 and 4 with oxygen. I could not place NH, SiH and SiF in a group but I found highly-diagonal Franck-Condon Factors. I also included molecules with a high nuclear spin. There are many hyperfine levels which all have to be addressed by laser frequencies.

Molecules that would also fit in the list above are BeF and BF but their f_{00} are 0.897 [135] and 0.7885 [136] respectively. YbH, GaH, InH and AlCl could also fit in the list but I could not find their Franck-Condon factors. I could not find enough information about InF and LuO. Stuhl [78] mentioned also FeC, ZrO, HfO, ThO and SeO in the metastable state. Besides laser cooling of TiO using the $E^3\Pi_0 \rightarrow X^3\Delta_1$ transition, he also mentioned TiS.

There are more molecules suitable for laser cooling than only the alkaline-earth monohalides. The advantage of alkaline-earth monohalides, alkaline-earth hydrides and the group-3 oxides, ScO, YO and LaO, is that only one atom has a nuclear spin, which makes laser cooling less complicated than two atoms with nuclear spin. The group-13 halides and group-13 hydrides have a more favorable electronic system ($^1\Pi \rightarrow^1 \Pi$), which has less dark states and the excited state has a Zeeman splitting, in contrast to the $\Pi_{1/2}$ state. In general lighter molecules require less photon scatterings compared to heavier molecules. Using laser cooling for a nuclear spin dependent-parity violation test, I would not prefer the alkaline-earth monohalides with an-

other isotopes with nuclear spin, but for example a group-3 oxide. Here the nuclear spin belongs to the heavy nucleus.

3.9 Summary

We have used the multi-level rate equations to simulate the interaction of light with SrF molecules. Simulations of the detection downstream ofthe traveling-wave Stark decelerator are shown for several settings. The scattering force for several parameters are simulated. For the 3D laser cooling downstream of the decelerator the molecules are standing still with a maximum velocity spread of 2 m/s. The Monte Carlo method is used to randomly choose the initial conditions for laser cooling. Simulations show that with 10 mW per sideband, the molecules are cooled down to the Doppler limit in 1 ms and 3 $\times 10^3$ photon scatterings. For 2D cooling we can use a slow beam of molecules that can be cooled transversely. With a repetition rate of 10 Hz and 10^3 molecules per shot [44] very attractive conditions are created to perform a high-precision measurement on a slow, cold and intense molecular beam.

Table 3.3: *Several molecules with their properties relevant for laser cooling.*

Molecule	transition	FCF00	λ [nm] [137]	τ [ns]	I_1, I_2	m [amu]	a [km/s^2]	Leak
BeH	$A^2\Pi \rightarrow X^2\Sigma^+$	.998 [138]	497 [138]	82.0 [138]	3/2, 1/2	10	140	
MgH	$A^2\Pi \rightarrow X^2\Sigma^+$	.954 [138]	526 [138]	48.6 [138]	0, 1/2	25	89.2	
CaH	$A^2\Pi \rightarrow X^2\Sigma^+$	.961 [138]	693 [139]	33 [140]	0, 1/2	41	61	
SrH	$A^2\Pi \rightarrow X^2\Sigma^+$	.978 [138]	740	33.2 [138]	0, 1/2	89	26.1	
BaH	$A^2\Pi \rightarrow X^2\Sigma^+$	.9943 [141]	1057 [141]	68.6 [138]	0, 1/2	139	5.66	
BH	$A^1\Pi \rightarrow X^1\Sigma^+$	.9863 [109]	433 [142, 143]	127[144]	3/2, 1/2	12	202	yes
AlH	$A^1\Pi \rightarrow X^1\Sigma^+$	.9658 [111]	426 [111]	66 [145]	5/2, 1/2	28	169	yes
MgF	$A^2\Pi \rightarrow X^2\Sigma^+$	.986 [146]	359	7.16 [146]	0, 1/2	43	516	
CaF	$A^2\Pi \rightarrow X^2\Sigma^+$	.964 [81, 120]	606 [81]	19.2 [120]	0, 1/2	59	83.1	
SrF	$A^2\Pi \rightarrow X^2\Sigma^+$	.98 [79]	663 [123]	24.1 [123]	0, 1/2	107	33.4	
BaF	$A^2\Pi \rightarrow X^2\Sigma^+$	.960 [126]	860 [125]	56.0 [124]	0, 1/2	157	7.54	
YbF	$A^2\Pi \rightarrow X^2\Sigma^+$	.928 [148, 37]	552 [150]	28 [150]	0, 1/2	193	19.1	
RaF	$A^2\Pi \rightarrow X^2\Sigma^+$	high [1][51]	$\sim$710 [51]	$\sim$25 [51]	0, 1/2	245	13.1	
AlF	$A^1\Pi \rightarrow X^1\Sigma^+$	.99991 [111]	227 [111]	1.8 [110]	5/2, 1/2	46	7.1×10^3	yes
GaF	$A^1\Pi \rightarrow X^1\Sigma^+$	.997 [110]	209 [110]	2.26 [110]	3/2, 1/2	88	3.20×10^3	yes
TlF	$B^3\Pi_1 \rightarrow X^1\Sigma^+$[2]	.989(2) [151]	272 [151]	99 [151]	1/2, 1/2	224	22.1	yes

Continued on next page

[1]The internuclear distance of RaF is not known very precise. The Franck-Condon factors depend on that. The probability is higher than 0.9999 to decay from $v' = 0$ to the first three vibrational states [51].

[2]I did not take into account all other molecules with this transition because it is forbidden. I only mention TlF because it is proposed for laser cooling [151].

Table 3.3 – *Continued from previous page*

Molecule	transition	FCF00	λ [nm] [137]	τ [ns]	I_1, I_2	m [amu]	a [km/s^2]	Leak
BCl	$A^1\Pi \rightarrow X^1\Sigma^+$	.959 [152]	268 [152]	17.1 [152]	3/2, 3/2	46	631	yes
BBr	$A^1\Pi \rightarrow X^1\Sigma^+$	.974 [152]	289 [152]	31.1 [152]	3/2, 3/2	90	165	yes
ScO	$A^2\Pi \rightarrow X^2\Sigma^{+3}$	.941 [153]	610 [155]	?	7/2, 0	61		yes
YO	$A^2\Pi \rightarrow X^2\Sigma^+$	.995 [80]	614 [80]	33[156]	1/2, 0	105	26.8	yes
LaO	$A^2\Pi \rightarrow X^2\Sigma^+$	.96173 [154]	791 [155]	?	7/2, 0	155		?
TiO	$E^3\Pi_0 \rightarrow X\ ^3\Delta_1$	.845 [78]	845 [157]	4.9μs [158]	0, 0	64	0.50	yes
HfO	$A^1\Pi \rightarrow X^1\Sigma^+$	.924 [159]	602 [159]	?	0, 0	228		
NH	$A^3\Pi \rightarrow X^3\Sigma^-$	.99989 [160]	336 [162]	470 [161]	1, 1/2	15	25.1	yes
SiH	$A^2\Delta \rightarrow X^2\Pi$	.994 [163]	413 [164]	534 [165]	0, 1/2	29	8.92	
SiF	$A^2\Sigma^+ \rightarrow X^2\Pi$	.98710 [136]	439 [166]	0.23μs [168]	0, 1/2	47	12	

[3]For ScO, $A^2\Pi_r$ can decay to $X^2\Sigma^+$ and $A'^2\Delta_r$. The transition between Σ and Δ is forbidden. The energy splitting between $A^2\Pi$ and $A'^2\Delta$ is 1533 cm^{-1} [169] so there is mixing. In the first place this might be less suitable for laser cooling but this might be interesting for molecular clocks.

4 | Experimental setup

In our experiment, SrF molecules are produced in a source chamber and they enter the traveling-wave Stark decelerator by a pulsed supersonic expansion. The molecules can be accelerated, decelerated or guided at constant velocity by the decelerator. At the end of the decelerator molecules are detected by laser induced fluorescence. In future experiments, when molecules are decelerated to stand still, they can be further laser cooled. To provide optical access for laser beams for laser cooling, a very open electric trap is designed. This trap is an extension of the decelerator and besides laser cooling the molecules can be detected in this trap and there is space for an optical dipole trap. A schematic overview is shown in Figure 4.1.

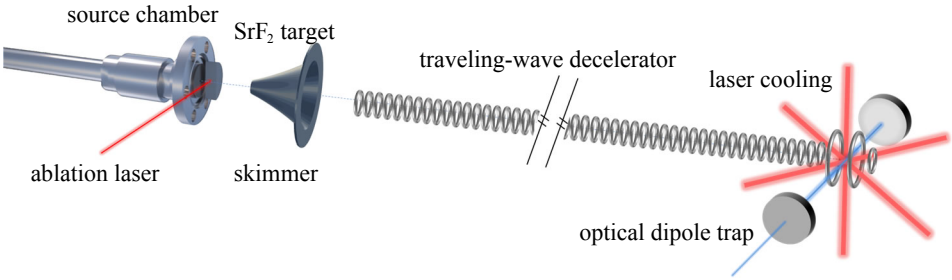

Figure 4.1: *A schematic overview of the setup to decelerate and trap SrF.*

In this chapter an overview of this experimental setup is given, that has been designed and built in a joint effort during my PhD period. Special attention is being paid to two topics that I did most work on: the design of the trap and the setup and operation of the laser system.

4.1 Source chamber

SrF molecules are formed by laser ablation of a homemade tablet of SrF_2 containing additional boron (with mass ratio 9:1) [170, 171, 172]. A high-intensity pulsed Nd:YAG laser is used for ablation. A mix of atoms, ions and molecules is evaporated from the pill. The power of the YAG laser is around 100 mJ per pulse of 5 ns at 1064 nm with a repetition rate of 10 Hz. A supersonic expansion of Xe gas collects the molecules and brings them forward in the lower rovibrational states. This results in a velocity of $\sim$ 370 m/s with 10% velocity spread. The gas flow is regulated by a magnetic pulsed valve. The valve has been modified so that it can be cooled to around -30 °C using cold nitrogen gas, which reduces the average forward velocity down to 280 m/s.

4.2 Stark deceleration

Stark deceleration makes use of the Stark effect of molecules in an external electric field. In the traveling-wave Stark decelerator, electric field minima and maxima are created. This is shown in Figure 4.2. Molecules in the low-field seeking state are attracted to the electric field minima. The electric field minima initially move with the same speed as the molecules and are then slowed down in time. Low-field seeking molecules within the velocity acceptance of the decelerator remain trapped in the electric field minima during deceleration, and are in this way brought to lower velocities. High-field seeking state molecules gain kinetic energy and lose potential energy in electric field minima. They are attracted to electric field maxima, at the sides of the decelerator. In Figure 2.8 of Chapter 2 the Stark shifts of the lowest rotational states of SrF are shown. The states (N, M_N)=(1,0) and (2,0) are low-field seeking at electric fields smaller than resp. 20 kV/cm and 60 kV/cm. Of the (1,0) state, a quarter of the hyperfine states is low-field seeking and three quarter of the states high-field seeking. In Chapter 5 it is described how to increase the number of low-field seeking molecules by optical pumping of high-field seeking states.

The traveling-wave Stark decelerator consists of a sequence of ring electrodes where a high-voltage is applied onto. Electric field minima are created by a sinusoidal input, so that a 3D electric trap is formed. A 2D plot

is shown in Figure 4.2. It should be pointed out that this is not directly the potential curve for the molecules; the potential is obtained by the convolution of the electric field with the Stark curve of the particular state of the molecule that is being used. Of particular importance is the fact that SrF in the (N,M)=(1,0) state makes a transition from low-field seeking to high-field seeking around an electric field strength of 25 kV/cm.

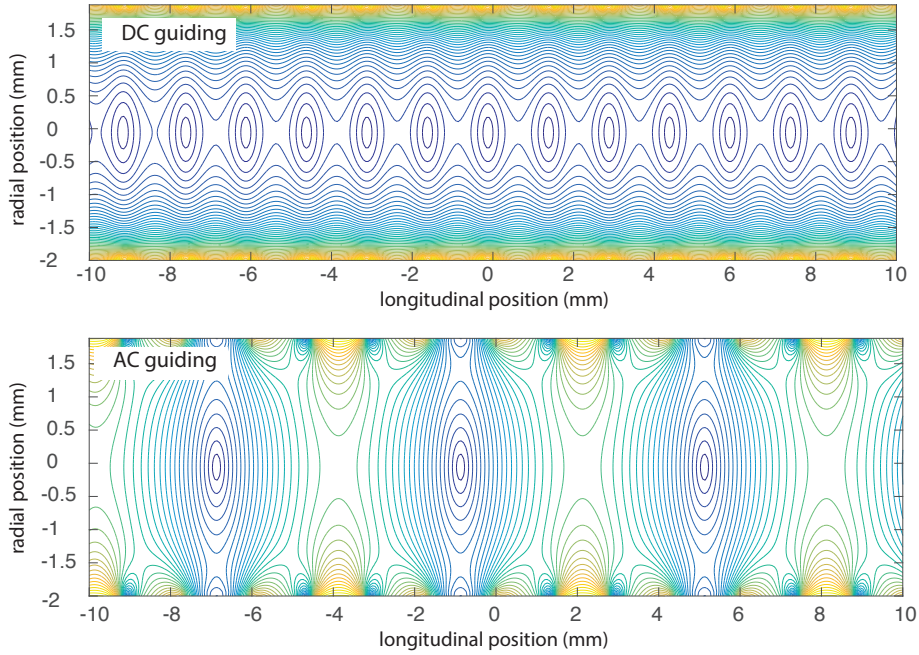

Figure 4.2: *Lines of equal electric field strength illustrate the shape of the electric field in this cross section of the decelerator for two different modes of operation, DC guiding (top) and AC guiding (bottom). During DC guiding mode static voltages on the rings lead to strong transverse confinement. In AC guiding mode the distribution of the voltages leads to larger stable traps that also have strong confinement in the longitudinal direction. In this example the amplitude of the voltages in both modes is the same.*

Another mode of operation that was used in the experiments described in this thesis is called DC-guiding. Instead of moving electric field minima, the high-voltages are static in time. The electrodes are connected to either a positive or a negative static voltage in an alternating way. The electric field

minimum is now spread along the decelerator. This is shown in Figure 4.2. Low-field seeking molecules will be guided through the decelerator. Longitudinally the molecules are not bunched as in the AC mode. The molecules have a much larger longitudinal velocity spread compared to AC-guiding. DC-guiding can be obtained from simple electronics. This is used for the hyperfine pumping experiment, Chapter 5. For the hyperfine pumping experiment only the total number of molecules is counted. The systematical error would have been smaller when using AC-guiding, because the background for AC-guiding is smaller.

One of the modules of the decelerator is shown in Figure 4.3. More about the principle of such a decelerator can be found in [44, 57, 69, 70, 48]. A detailed description of our decelerator can be found in [44].

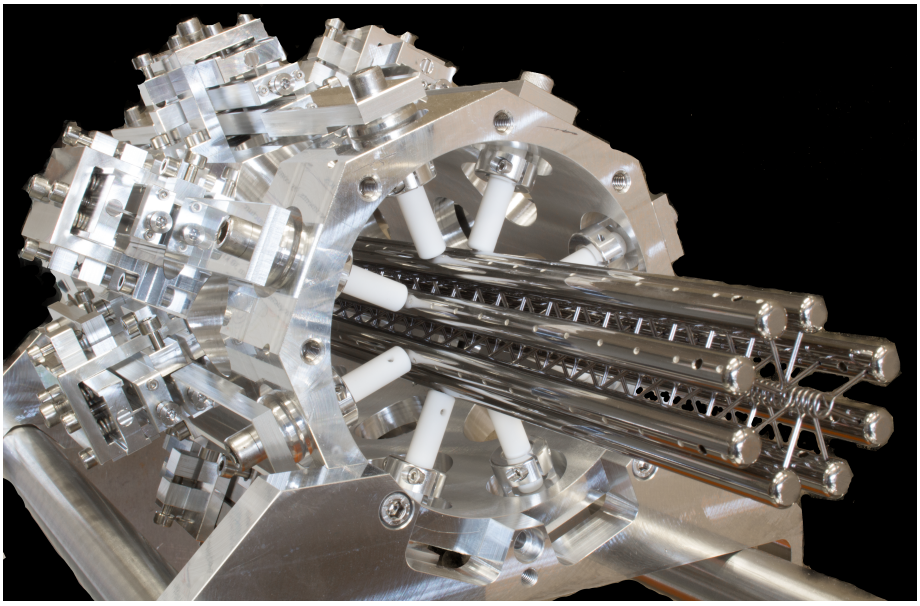

Figure 4.3: *This assembly of eight rods, each containing 42 ring-shaped electrodes, is a single module of the ring decelerator with a length of 50 cm.*

For the deceleration of molecules with an initial velocity of 300 m/s in a 5 meter long decelerator, a deceleration strength of ~ 9 km/s^2 is required. When decelerating, the phase-space acceptance is reduced compared to

guiding. This is illustrated for the longitudinal phase-space acceptance in Figure 4.4 for various deceleration strengths. At 9 km/s^2, only molecules moving within ± 2 m/s of the selected initial longitudinal velocity are decelerated in a phase-stable way. Since the deceleration is directed along the axis of the decelerator, the transverse acceptance is not directly affected. The motion in the longitudinal and transverse direction is coupled however, and ultimately the total acceptance is limited by the lowest point of the potential, which is in the longitudinal direction. As a result, only molecules within a distance of ∼ 1 mm to the center of the traveling minimum — and therefore the center of the decelerator — are being decelerated. The deceleration data is shown in Figure 4.22. Simulations were done by J.E. van den Berg [48]. More information about the deceleration is given in the PhD thesis of J.E. van den Berg [44] and the papers about simulations and measurements with 2m of deceleration [48, 57].

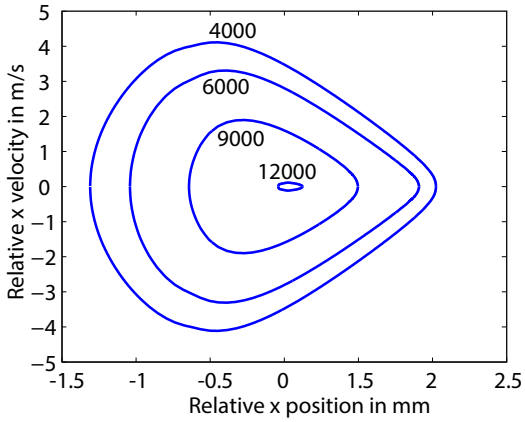

Figure 4.4: *The longitudinal phase stable area of the traveling-wave decelerator for several deceleration strengths (in m/s^2).*

4.3 End trap

The molecules are already trapped in the traveling-wave decelerator, but in order to be able to do laser cooling more optical access is required. To give access to the laser beams, an extension of the traveling-wave decelerator is designed. Molecules are trapped in this extension by electric fields which

can be switched off to allow for laser cooling in a field-free environment. When the electric fields in the trap are not switched off, molecules in low-field seeking states are attracted to the center of the trap while molecules in the high-field seeking states are attracted to the sides of the end trap. We have designed the extension to have an electrode geometry that allows for laser cooling in two or three perpendicular directions. 2D cooling can be used for beam experiments with a very small transverse velocity. 3D cooling can be done to trap the molecules in all directions. In Chapter 3 more is explained about laser cooling.

For the best electric trap, some parameters are conflicting each other. For example there has to be enough space between the electrodes to give optical access. But at constant voltage the further the electrodes are away from each other, the shallower the trap will be. To compensate for this, the voltages have to be increased to maintain the same trap depth. Too high voltage differences can cause sparks or can not be made by the electronics. We designed an electric trap aiming for an optimal compromise between all the requirements.

As can be seen from Figure 4.4, the maximum accepted velocity for the deceleration at 9 km/s^2 is 2 m/s. For SrF molecules the kinetic energy of 2 m/s corresponds to the stark shift at an electric field of 400 V/mm. Molecules are trapped within these gradients.

Beforehand it is decided to give optical access for three orthogonal laser beams with a diameter of 5 mm. 5 mm is decided because molecules inside the decelerator are distributed in a volume of $0.8 \times 1.6 \times 1.6$ mm^3. The decelerator electrodes have a diameter of 4 mm. When the trap is turned off, the molecules spread out. It is difficult to send two laser beams (anti)-parallel to the beam axis. Therefore a configuration is chosen where two laser beams make an angle of ~ 45 degrees to the beam axis. The third laser beam can be perpendicular to the decelerator. With at least one laser beam perpendicular to the decelerator, a logical design is to have two rings where laser beams can access perpendicular to the decelerator. For 3D laser cooling the access for one laser beam axis is perpendicular to the beam axis and in the first try the two other laser beams make an angle of 45 degrees, such that the three beams are orthogonal. With this composition the large

ring is too far away from the decelerator rings to make a deep enough trap. At an angle of 52 degrees between the laser beams and the decelerator axis, the trap is deep enough. For this the two rings of the trap have to be larger than the other decelerator rings. The voltages in the two large electrodes have to be 10 kV for a deep enough trap. Therefore a thickness of 1 mm is chosen for the two large rings. The electric trap can only exist (in the center of the two large rings) with an additional electrode at the end. We chose an electrode with the same size as the decelerator electrodes: the electrode has the largest diameter such that the solid angle for laser induced fluorescence (LIF) is the largest, but it still gives optical access for the laser beams.

Molecules can be detected by LIF by placing a PMT downstream of the decelerator and the end trap. For 2D laser cooling both beams are orthogonal to the PMT, for 3D cooling there is an angle, which can cause more background scattering. The solid angle is 0.30 sr. This is less than we have in the detection chamber (1.33 sr) which is explained in the Section Experimental Setup. When the end trap is implemented the velocity of the molecules can be reduced, which means that the number of scattered photons per molecule can be increased due to the longer interaction time. More is explained in Chapter 3. There is also optical access for a dipole trap.

Figure 4.5 shows the electrodes with electric field lines and the access of the end trap to laser beams through the two large rings. For 2D laser cooling two beams have access to the trap in between the large electrodes. For 3D cooling, one laser beam has access to the trap in between the large electrodes and the other two laser beams make an angle of 52 degrees with the beam axis and have access to the trap through the large electrode and the adjacent small electrode. The three beams are orthogonal. Figure 4.5 shows also the sizes of the electrodes and spacings. To supply the voltages to these electrodes, 3 additional separately programmable high-voltage amplifiers are required. Since the capacitance of the trap electrodes is much reduced compared to the decelerator, standard commercial amplifiers with a higher voltage output of $\pm$ 10 kV can be used, where for the decelerator we are limited to specially developed models that can supply $\pm$5 kV at most. All high-voltage amplifiers that we use have been obtained from TREK (www.trekinc.com).

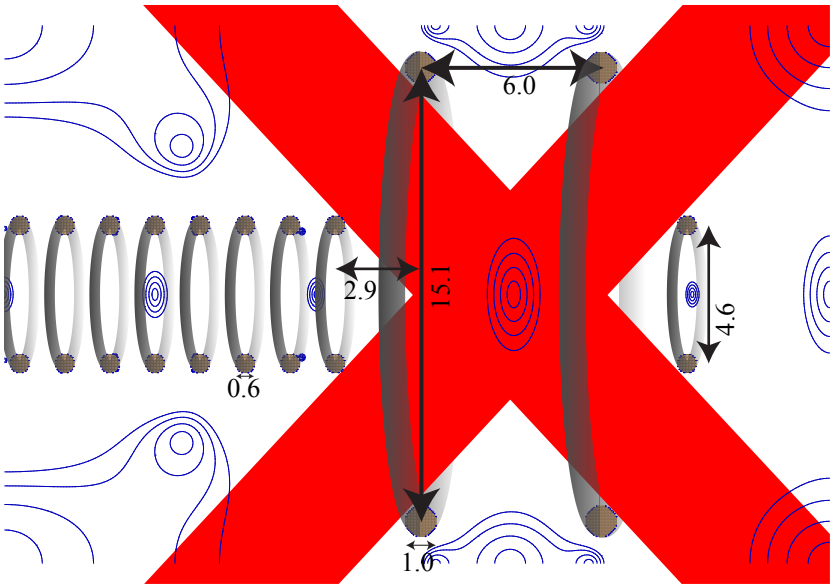

Figure 4.5: *The trap at the end of the decelerator. The extension of the decelerator consists of the two larger rings and an additional smaller ring. Due to this configuration three orthogonal laser beams with a diameter of 5 mm have access to the center of the trap. The blue lines are the contour lines of the electric field, lower than 400 V/mm. The sizes are in mm.*

The trap is designed in such a way that laser beams of 5 mm diameter have access in three orthogonal directions. The biggest challenge of the simulations was to find the combination of high-voltages to create a fluently moving trap, where the electric field did not come below 400 V/mm. A starting point was the continuation of the sinusoidal sequence. At several positions there was a sufficiently deep trap, at other positions fine-tuning was required. The voltages are optimized and a solution for a fluently moving trap is found. In Table 4.1 the voltages as a function of time are given of the last four electrodes of the decelerator (E1, E2, E3, E4), the two large rings (L1, L2) and the ring at the end (EE). Figure 4.6 shows the trap depth, distance to the trap center and the voltages as a function of time. In all situations the depth is higher than at deceleration. The trap depth is the lowest when the trap is in between of two electrodes, in between E4 and L1 and in between L1 and L2. The evolution of the electric field minima from the last part of the decelerator to the trap is shown in Figure 4.7.

Table 4.1: *The voltages for the transfer of molecules to the final trap at position $x = 0$. Columns denote for the last four decelerator electrodes, the two large rings and the end electrode. Figure 4.6 shows the voltages in steps for the seven electrodes.*

x(mm)	E1	E2	E3	E4	L1	L2	EE
5.9	-3530	0	3530	5000	5000	-10000	-5000
5.6	-4619	-1913	1913	4619	5000	-10000	-5000
5.3	-5000	-3530	0	3530	5000	-10000	-5000
5.0	-4619	-4619	-1913	1913	5000	-10000	-5000
4.9	-4619	-3000	-1000	3500	7500	-10000	-5000
5.2	-4619	-3000	0	5000	7000	-10000	-5000
4.8	-4619	-3000	0	5000	10000	-10000	-5000
4.0	-4619	-4619	-1913	1913	10000	-10000	-5000
3.7	-3530	-5000	-2500	1000	10000	-10000	-5000
2.9	-1913	-4619	-4619	-1913	10000	-10000	-5000
2.6	0	-3530	-5000	-3530	10000	-10000	-5000
2.1	3530	0	-3530	-5000	10000	-7500	-5000
1.1	3530	0	-3530	-5000	10000	0	-5000
0.5	3530	0	-3530	-5000	10000	5000	-5000
0.1	3530	0	-3530	-5000	10000	7500	-5000
0	3530	0	-3530	-5000	10000	10000	-5000

During the transfer of the molecules from the decelerator to the additional set of electrodes the volume of the trap increases. If this expansion of the trap volume is done sufficiently slow, i.e. on a timescale that is slow compared to the trap frequency, a process called adiabatic cooling takes place. It is essentially a rotation of the phase-space distribution where velocity is reduced at the expense of an increase of the size of the trapped cloud. There is no dissipative process; so strictly it is not a cooling process in the sense that energy is removed. The average velocity of the trapped cloud of molecules is reduced during its expansion, however, the temperature used to describe this velocity distribution is therefore 12 mK. This process has been demonstrated to work on CH_3F molecules [173] trapped in a micro structured trap, and recently on NH_3 and ND_3 molecules using

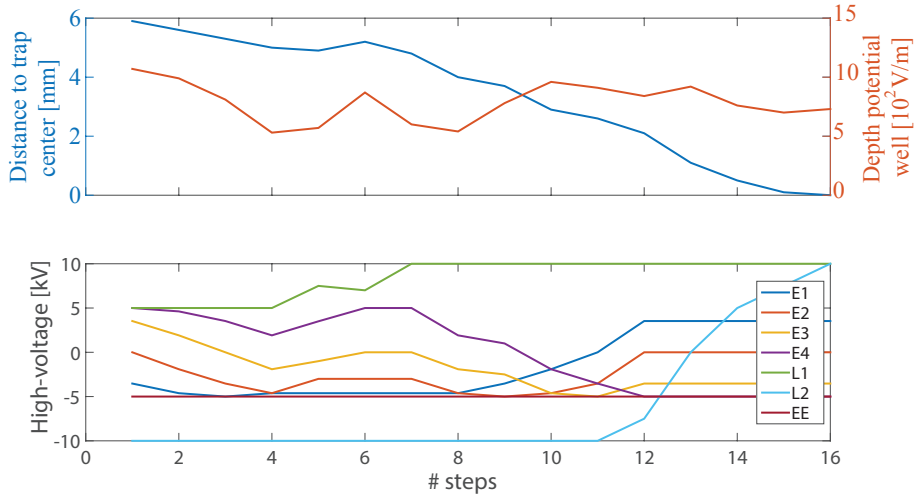

Figure 4.6: *The upper part shows the trap depth and distance to the trap center as function of the step number. The lower part shows the voltages of the last electrodes of the decelerator, shown in Table 4.1.*

our traveling-wave decelerator in a collaboration of our group with the VU Amsterdam [42, 43, 174].

Here we estimate how much the temperature would be lowered in our situation. In adiabatic cooling, the ratio of initial and final temperature is related to the ratio of final and initial volume through the following relationship [106, 175]:

$$\frac{T_i}{T_f} = \left(\frac{V_f}{V_i}\right)^{1/\xi} \tag{4.1}$$

with $\xi = 3/2$ for the three-dimensional geometry that we have. From the simulations of the trapping potential we estimate that the trap volume increases by a factor of $\sim$13 during the transfer. This results in a ratio between the initial and final temperature for perfect adiabatic conditions of $\sim$2.5. The temperature could therefore be reduced due to adiabatic cooling from the initial maximum 25 mK (due to limited decelerator acceptance) to 4.5 mK.

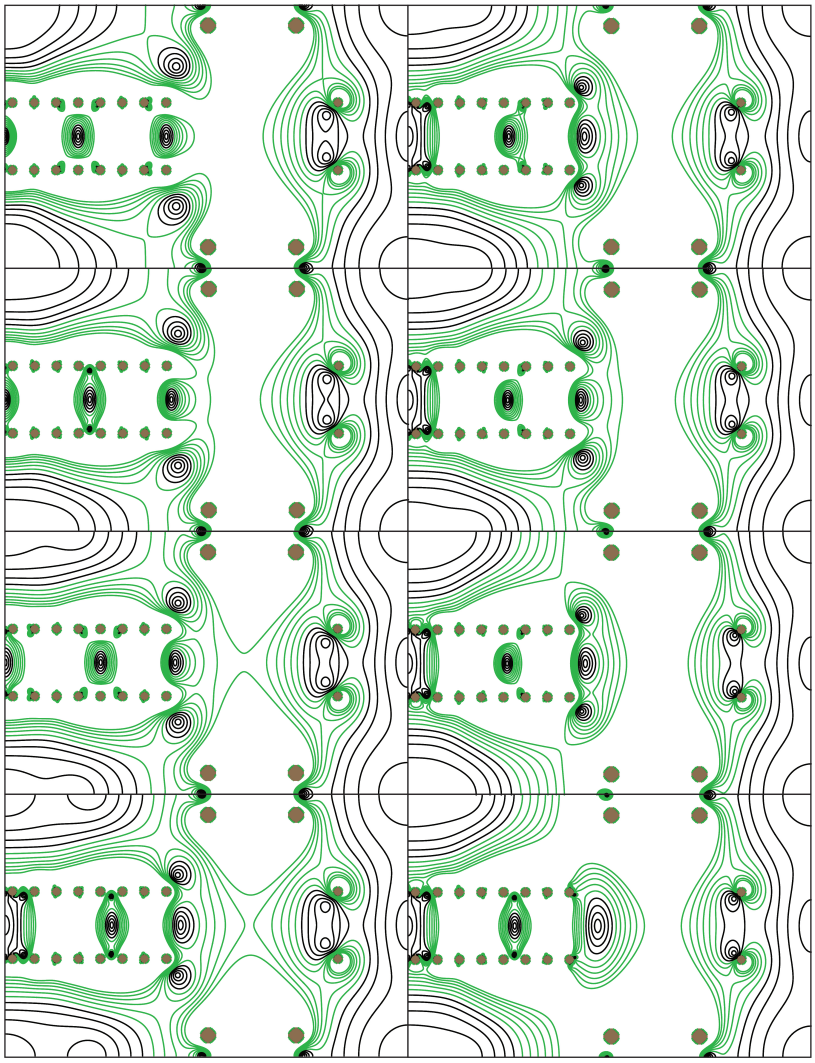

Figure 4.7: *The first eight snapshots of the electric field transporting molecules from the end of the decelerator to the middle of the end trap. The black lines show the contours of the electric field with a deceleration of 9 km/s^2, with a field of 100, 200, 300 and 400 V/mm. The green fields are higher, up to 1 kV/mm. Higher fields are not shown. The sequence is from left top to bottom then right top to bottom.*

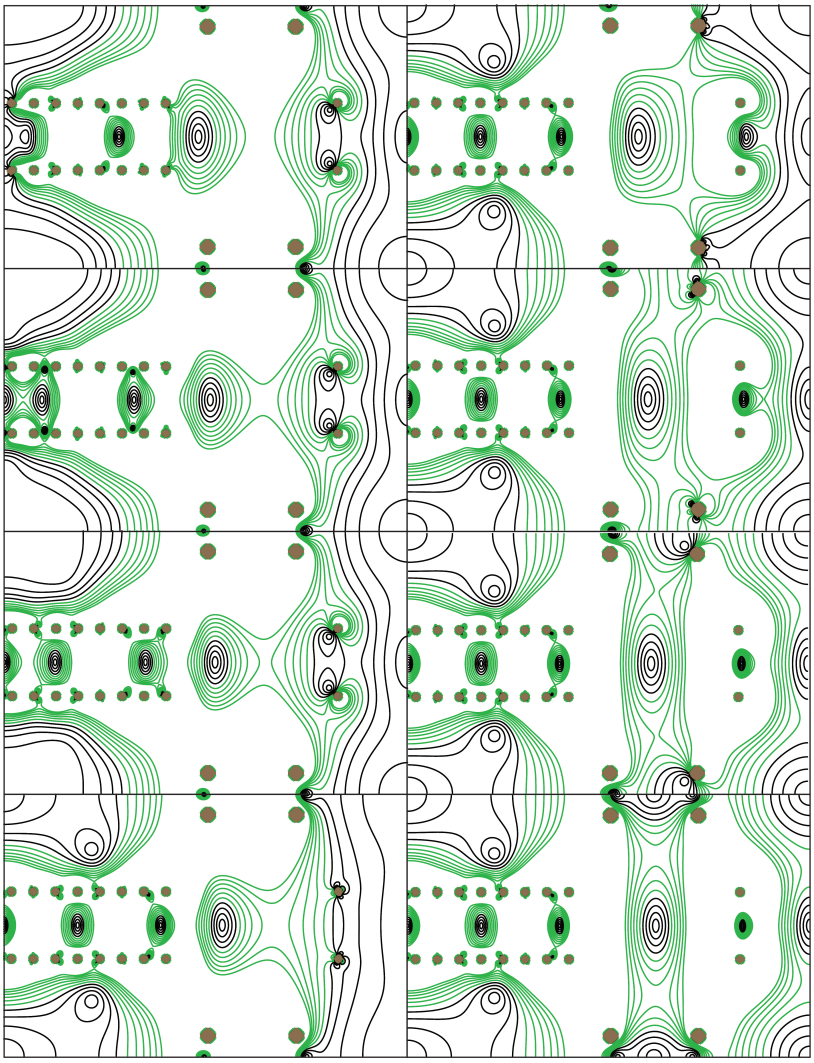

Figure 4.8: *The last eight snapshots of the electric field transporting molecules from the end of the decelerator to the middle of the end trap. The sequence is from left top to bottom then right top to bottom.*

4.3.1 Trap design

The mechanical design of the trap is made by Imko Smid, the parts are made by the mechanical workshop at the KVI-CART. Pictures of the designs

are shown for 2D laser cooling in Figure 4.9 and for 3D laser cooling in Figure 4.10. It consists of a vertically mounted insulating base plate, onto which horizontal supports for the mirror mounts can be attached. The ring-shaped electrodes are mounted on ceramic rods to the baseplate. This baseplate can be directly mounted to the last decelerator module, ensuring good alignment of the electrodes of the extension to the last electrodes of the decelerator. There is the flexibility to use a 2D or 3D laser beam arrangement by replacing two of these supports. The collection of the laser-induced fluorescence is now placed on the molecular beam axis, in order to provide space for the cooling lasers beams, which are also being used for detection of the molecules. Laser beams enter the vacuum chamber through a fiber port. Ultra stable vacuum compatible Polaris mirror mounts (Thorlabs) are used to align the beams.

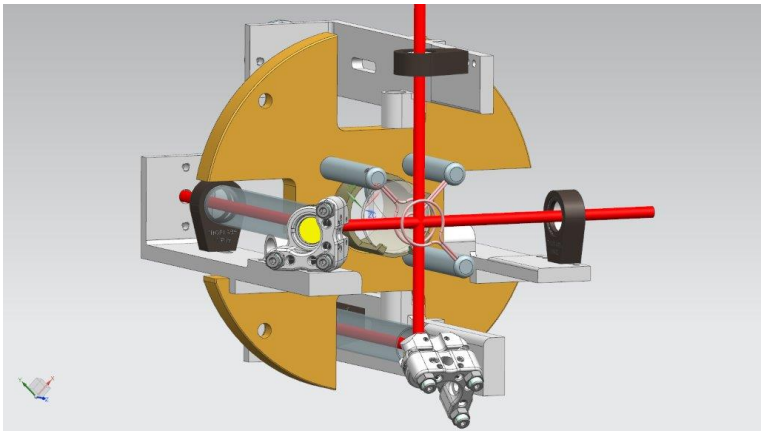

Figure 4.9: *The design of the 2D laser beams through the end trap. The red lines are the laser beams and they cross in the center of the trap. The laser beams are reflected and aligned by ultra stable vacuum compatible Polaris mirror mounts (Thorlabs).*

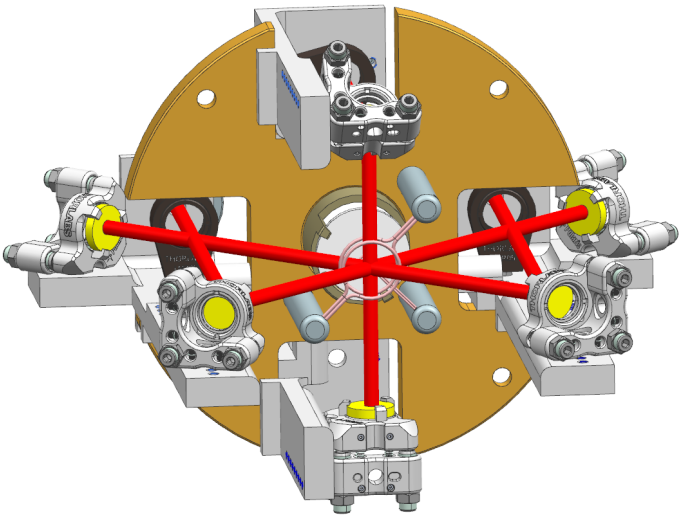

Figure 4.10: *The design of the 3D laser beams through the end trap. The red lines are the laser beams and they cross in the center of the trap. The laser beams are reflected and aligned by ultra stable vacuum compatible Polaris mirror mounts (Thorlabs).*

4.4 Laser system

In this section the laser system is described. Both pump and repump lasers are diode lasers in a home-built laser box. The current, temperature and piezo-voltage are controlled by Moglabs diode laser controllers, type 202. First the pump laser system for the X $^2\Sigma^+(v = 0) \rightarrow A^2\Pi_{1/2}(v' = 0)$ is described, where all the optical elements and the locking scheme are presented, then the repump laser for the $v = 1 \rightarrow v' = 0$ transition. A schematic overview of the pump laser system is given in Figure 4.11.

4.4.1 Pump laser

The pump laser with a wavelength of 663 nm has a HL6545MG-diode with an output power around 60 mW. The mean wavelength of the diode is around 660 nm but this can be adjusted to 15075.68 cm^{-1} (663.32 nm) by the diode current ($\sim$ 120 mA), temperature ($\sim$ 25 °C) and the path length of the diode and the grating. The beam passes a Faraday Isolator

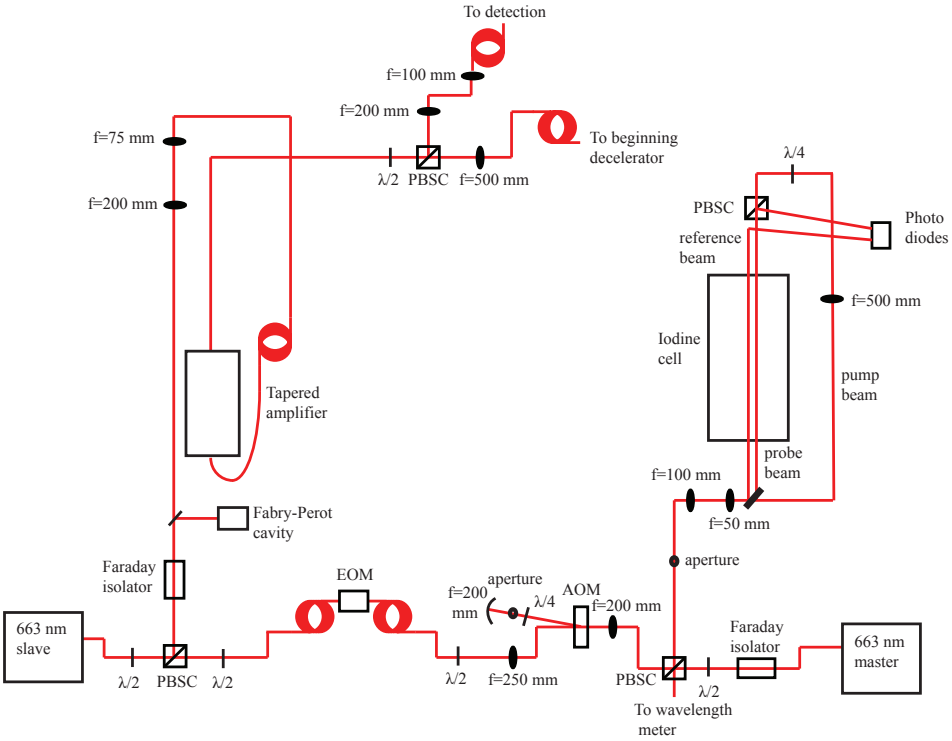

Figure 4.11: *Schematic overview of the pump laser.*

which blocks the light from the opposite direction. Without isolator the reflected light creates instabilities in the diode. The beam passes a polarizing beam splitter cube (PBSC) and an Acousto Optical Modulator, AOM (IntraAction ATM-80A2). The AOM splits the beam into sidebands where the zeroth order goes to the setup. The first order is 72.5 MHz shifted, the difference between the SrF and iodine frequency, and returns via a double pass configuration. This laser beam passes a quarter wave plate (QWP) twice, so the beam is deflected by the PBSC at the return. The beam passes the iodine cell for locking, which is explained below. The zeroth order passes an Electro Optical Modulator, EOM. An EOM is used to make sidebands and, unlike the AOM, the higher orders are not deflected. More about the sidebands of the EOM is given below. After the EOM the beam seeds another laser diode: the slave laser. This laser beam has exactly the same properties as the original beam, only the power is enhanced to 60 mW.

This beam passes another Faraday isolator (Thorlabs IOT-5-670-VLP) and is available for experiments via a fiber. For detection only a few mW is required, for laser cooling the laser power can be enhanced to 500 mW by a tapered amplifier (Toptica BoosTA 00267). The tapered amplifier is also used to gain more power for the hyperfine pumping experiment, which is described in Chapter 5.

Locking to iodine

The pump laser is locked by Doppler-free Saturated Absorption spectroscopy [112] to an absorption line in molecular iodine. After passing the AOM, a beam splitter splits the laser beam ($\sim$ 8 mW) in a reference beam, a probe beam and a strong pump beam. The probe beam passes through a 50 cm-long iodine cell, a PBSC and goes to a photo diode. The iodine cell has a temperature of 300 °C. The pump beam passes the same PBSC from the other side and overlaps with the probe beam in the iodine cell. The reference beam passes through the iodine cell without overlapping the pump and probe beams and is also detected by the photo diode. The two detected signals are subtracted to reduce common noise. To further reduce the noise we modulate the laser diode current and use lock-in detection at 250 kHz. The lock is stable to within 2 – 5 MHz [101]. While scanning the laser frequency, the voltage of the photodiode corresponds to the derivative of the absorption lines of the iodine molecules to the frequency. This signal is shown in Figure 4.12. The laser is locked to the R(115)(6-6)a8 line of iodine at 15075.6811 cm^{-1}.

Electro-Optical Modulator (EOM)

We use a fiber-coupled Integrated Optical Phase Modulator as EOM. A relatively simple way to address all four hyperfine states of SrF is to give a sinusoidal input to the EOM [45]. With a frequency of 41.8 MHz and a modulation index of 2.6, the first and second order have equal laser power. Less power, 17% in total, goes to the other orders. The sidebands in the first and second order do not exactly address all the four hyperfine states: the $|1/2, 0\rangle$-state is 12.5 MHz off if the others are addressed within a few MHz.

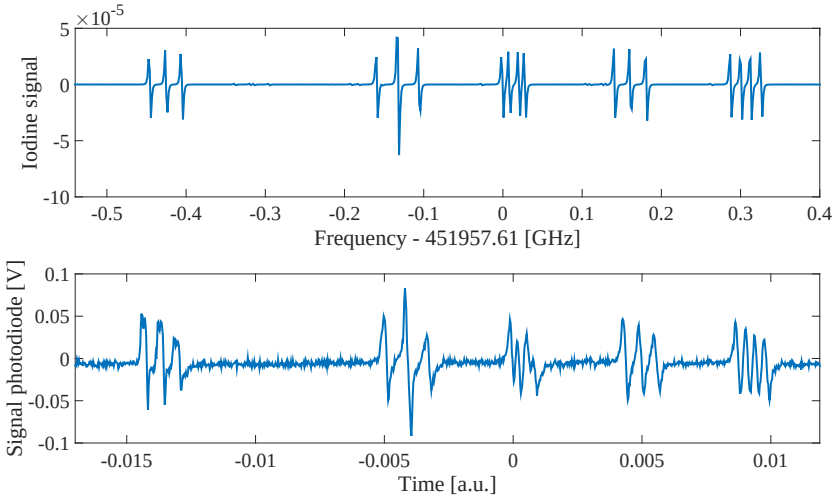

Figure 4.12: *The measured spectrum of absorption from the iodine cell (bottom) compared to simulations of the iodine spectrum in IodineSpec (top).*

The overlap in frequencies can be improved by creating frequency shifts with the serrodyne technique [176]. The electric field for the light through the EOM is $E(t) = E_0 \cos(\omega t + \varphi(t))$, where ω is the optical frequency and φ the phase, imprinted by the modulator. A frequency offset is made by a linear phase variation. The phase ramp should have an amplitude of $2\pi n$ and a period of $1/f_k$ for frequency nf_k, where n is an integer. When the ramp and period do not perfectly match, other frequencies appear. Rogers et al.[177] drove a phase modulator by a sequence of four slopes. We use this technique to produce sidebands that address all hyperfine levels in SrF. The required sequence of triangular waveforms is created using the programmable arbitrary-waveform generator (AOU-H3434-PXIe-12) from Signadyne. It has a bandwidth of 500 megasamples per second, which limits both the maximum frequency shift and the rate at which we can switch between the different sidebands. Another limitation is the Fourier constraint. The linewidth depends inversely on the time spent in the corresponding ramp. Figure 4.13 shows the input of the EOM of four sawteeth, such that the laser frequencies correspond to the four hyperfine transitions of SrF. There was a period of $\sim$250 ns per frequency. The duration of each of the four sets is not the same: for smaller frequency shifts the noise is reduced

so effectively that sideband has more power. To compensate for this, the duration for the two frequencies on the outside have a longer duration (290 ns) while the two in the middle have a shorter duration (220 and 250). The noise of the sidebands depends also on the temperature and can change slightly during the day. Figure 4.14 shows the signal on the Fabry-Perot Cavity applying a sawtooth with two sets of two transition frequencies of SrF compared with the 'normal' sinusoidal input. Figure 4.14 is not normalized, the laser power of the three cases is the same.

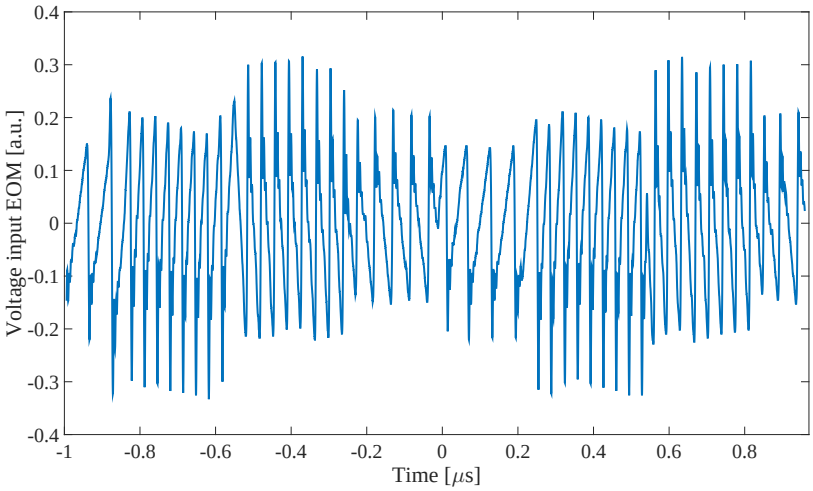

Figure 4.13: *The input voltage of the EOM for the four asymmetric sidebands with a duration per set of* ~ 250 *ns.*

4.4.2 Repump laser

The repump laser has a HL6750MG-diode (685 nm), also with an output power around 60 mW. The typical current is 85 mA, the temperature 20 °C and the path length is chosen so that the wavenumber is 14577.8 cm^{-1}. The beam passes a Faraday Isolator (Thorlabs IOT-5-670-VLP) and by a beam splitter some light is sent to a cavity to lock the beam, as explained in the next section. The rest of the beam (20 mW) is available for the experiment. The power can also be increased by an extra laser diode or a tapered amplifier.

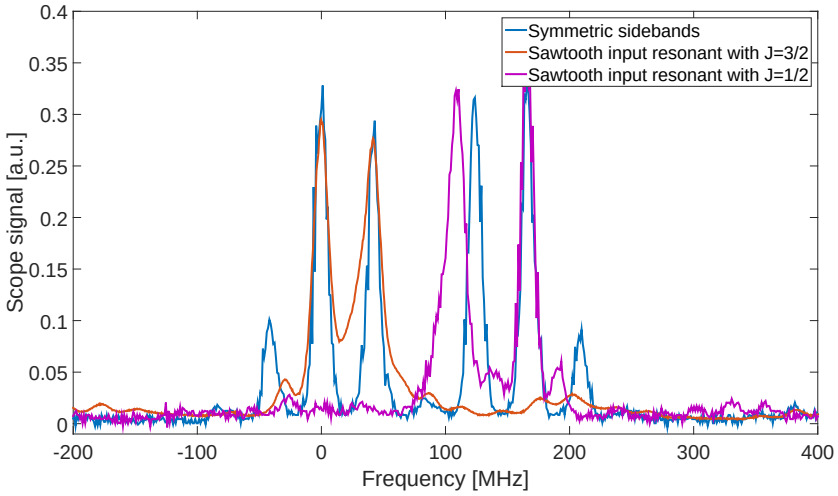

Figure 4.14: *The sidebands created by the EOM applying a sinusoidal input and a sawtooth input. The sinusoidal input has equally spaced sidebands, the sawtooth input makes arbitrary frequencies which can be addressed to the transitions of SrF.*

Cavity locking

The repump laser is locked by a scanning transfer cavity, which has been assembled by J. Nauta [101]. A commercial stable He-Ne laser (<1 MHz/h) and the repump laser are aligned into a Fabry-Perot cavity. The transmission of the resonance peak of the He-Ne laser is used as a reference and the difference between the He-Ne laser and the repump laser is used as a feedback for the repump laser. A schematic picture is shown in Figure 4.15. The stability on short term (< 1 s) has $\sigma = 0.99$ MHz. For long terms the stability is 2.87 MHz/30 min [101]. This can also be used for the lock of the pump laser, or as a reference if the laser is locked.

4.4.3 Detection of molecules

The molecules are detected at the end of the decelerator, in the detection chamber. This is an extension of the last module of the decelerator and is designed to have optimal light induced fluorescence (LIF) for the photon multiplier tube (PMT, Hamamatsu photo sensor module H7422P-40). The molecules fly through the center of a small cube (Thorlabs c4w). From

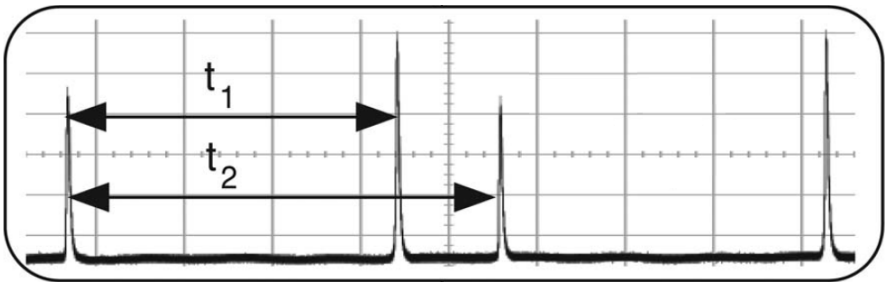

Figure 4.15: *A schematic picture of the resonance peaks of two laser beams in a cavity. The lower peaks are from the reference laser, the higher peaks from the repump laser that has to be locked. The difference $t_2 - t_1$ gives feedback to lock of the repump laser. This picture is from [101].*

one side laser light excites the molecules. The $1/e^2$ beam diameter is 2.4 mm. The laser light is reflected by a mirror to double the power. Excited molecules send their light in random directions. Orthogonal to the laser beam the light is collected via a lens (Thorlabs LA1805) onto the PMT. The lens has a back focal length of 24.2 mm. The cube is adapted to overlap the focal length with the distance between the molecules and the lens. In front of the sensitive area of the PMT a FB660-10 filter (660 $\pm$ 2 nm) is placed. At the opposite side of the molecular cloud the emitted photons go via another lens and a mirror to the PMT. The two lenses capture 1/8th of the total solid angle. A picture is shown in Figure 4.16. Typical background scattering is 6 kHz with a 0.5 mW laser beam and $\sim$100 Hz without laser beam. Because of the highly-diagonal Franck-Condon factors the molecules can be excited a few times before decaying to a dark state. Depending on the velocity the interaction time of the dark states are limiting the number of scatterings per molecules, which is discussed in Chapter 3.

Besides LIF detection, we have used hearing aid microphones to detect the pulsed molecular beam [129]. However this only works for a short decelerator ($<$1 m), as the intensity for longer decelerators quickly becomes too weak to detect.

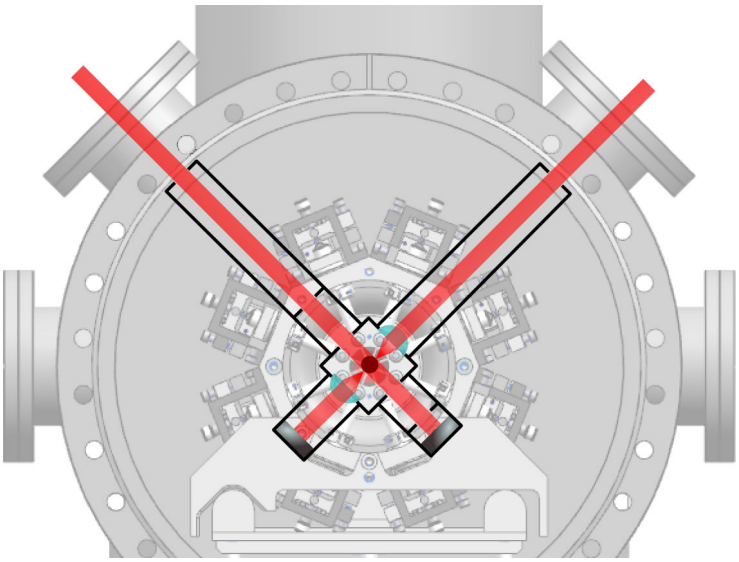

Figure 4.16: *The detection chamber after the last decelerator module. From the upper-left the detection laser enters into the chamber and is reflected from the bottom-right. Molecules scatter photons in random directions. The PMT detects the photons in the upper-right via a strong lens. Photons from the bottom-left are also detected via reflection of the lower-left mirror.*

4.5 Experiments

Besides the experimental setup that is described above, we have an additional source and detection chamber in order to study and improve the expansion and SrF source. We have connected our primary source to this second detection chamber for performing the spectroscopy measurements described below.

4.5.1 Detection of molecules

We have placed the additional source chamber directly after the detection chamber to optimize the source. We have detected the molecules with a brand new SrF_2-pill and quite some laser power (224 mJ per pulse at 1024 nm). The carrier gas was Argon, so the molecular beam obtains a mean velocity of ~ 560 m/s. The detection beam $1/e^2$ diameter is 2.4 mm. Figure 4.17 shows the photon signal. Around $5{\times}10^4$ photons were detected in 100

seconds detection time at a repetition rate of 10 Hz. The detection laser had a power of 0.45 mW, and from simulations we estimate that around 3.5 photons per molecule are detected. The PMT has an efficiency of 1% and the solid angle is 1/8 of the total area. This means that 10^4 SrF molecules per shot are detected.

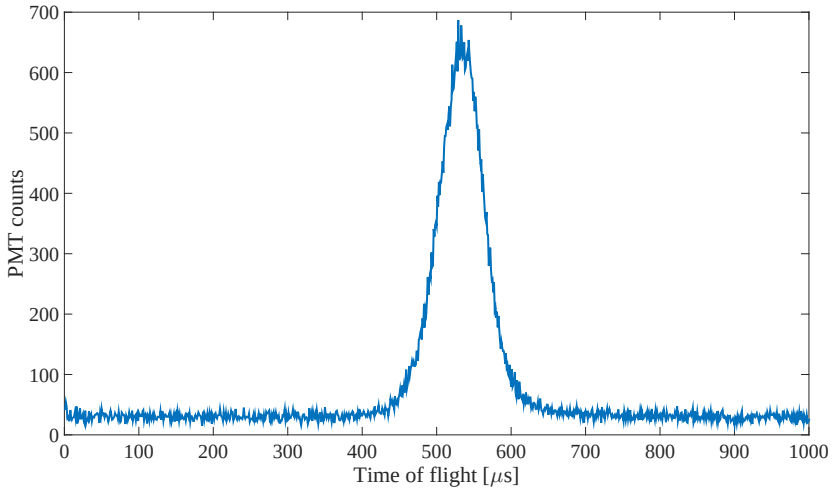

Figure 4.17: *The detection of around $5{\times}10^4$ photons with 0.5 mW laser power and 100 s detection time. With a PMT efficiency of 1%, a solid angle of 1/8 and 3.5 photons per molecule, 10^4 molecules per pulse are detected directly after the source chamber.*

4.5.2 SrF spectroscopy of the $v = 0, N = 1 \rightarrow v' = 0, J' = 1/2$ transition

We have done spectroscopy of SrF directly after the additional source chamber. For the spectroscopy of the $A^2\Pi_{1/2} \rightarrow X^2\Sigma^+$, $v' = 0, J' = 1/2 \rightarrow v = 0, N = 1$ transition the laser frequency is scanned $\sim$ 400 MHz across 20 relatively strong iodine lines. The laser is modulated to see the iodine signal as a reference, see Figure 4.18. At 0.1 mW detection power the four hyperfine states are resolved. Normally for the detection the laser is locked to the R(115)(6-6)a8 line, which is marked by the arrow. The laser frequency is not exactly linear with the piezo voltage so several iodine lines are used to interpolate. Therefore the error bars of the four frequencies are

relatively high and could be improved using the transfer cavity to have the laser frequency as a reference instead of the piezo voltage. Then the current modulation of the laser can be switched off, which affects the linewidth of the laser. From a Gaussian fit the four frequencies are -90 ± 6 MHz, -53 ± 6 MHz, +27 ± 3 MHz and +76 ± 7 MHz away from the iodine line where normally the laser is locked to. From theory the hyperfine splittings are 41, 75 and 55 MHz.

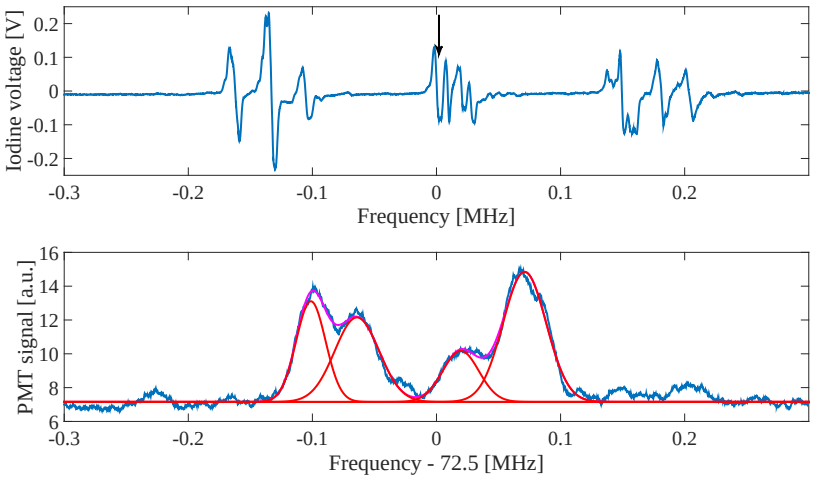

Figure 4.18: *Scanning over the laser frequency to see the four hyperfine levels. The arrow points to the iodine line where normally is locked to. The frequency is shifted by the AOM with 72.5 MHz*

The same measurement was done using 0.17 mW laser power. Due to the power broadening at higher powers the hyperfine levels are not resolved anymore. The measurement and simulations are compared and shown in Figure 4.19. There was no magnetic field, besides the earth magnetic field. In the model the twelve magnetic hyperfine substates are equally populated. The width and the shape of the four peaks is more or less similar. In the simulations the peaks do not have a Lorentzian shape but do exist of more than one peak. Without magnetic field, only the population of molecules in the same m_F state are connected by stimulated emission and absorption. On resonance the transition for one hyperfine state with the excited

state is the most favorable. Slightly off resonance increases the rate for the adjacent transition, while the almost on resonant transition is still very strong. Therefore more photons are scattered. For higher powers the peaks are shifted due to this. For very low powers the shape is Lorentzian. We have simulated also the powers of 0.01 mW, 1 μW and 0.1 μW. The natural linewidth is expected to be $2\pi \times 7$ MHz, which is the case for 0.1 μW.

4.5.3 Detection at the end of the decelerator

The previous experiments were done when the source chamber was directly connected to the detection chamber. Only low-field seeking states make it through to the end of the decelerator. To see this effect at the end of the decelerator we detect the molecules with the four sinusoidal sidebands and compare that to a measurement with the sawtooth-frequencies resonant to the $J = 3/2$ and $J = 1/2$ state. The detection power is 0.5 mW. When the laser frequencies are only resonant with the $J = 1/2$ state, the PMT signal is decreased by 16 $\pm$7% compared to the four sidebands. When the frequencies are only resonant with the $J = 3/2$ state, the PMT signal is 65 $\pm$10% of the signal with four sidebands. A picture is shown in Figure 4.20.

Simulations of this measurement were done. When 5% of the laser power is assumed to go to the frequencies resonant with the 'unwanted' transition, the ratio compared to the four sidebands were 20 $\pm$ 5% and 72 $\pm$ 7%. The simulations and measurements do agree within the error bars, when the frequency is shifted $\pm$ 2 MHz, which is the case when the laser is locked. Figure 4.20 shows the detected molecules at the end of the decelerator and the ratio of detected molecules compared to the four sinusoidal sidebands. At the right y-axis the total number of scattered photons from the simulations is shown. The detected molecules with the frequencies resonant to the transition between the $J = 1/2$ and the excited state is due to the 5% laser power in the frequencies resonant to the transition between $J = 3/2$ and the excited state.

4.5.4 Comparing DC-guiding with AC-guiding

In section 4.2 the working of the decelerator is discussed. Figure 4.21 shows a time of flight plot of AC and DC-guiding. Even thought the photon counts

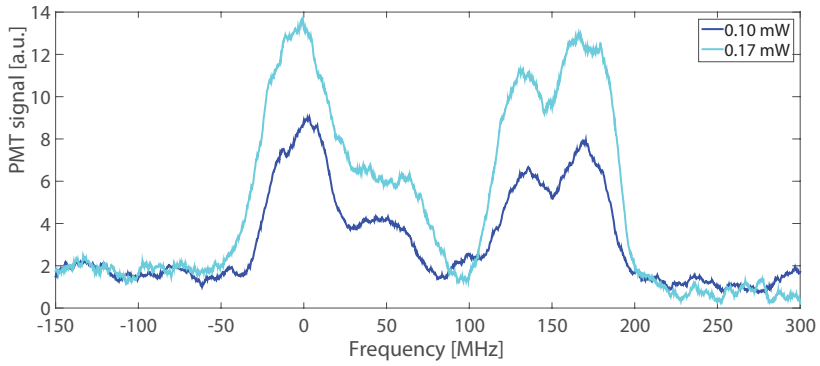

(a)

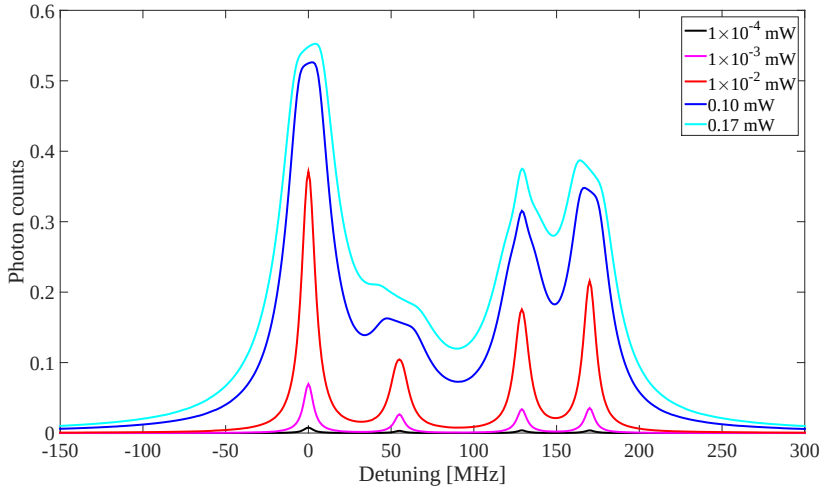

(b)

Figure 4.19: *The upper part shows the spectrum of the four transition frequencies of the $N = 1$ state for 0.10 and 0.17 mW laser power. The backgrounds are subtracted. The lower part shows simulations of the scanning over the four transition frequencies of the $N = 1$-state for several laser powers.*

cannot be compared to each other, the figure shows the difference in velocity spread in both guiding modes.

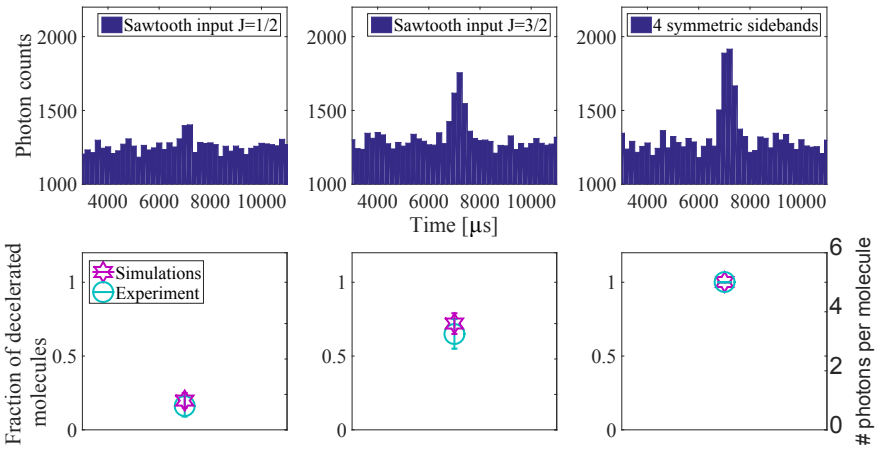

Figure 4.20: *The upper part shows the detection of molecules at the end of the 4 m long decelerator. The molecules are excited by the four symmetric sidebands or by the two sidebands resonant to the excited state and the transition between the high-field seeking states ($J = 1/2$) or low-field seeking states ($J = 3/2$). The lower part shows the fraction of molecules that is detected compared to the symmetric sidebands (experiments) and the number of photon scatterings (simulations) of the three situations.*

4.5.5 Deceleration of the molecules

We have decelerated molecules with a 2 m long decelerator and a cooled valve. Molecules enter the decelerator with 300 m/s and are decelerated to several end velocities. This is shown in Figure 4.22. More about the deceleration can be found in [57] and the PhD thesis of J.E. van den Berg [44].

4.6 Summary

In this chapter the traveling-wave Stark decelerator is discussed. The end trap, an extension of the decelerator with optical access for laser cooling, is designed. The laser setup is shown and discussed. We made use of the serrodyne technique [176, 177]. With this technique a sawtooth signal is given to the EOM input to make arbitrary time-sequenced line spectra. The

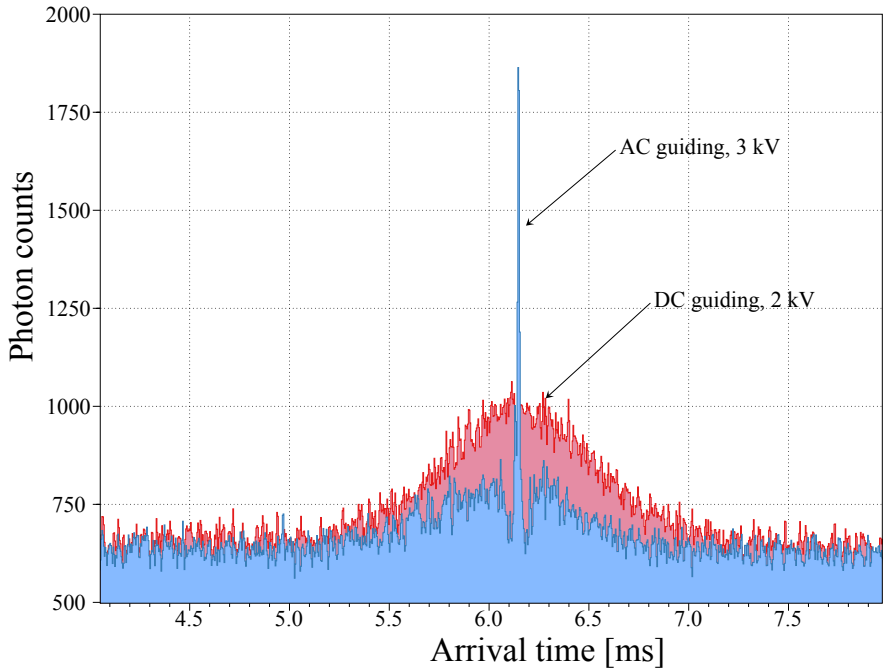

Figure 4.21: *A time of flight plot for AC-guiding and DC-guiding when the decelerator was 2 m. This figure only shows the different shapes in times of flight. The number of detected molecules cannot be compared with each other.*

laser frequencies can address the four hyperfine transition frequencies of SrF. In the experimental results the detection of molecules and the deceleration of molecules are discussed. The source chamber is connected to the decelerator chamber to optimize the number of molecules and to do spectroscopy. The source chamber is also connected to the decelerator chamber. Molecules are decelerated and AC and DC guiding are compared. Also the detection with the symmetric sidebands for the detection laser are compared with the asymmetric sidebands, made by the serrodyne technique.

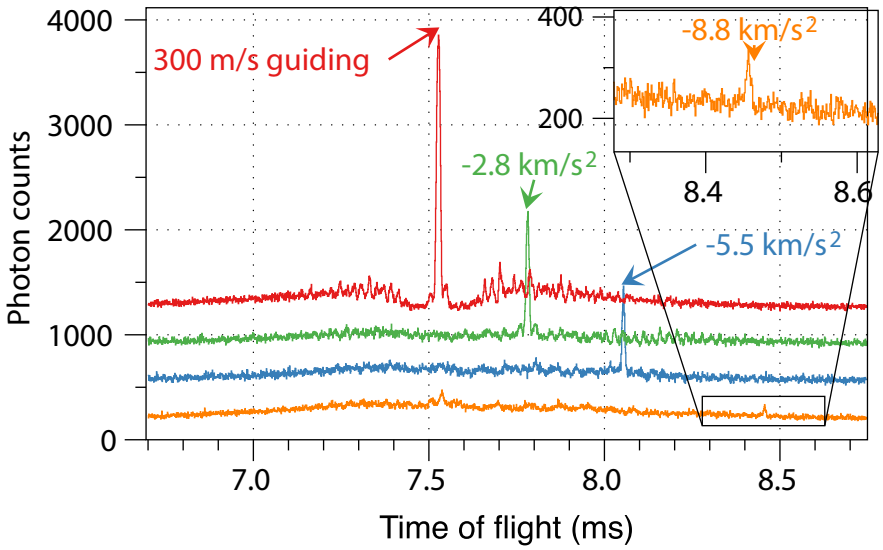

Figure 4.22: *The time of flight spectrum for various decelerations from 300 m/s with a 2 m long decelerator.*

5 | Optical pumping of molecules to low-field seeking states

The traveling-wave Stark decelerator works for molecules in low-field seeking states. Molecules in these states are attracted to a minimum of the electric field strength. For the detection, and in the future for laser cooling, the $v = 0, N = 1$ level is used. This is the lowest rovibrational level with low-field seeking states. The rotational $N = 1$ level is split into a $J = 3/2$ and $J = 1/2$ level due to spin-rotation coupling. Each of those is split into two hyperfine components. This results in 12 m_F states. Only four of these are low-field seeking and eight are high-field seeking states. Figure 5.1 shows the low-field seeking states (green) and high-field seeking states (black). It also shows the high-field seeking states which are dark for excitation to the $A^2\Pi_{1/2}, J = 1/2$ state with linearly polarized light (red). A picture of the Stark shift is also shown in Figure 5.1. The Stark shifts were calculated by the program PGopher.

If the molecules from the source are equally distributed over the twelve hyperfine states, only 1/3 will arrive at the end of the decelerator. When all molecules in the $J = 1/2$ state are optically pumped into the $J = 3/2$ state, at most 1/2 of the population is in the low-field seeking state. Thus, we expect to increase the number of molecules at the end of the decelerator by a factor 1.5. We could also pump molecules only into the $F = 2$ state. The hyperfine splitting between this state and the $F = 1$ is 41 MHz. Power broadening becomes more important than for the splitting between $J = 3/2, F = 1$ and $J = 1/2, F = 0$. Here the energy spacing is 74 MHz.

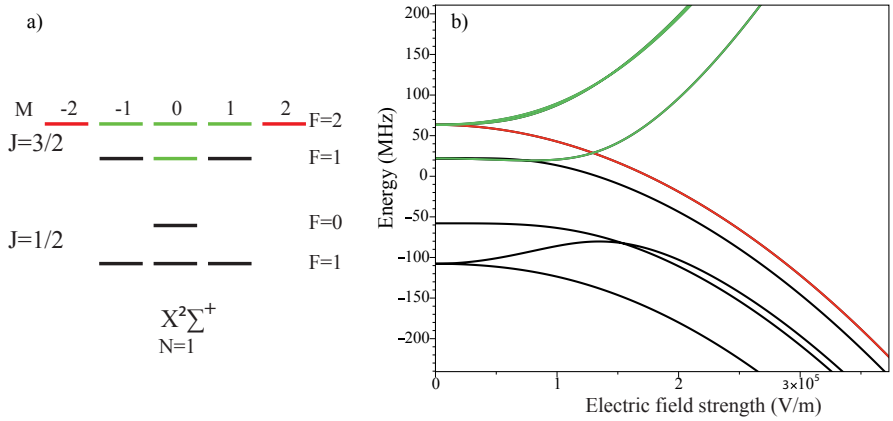

Figure 5.1: *a) The magnetic substructure of the $N = 1$ rotational state. b) The $N = 1$ rotational state in a magnetic field. The green states are low-field seekers, the red states are the dark states when linearly polarized laser light is applied, resonant with the $A^2\Pi_{1/2}, J = 1/2$ state. These red states are, together with the black states, high-field seeking.*

In this chapter we study, both experimentally and through simulations, the possibility to increase the fraction of low-field seeking molecules by optical pumping. A transverse laser beam interacts with molecules at the entrance of the decelerator. The laser beam contains light at frequencies that are resonant with the transitions from the high-field seeking $|J = 1/2\rangle$ states to the excited $A^2\Pi(J = 1/2)$ state. A fraction of the molecules in the excited state spontaneously decays to the low-field seeking states, which are not resonant with the laser light. On the contrary, when the molecules in the $|J = 3/2\rangle$ state are excited, this causes a loss in the fraction of low-field seeking molecules by decay to the $|J = 1/2\rangle$ manifold. We have investigated this optical pumping process through experiments and numerical simulations. The results are presented in this chapter.

5.1 Experiment

A schematic overview of the experiment is shown in Figure 5.2. The experiment has been done with DC-guided molecules ($\pm$ 1.25 kV) in a 4 meter long decelerator. The molecules were expanded in Ar and had a velocity

of 560 ± 60 m/s after the supersonic expansion. A laser beam, the pump laser, crossed the molecular beam 12 cm downstream from the entrance of the decelerator. This is the first optical access of the vacuum chamber. The transverse oscillation frequency of the molecules in the decelerator is ∼ 350 Hz, corresponding at this velocity to a distance of ∼ 1.5 m. In the first 12 cm of the decelerator we, therefore, do not yet have a spatial separation of the low- and high-field seeking states. The guiding electric fields were switched off for 200 μs when the molecules crossed the laser beam so that there was no Stark shift. Two sets of measurements were done: one with a circular laser beam profile and one with an elliptical laser beam profile, where one aspherical lens was used. The power distribution of the laser beam was Gaussian with a $1/e^2$ of 2.4 mm. The elliptical laser beam was spread out along the ring structure by a factor 17.5. We did the experiments before the simulations where done and we wanted to be sure that the interaction time of the laser light with the molecules was long enough. The total laser power in the beam was measured before entering the decelerator.

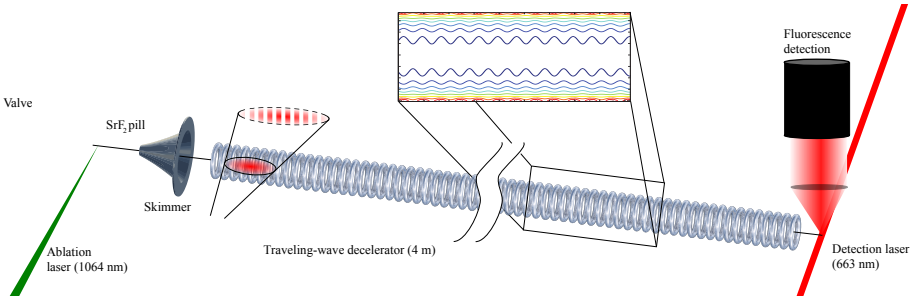

Figure 5.2: *A schematic overview of the hyperfine pumping experiment, showing the elliptical beam configuration.*

The two laser frequencies were made by the serrodyne technique using a phase modulator driven by a sawtooth voltage [177]. The frequencies were made by optimization of the fringes of the Fabry-Perot cavity such that most of the power went to the frequencies that excite the $J = 1/2$ or $J = 3/2$ state. A more detailed explanation is available in Chapter 4. Figure 5.3 shows the fringes of the Fabry-Perot cavity for a sinusoidal input and for the two frequencies created by the sawtooth input. The total laser power is the same in all three cases.

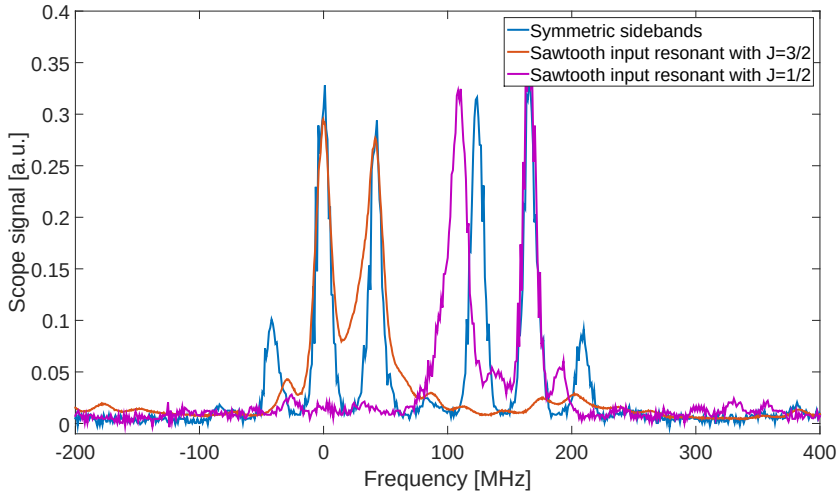

Figure 5.3: *The fringes of the Fabry-Perot cavity showing the frequency sidebands when applying a sinusoidal input and a sawtooth input to the EOM. The four symmetric sidebands created using the sine wave are used for the detection at the end of the decelerator. The frequencies made with the sawtooth input are resonant with the transition between the two $J = 3/2$ or the two $J = 1/2$ hyperfine levels and the excited state.*

The molecules are produced and guided with a repetition rate of 10 Hz. At the crossing with the pump laser, molecules in the $J = 1/2$ or in the $J = 3/2$ states are excited. Accordingly, there will be an increase and decrease, respectively, of the molecules in the low-field seeking states. The number of scatterings needed to pump the maximum fraction to the low-field seeking state is 4.8. The number of scatterings realized in the experiment depends on the laser power and the width of the laser beam: with too low power there will be too little interaction for significant optical pumping, with too high power there will be power broadening and all the molecules will end up in the high-field seeking dark states. The maximum available laser power in the pump beam is 20 mW. Every second shot is used as a reference: during these shots the pump beam is blocked by a mechanical shutter. The reference should compensate for long term changes, for example damage of the pill. At the end of the decelerator the molecules are detected by laser

induced fluorescence (LIF). Four sidebands, made by an EOM driven with a sinusoidal waveform addressed all the four hyperfine states. The laser power used for detection is 0.5 mW.

5.1.1 Data analysis

The arrival times of the molecules at the detection zone can be approximated by a Gaussian distribution [44]. The time of flight (ToF) spectra with and without the pump laser beam being present were fitted. From the fit the total number of photons is obtained, N_{on} for the measurement with the pump laser on and N_{off} for the measurement where the pump laser is blocked. The ratio, $r = \frac{N_{\text{on}}}{N_{\text{off}}}$, is the ratio between the number of detected molecules at the end of the decelerator when optical pumping is used, compared to the number of detected molecules without pumping. From the two Gaussian fits, an error is obtained, e_{on} and e_{off}. The error of the ratio is:

$$e_r = r\sqrt{\left(\frac{e_{\text{on}}}{N_{\text{on}}}\right)^2 + (\frac{e_{\text{off}}}{N_{\text{off}}})^2}. \tag{5.1}$$

An example is shown in Figure 5.4.

5.2 Simulations

The optical pumping was simulated by the multi-level rate equation model (MLRE) as described in Section 3.3. The initial population of molecules was assumed to be equally divided over the 12 magnetic hyperfine substates. The simulations compared the population of low-field seeking states after the interaction with light with the initial population of low-field seeking states. The propagation of the molecules through the decelerator in guiding mode was not taken into account in these simulations: it is assumed that all low-field seeking molecules are being transported and detected with unit efficiency while none of the high-field seeking states make it to the detector.

5.2.1 Intensity distribution

The distribution of the laser intensity is derived from a Gaussian distribution. The decelerator rings have a thickness of 0.6 mm and the spacing between the rings is 0.9 mm. In the simulations the intensity is zero at the

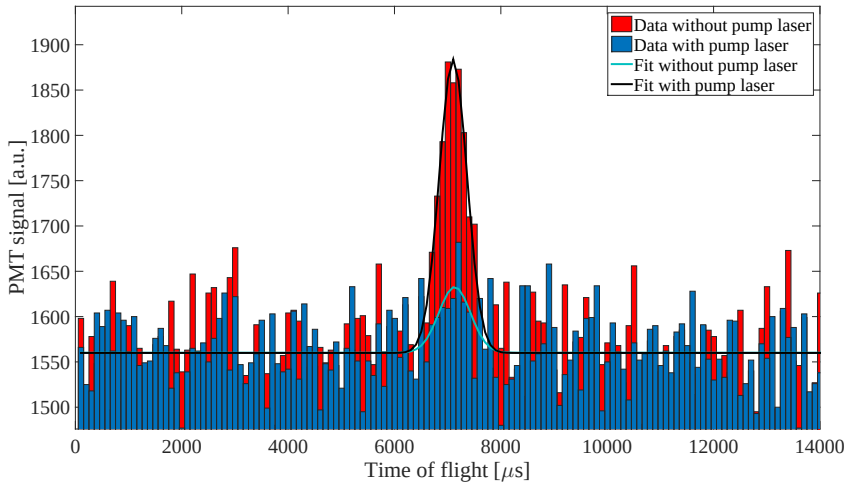

Figure 5.4: *An example of a time of flight spectrum of the molecules when the pump laser is crossing the molecules and when it is blocked. A laser power of 2 mW was used to pump away LFS molecules. The ratio and error are* $r = 0.26$ *and* $e_r = 0.15$.

positions where the rings block the light. Assumed is that the laser beam is perpendicular to the decelerator rings. In the measurements the elliptical beam was a little divergent but negligibly so. A picture of the simulated intensity distribution in the laser beam is shown in Figure 5.5.

5.2.2 Spatial molecular distribution

In the central region of the decelerator the laser power is higher than in the upper and lower parts. The assumption is that the high- and low-field seeking states are both equally distributed transversely inside the decelerator: due to the circular shape of the electrode, there are more molecules on the decelerator axis than in the upper or lower regions. The model does not take into account the effect that high-field seeking states are more attracted to the edges and that low-field seeking states are attracted to the center of the decelerator. The model accounts for the laser power distribution and molecular distribution.

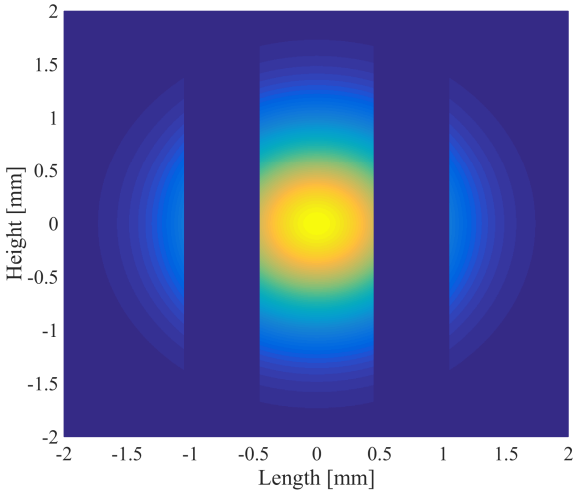

Figure 5.5: *Simulations of the Gaussian intensity distribution of a circular ($\epsilon = 1$) laser beam with $1/e^2$ diameter of 2.4 mm crossing the rings.*

5.3 Results

First the difference between the circular and elliptical beam is simulated. The height of the laser beam, d_0, is kept constant. The ellipticity is $\epsilon = d/d_0$, where d is the horizontal width of the laser beam. With the width and ϵ we denote the laser power distribution along the decelerator axis and the height of the laser beam is in the vertical direction. Measurements were done with $\epsilon = 1$ (circular) and $\epsilon = 17$ (elliptical).

5.3.1 Width of the beam

There are two important parameters for the interaction with light: the interaction time and the laser power or intensity. Doubling the horizontal width of the laser beam also doubles the interaction time. However the laser intensity is halved if the power is kept the same.

Simulations

Simulations were done with the laser frequencies being resonant with the transition between the $J = 1/2$ state and the excited state, so that part of

the high-field seeking states are pumped into the low-field seeking states. This is done for various laser powers and ellipticiy ϵ. Figure 5.6 shows the increase in the fraction of low-field seeking molecules normalized to the situation with no laser light. When the interaction of light with molecules is long enough ($\epsilon > 2$), the results become independent on the width of the laser beam. At small ϵ the interaction zone is short and the pumping is limited by the decay time. The same is done with laser frequencies resonant to the transition between $J = 3/2$ and the excited state. Now the low-field seeking molecules can only be pumped into high-field seeking states. Figure 5.7 shows the ratio of LFS population when frequencies are resonant with the transition between the $J = 1/2$ state and the excited state. The simulations were performed for powers up to 40 mW. The maximum gain in LFS population is found to be around 25 mW, depending on ϵ. At higher powers the increase in LFS population is reduced due to power broadening. The center of the laser beam is chosen to be in the middle of two ring electrodes. At very small widths all the laser power passes in between decelerator rings. For larger widths, around $\epsilon \sim 0.3$, the electrodes partially block the light. At higher ϵ ($\epsilon > 2$) the total power is effectively lowered by 2/5, the ratio between the spacing between the electrodes (0.9 mm) and the thickness of the electrodes (0.6 mm). A combination between the relatively weak transition of the excited state and $J = 3/2, F = 1$ and power broadening that plays a role for the transition between the excited state and $J = 3/2, F = 2$ causes a lower gain around $\epsilon = 0.5$ in Figure 5.6.

Measurements

The measurements with the circular beam are plotted in Figure 5.8 and for the elliptical beam in Figure 5.9. In the measurements the number of detected photons with the pump laser on is compared to the number of photons without laser.
In both measurements the molecules in the low-field seeking states could be pumped away. Increasing the power beyond $\sim$ 2 mW does not lead to more losses. When pumping molecules from the high-field seeking states into the low-field seeking states, there is no clear gain or loss. The expected fraction of 1.5$\times$ the low-field seeking population compared without pump laser is not seen in the experimental data. In the next paragraphs we discuss the change of some parameters in the simulations to see how sensitive the

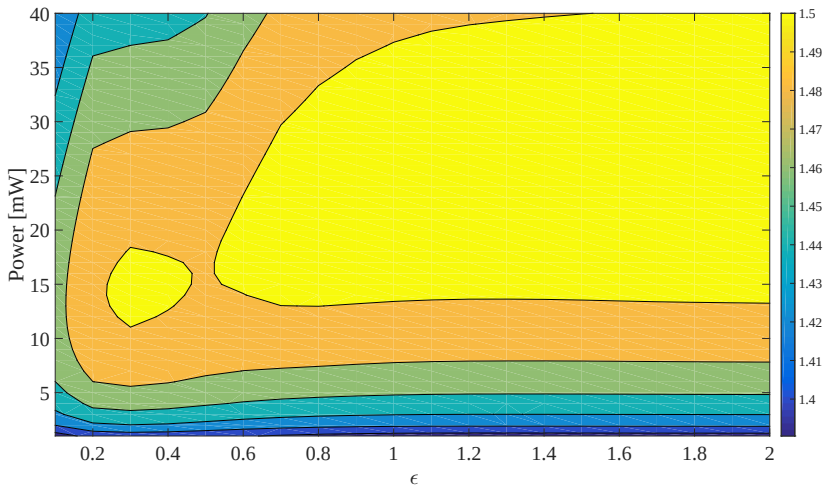

Figure 5.6: *Simulations of the increase of low-field seeking molecules as function of the width of the laser beam and the total power. This is with the laser frequencies being resonant with the transition between the $J = 1/2$ state and the excited state. The results are normalized to the case without pump laser.*

hyperfine pumping is to those. The parameters of the measurements that can be different than simulated are: the position of the laser beam, the diameter of the laser beam, the initial population of the molecules, the detuning of the laser light and the power distribution over the frequencies.

5.3.2 Horizontal position of the laser beam

The laser beam crosses the decelerator rings. Dependent on the horizontal position the power distribution might change. In the simulations the position of the laser beam with respect to the decelerator rings is changed to several positions. This does not affect the gain or loss in low-field seeking states within the uncertainties.

5.3.3 Vertical position of the laser beam

The horizontal and vertical position of the laser beam is aligned by eye. An image of the crossed laser beam is visible where it exits the decelerator. The decelerator rings and the outer edges were clearly visible in the image.

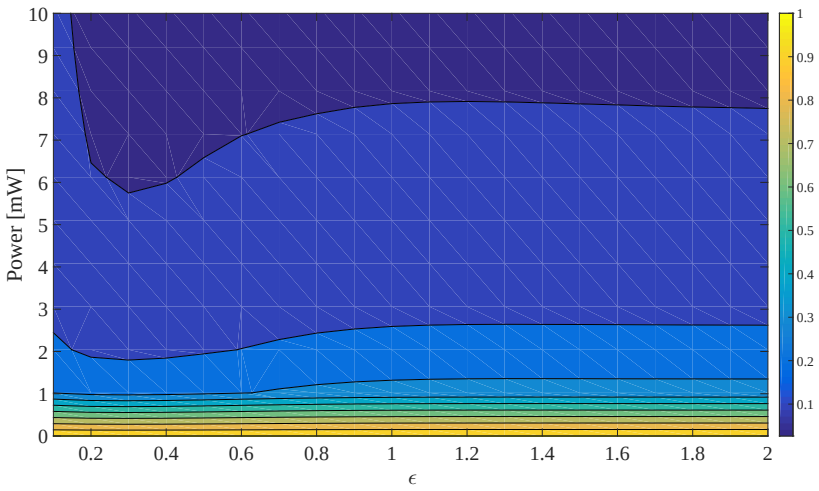

Figure 5.7: *Simulations of the decrease of low-field seeking molecules as function of the width of the laser beam and the total power. The laser frequencies are resonant with the transition between the $J = 3/2$ state and the excited state. The results are normalized to the case without pump laser.*

The laser beam is aligned to the center and would be maximally 0.5 mm off. When the vertical position of the laser beam is not exactly in the center of the rings, there is effectively less laser power for a larger part of the molecules. Figure 5.10 shows the dependence of optical pumping for several heights of the laser beam. The alignment of the elliptical and circular laser beams were performed independently. This might be the reason why only the elliptical beam has effectively less power.

5.3.4 Detuning of the laser frequency

The laser is locked to an iodine line and is stable within ~ 5 MHz. When the laser is locked to the wrong iodine line the offset to the next peak is 9 MHz. Figure 5.11 shows the dependence on the detuning of the laser frequencies. This might be a reason why the interaction with laser light in the experiments was less effective than we simulated in 5.3.1.

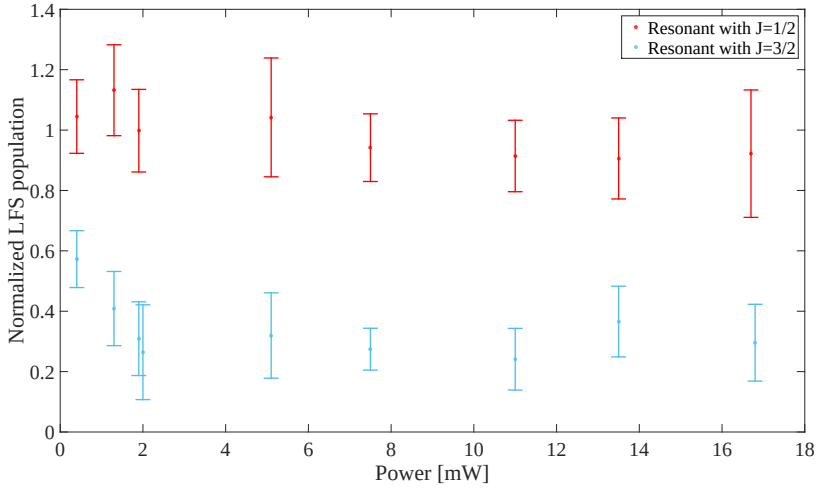

Figure 5.8: *Measurements of the hyperfine pumping using the circular laser beam ($\epsilon = 1$). The normalized LFS population is the ratio of detected molecules at the end of the decelerator compared to the case without laser. The error bars originate from the statistical uncertainty in the number of detected molecules.*

5.3.5 Power distribution over the laser frequencies

The serrodyne modulation technique introduced unwanted frequencies in the laser light, due to the imperfectness of the sawtooth. More about the serrodyne technique is described in Chapter 4. Figure 5.12 shows the dependence on the distribution of the laser power over the four frequencies.

When we use the serrodyne technique to address the LFS states, around 5% of the power ends up in the unwanted frequencies that are resonant with the HFS states. The same is true for the opposite case. Other frequencies than the four transition frequencies are neglected in the simulations. According to the simulations, 5% of power leaking already influences the number of low-field seeking states, especially at higher powers.

5.3.6 Diameter of the laser beam

The width of the laser beam was obtained by measuring the laser power when an aperture is varied in diameter. The diameter is accurate within

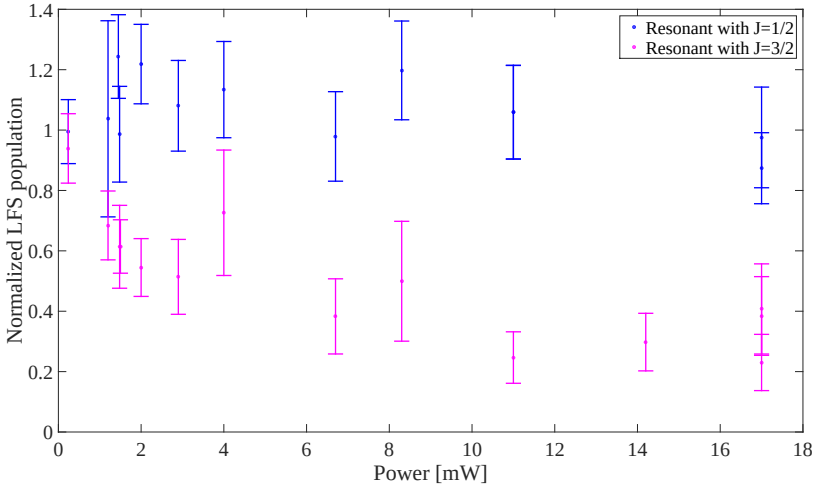

Figure 5.9: *Measurements of the hyperfine pumping using the elliptical laser beam ($\epsilon = 17$). The normalized LFS population is the ratio of detected molecules at the end of the decelerator compared to the case without laser. The error bars originate from the statistical uncertainty in the number of detected molecules.*

0.1 mm. In Figure 5.13 the dependence of the hyperfine pumping on the diameter is shown. This might also be a parameter which causes the difference between the simulations and the measurement. Only at higher powers the ratio of LFS states does not depend much on the diameter.

5.3.7 Initial population of the molecules

It is assumed that the high and low-field seeking states are equally populated at 12 cm from the entrance of the decelerator. In the measurements it looks like there is no increase in low-field seeking molecules, because there are perhaps no high-field seeking molecules to be excited. A reason for this is that they are deflected by the electric fields before they reach the interaction zone. Simulations were done where all high-field seeking molecules are already gone and where 25% and 50% of the high-field seeking molecules are reaching the interaction zone. This is shown in Figure 5.14. The initial population is the only parameter that can explain why the measurements in which we pump the high-field seeking states do not show a significant increase in low-field seeking molecules. When a part of the high-field seeking

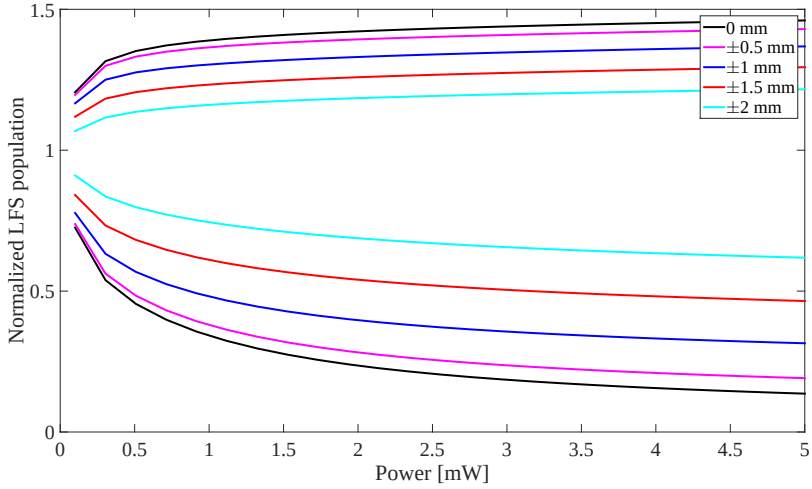

Figure 5.10: *The dependence on the height of the laser beam with respect to the center of the decelerator rings.*

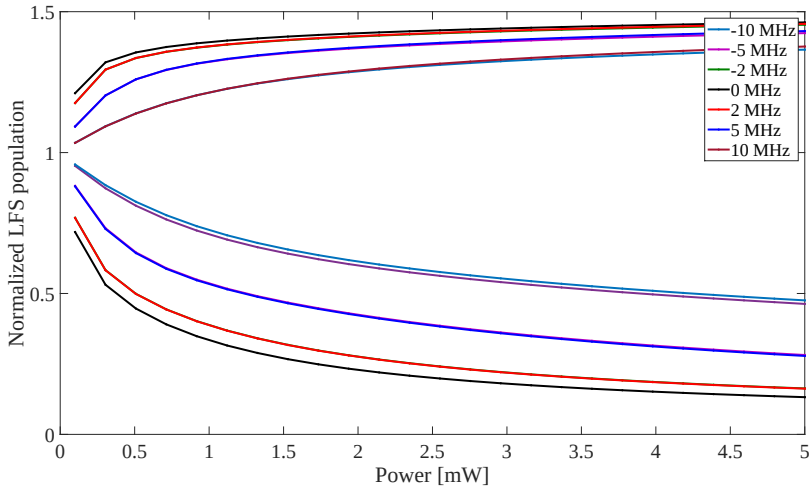

Figure 5.11: *The dependence on the detuning of the laser frequency with respect to the frequency.*

molecules is already deflected due to the electric field, there is a decrease

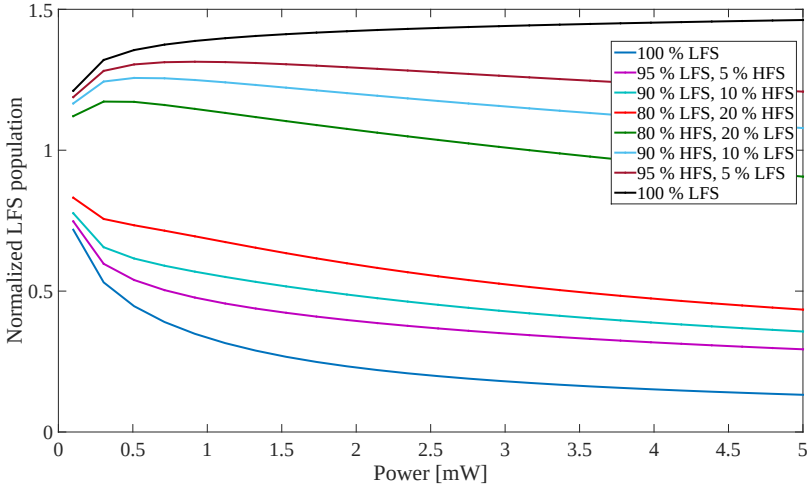

Figure 5.12: *The dependence on the power distribution to the four resonant frequencies.*

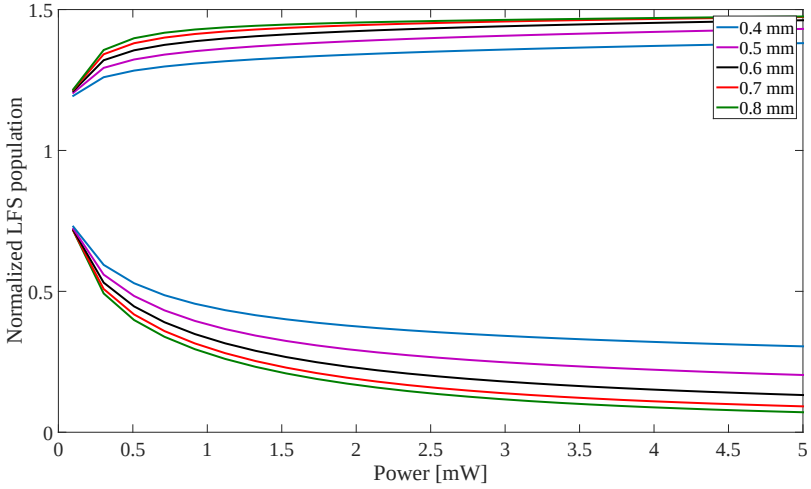

Figure 5.13: *The dependence on the diameter of the laser beam.*

in the possible gain of low-field seeking molecules. Simulations that track molecules in the low- and high-field seeking molecules in the decelerator

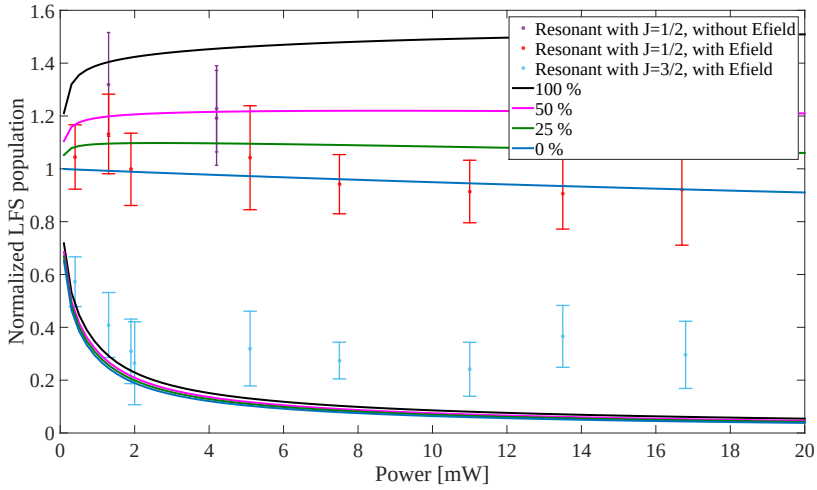

Figure 5.14: *The dependence on the initial distribution of the high-field seeking states and the measured data obtained from the simulations (lines), compared with the measured data (symbols). The purple points are the fractions of molecules in the low-field seeking state when the electric field is switched off before the interaction with the pump laser. The error bars error bars originate from the statistical uncertainty in the number of detected molecules.*

show that there is a negligible difference between the two. Two extra measurements were done when the electric field was only switched on after the interaction of the molecules with the laser beam. These are the yellow data points in Figure 5.14. There is a gain in low-field seeking molecules compared to the experiment where the electric fields were only briefly turned off at the interaction point. Without electric field the high-field seeking states can not be deflected from the decelerator axis. The total number of low-field seeking molecules was also decreased, which means that the low-field seeking molecules were also influenced by the absence of electric field during that short period.

5.4 Summary: all parameters

The described parameters influence the hyperfine pumping measurement. By taking realistic parameters of the experiment into account, the simu-

lations and measurements agree within the error bars of the measurement (Figure 5.15). In the model the detuning is set at 2 MHz and the fraction of power to the unwanted laser frequencies is set at 5%. Because the model for the circular beam was more in agreement with the measurements than for the elliptical beam, it suggest that the height of the elliptical beam was 0.5 mm off in the experiment. For the initial population 50% of the molecules in the high-field seeking states were simulated. For the circular beam the population where 100% was left is also simulated and compared with the few data point were the electric field was switched off before the interaction with the pump laser.

5.5 Conclusion and outlook

The goal of this experiment and simulations was to increase the number of low-field seeking molecules by optical pumping of the high-field seeking molecules into low-field seeking molecules. The expected increase of low-field seeking molecules was at most 50% from simple calculations by counting the number of low-field seeking states before and after optical pumping. From simulation a gain in low-field seeking state molecules of 50% was indeed found to be possible. This was assuming ideal conditions: the laser light must not have any detuning from the resonant frequencies and it must not contain light at other frequencies nearby. Furthermore no electric fields should be present so that high-field seeking molecules are available to pump into low-field seeking molecules. In practice not all the parameters in the experiment are ideal: the lock is stable within a few MHz, the sawtooth-input to the EOM is not perfect etc. When we account for this, the simulations and the measurements agree within the error bars, which originate from the statistical uncertainty in the number of detected molecules. The shape (circular or elliptical) of the laser beam does not matter that much, as long as the interaction time is long enough.

The number of low-field seeking molecules can be improved when laser light interacts with the molecules before they enter the decelerator. In our setup this is possible in the source chamber, directly after the molecules are made. The error bar of the experiments can be decreased by using AC-guiding of the molecules. The longitudinal velocity spread will be smaller (from 56 m/s to 5 m/s) so the background is less.

Not included in these measurements and simulations is the magnetic field. After a few optical cycles the molecules can decay to a dark state ($\sim$ 30% for these simulations). With a magnetic field the molecules can be recycled again. Within the decelerator, where high-field seeking states were deflected, this might be a disadvantage because the low-field seeking molecules loose their orientation.

Another option is to use the electric field in the decelerator: the low- and high-field seekers are separated by their Stark shift. There are transition frequencies for only low or high-field seeking states so in theory all high-field seekers can be pumped without pumping low-field seekers. This might be interesting for electric fields higher than 2×10^5 V/m (see Figure 5.1). In the decelerator the electric field is not constant and especially in the center the field is small. For example: for the deceleration of 9 km/s^2 the maximum electric field is around 4×10^5 V/m. It could work if the laser beam only crosses molecules at a high electric field (only the outer region of the decelerator).

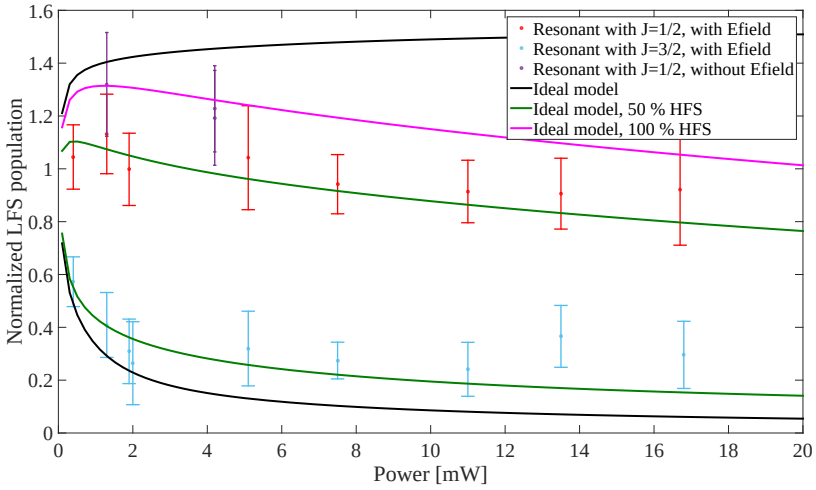

(a)

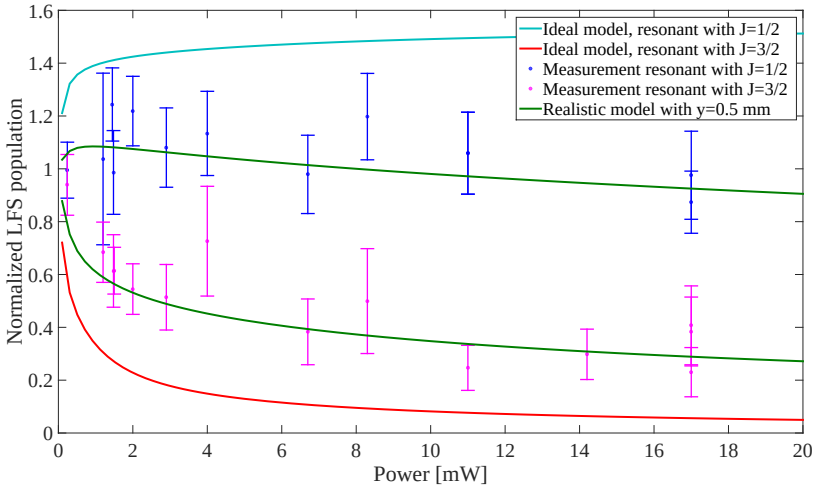

(b)

Figure 5.15: *The measurements and simulations including the detuning and frequency dispersion. The upper plot is for the circular beam and the lower plot is for the elliptical beam. The simulations consider a detuning of 2 MHz, the fraction of power to the unwanted frequencies of 5%, the height is set at 0 mm (circular beam) and 0.5 mm (elliptical beam) and the initial population of molecules in the high-field seeking state is simulated for 50% and 100%.*

6 | Summary & outlook

Molecules are very sensitive probes for testing the Standard Model, due to their rich energy level structure. For a number of precision experiments the sensitivity to new phenomena is greatly enhanced as compared to similar experiments in atoms. However, this level structure is also more complicated and some of the techniques that work well for atoms, e.g. laser cooling, are much more difficult to apply to molecules. Nevertheless in the recent past significant progress has been made. In this thesis an experimental setup is presented that has been designed to test the limits of the Standard Model of particles physics. We can perform such tests in precision measurements. For ultimate precision, excellent control over the molecules is beneficial. In our experiments we combine traveling-wave Stark deceleration with laser cooling of molecules to create a sample of ultracold molecules. We use SrF because this molecule is heavy enough for Standard Model tests and at the same time is light enough to be decelerated in a 5 meter long traveling-wave Stark decelerator. In addition, SrF is laser coolable. The latter feature is the main topic of this thesis.

Molecules are produced in a source chamber, where a tablet of SrF_2 is ablated by intense pulsed Nd:YAG laser light. In this process SrF is formed. By supersonic expansion with xenon gas from a pulsed valve the SrF molecules are cooled into their lower rovibrational states and they expand with ~ 300 m/s into the decelerator device. The traveling-wave Stark decelerator slows a fraction of the molecules down to standstill. The molecular sample has a temperature of 12 mK. Laser cooling can be applied subsequently to cool the sample even further. Figure 6.1 shows on overview of the experiment.

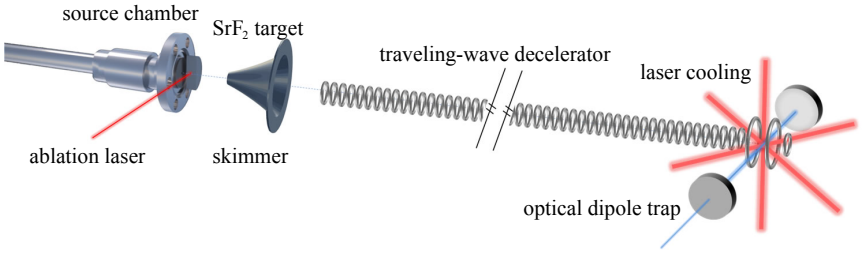

Figure 6.1: *A schematic overview of the setup to decelerate and trap SrF.*

Laser cooling of atoms is being performed since several decades. Molecules are more difficult to laser cool because there are no selection rules for the decay to vibrational states. For some electronic transitions the rotational transitions can be closed or limited due to the parity and selection rules. Nonetheless, some molecules, like the alkaline-earth monohalides are laser coolable. These systems exhibit only a small vibrational leak to higher order states and rotationally the system can be closed such that a limited number of lasers is required to provide the necessary light at all needed wavelengths. For SrF and the other alkaline-earth monohalides the electronic $X^2\Sigma^+ \rightarrow A^2\Pi_{1/2}$ transition is used and the rotational $N = 1, J = 1/2, 3/2 \rightarrow J' = 1/2$ transitions are exploited. Due to our combination with the traveling-wave Stark decelerator, only a few repump lasers are needed for cooling at vibrational states, depending on the number of laser cooling cycles that is required.

There are a number of challenges specific to the laser cooling of molecules. For the laser cooling cycle of SrF there are four hyperfine levels in the excited state and there are 24 ground state sublevels when using only one repump laser. This means that the effective scattering rate is $\frac{2}{7}$ as compared to a two-level system. Also the total angular momentum quantum number being higher in the ground state ($F = 2$) than in the excited state ($F' = 1$) causes dark states. Dark states can become bright by remixing in a magnetic field when linear polarized light is used, or by rapidly switching between two opposite circular polarizations of the laser light. This also makes the scattering force slightly less efficient.

In this work we used the multi-level rate equations (MLRE) to model the interaction of molecules with laser light (Chapter 3). An advantage of combining laser cooling with a traveling-wave Stark decelerator is that the initial velocities for laser cooling is only 2 m/s. We calculate from the MLRE that it will take around 1 ms to cool the molecules for 10 mW per sideband with a $1/e^2$ beam diameter of 40 mm. This will result in the scattering of $\sim 3 \times 10^3$ photons in 1 ms. If we use a main cooling pump laser on the $v = 0$ vibrational state and one additional laser to repump molecules in the $v = 1$ state back into the system, there will be a loss of 7.2% to higher order vibrational states. Here only an optical molasses is employed, there is no magnetic field gradient such as in a magneto-optical trap.

An open electric trap at the end of the decelerator has been designed (Chapter 4) for molecules that are brought to standstill. The setup provides optical access to the cooling laser beams. This is a flexible setup to enable 2D laser cooling, for cold beam experiments, and for 3D laser cooling to trap the molecules. There is also access for an optical dipole trap.

The traveling-wave Stark decelerator decelerates molecules in the low-field seeking states. We detect and apply laser cooling at the lowest rotational state that is low-field seeking, i.e. $N = 1$. This state consist of twelve hyperfine sublevels, only four of which are low-field seeking. The number of molecules in a low-field seeking states can be increased by optical pumping of molecules in high-field seeking states. In Chapter 5 we study both experimentally and through simulations the optimum conditions for this process. The best found option results in a factor 1.5 more low-field seeking molecules.

Outlook

Simulations and measurements performed with a deceleration section of 2 m indicate that the molecules can be stopped within 4.5 m. The ninth and last module of the decelerator has already been assembled. Another option for improvement is to set up a decelerator of 5 m length. The deceleration strength can then be lowered, so the acceptance for the molecules is higher: more molecules will be decelerated to standstill. The extension to give access to the laser beams has also been assembled already and is ready for experiments.

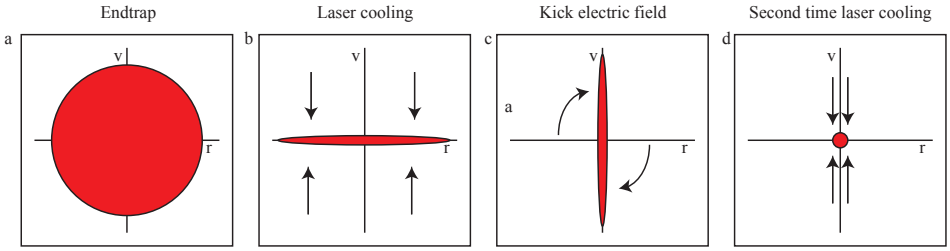

Figure 6.2: *A schematic phase space diagram of the molecules a) after the end trap, b) during laser cooling, c) when the electric trap is turned on again and d) the second time laser cooling.*

Besides the decelerator, we have an extra source and detection chamber to work on improving the number of molecules in the $v = 0, N = 1$ state. The supersonic expansion is now being analyzed in experiments using either a rotating SrF rod or a Sr rod with SF_6 gas mixed in the carrier gas. Investigations in a cryogenic buffer gas cell have been started as well. The second source chamber can also be used for the production and investigation of different molecules that can be decelerated in future experiments.

From laser cooling to an optical dipole trap

In Chapter 3 we performed simulations of laser cooling of SrF molecules at the end of the decelerator. This is achieved by only making use of the optical molasses: the velocity of the molecules decreases and the cooled molecules reach the Doppler limit. The laser cooling force is however independent of position and as a result, the cooled molecules are distributed over a relatively large volume ($\sim 2.6 \times 4.0 \times 4.0$ mm^3). To trap the molecules in an optical dipole trap the spatial size of the cloud needs to be much smaller (~ 500 μm $\times$ 2 mm). One option for trapping as many molecules as possible, is to turn on the electric trap again, so that all low-field seeking molecules are attracted to the trap center. If the trap is harmonic, at one point in time the molecules are all relatively close together. This process is shown in Figure 6.2. When laser cooling is applied again at the right moment, the velocity can be reduced while the molecules have a narrow spatial distribution.

A slow, intense and ultracold molecular beam for precision measurements

In this thesis we reported on an experiment aiming to combine the benefits of laser cooling with the strong points of Stark deceleration. In this way we can come to a total control over both external and internal degrees of freedom of the molecules. The decelerator efficiently reduces the lab-frame velocity such that a limited stage of laser cooling is sufficient to bring the molecules to ultracold temperatures, below 1 mK.

Recently, cryogenic molecular beam sources have created beams with a lower velocity and a higher intensity compared to the supersonic beams we have used in this work. These sources produce very long pulses of molecules, however, and therefore these beams are typically not very well matched to a single potential minimum in the traveling-wave decelerator. For the further cooling and trapping in an dipole trap such a source seems therefore of limited use.

We have realized however through this research that the combination of a cryogenic source, a traveling-wave decelerator and a stage of transverse laser cooling will result in a molecular beam with unprecedented properties: it will be slow, very intense, and transversely very cold. Such a low-divergence beam of stable molecules opens up the way to experiments with a greatly increased coherent interaction time, without sacrificing the number of molecules. If applied in this direction, the techniques and concepts that have been studied and developed in this thesis will be at the basis of a next generation of precision experiments for testing the Standard Model.

7 | Nederlandse samenvatting

Door hun rijke energieniveaustructuur hebben moleculen ten opzichte van atomen voor een aantal fenomenen een sterk vergrote gevoeligheid. Dit maakt moleculaire systemen uitermate geschikt voor onder andere het meten van de mogelijk asferische ladingsverdeling van het elektron, het bestuderen van eventuele tijdsvariatie van de natuurconstanten en ook voor het bestuderen van pariteitsschending in de zwakke wisselwerking. Het meten aan deze fenomenen kan gebruikt worden om de validiteit van het Standaardmodel van de deeltjesfysica te testen.

Een keerzijde van de rijke structuur is dat de grote hoeveelheid toestanden ervoor zorgt dat bepaalde technieken die erg goed werken voor atomen, gecompliceerder zijn voor moleculen. Een voorbeeld hiervan is laserkoelen. Toch is er de afgelopen jaren vooruitgang geboekt in het manipuleren en koelen van moleculen. Dit proefschrift laat een experimentele opstelling zien die ontworpen is om de limieten van het Standaardmodel te testen. Deze testen kunnen worden gedaan met precisiemetingen en voor de ultieme precisie is een goede controle over de moleculen vereist. In ons experiment combineren we een lopendegolf-Starkafremmer met laserkoeling om ultrakoude moleculen te verkrijgen. We gebruiken het molecuul SrF omdat dit zwaar genoeg is om het Standaardmodel te testen, maar ook licht genoeg om tot stilstand af te remmen in een 5 meter lange afremmer. Ook is SrF laserkoelbaar. Een onderzoek naar de krachtige combinatie van deze technieken is het hoofdonderwerp van dit proefschrift. Onze experimentele opstelling is drieledig van aard: eerst produceren we de moleculen, vervolgens remmen we ze af om ze ten slotte ultrakoud te maken voor de precisiemetingen.

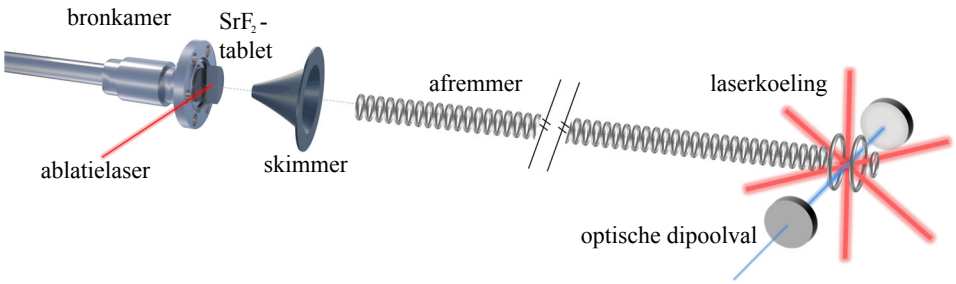

Figuur 7.1: *Een schematische weergave van ons experiment. Een SrF_2-tablet wordt lokaal verhit zodat o.a. SrF wordt gevormd. Via een supersonische expansie komen moleculen in de Starkafremmer alwaar de moleculen worden afgeremd door middel van elektrische velden. Aan het eind worden de moleculen verder afgekoeld met laserlicht.*

Moleculen worden geproduceerd in de bronkamer, waar een tablet SrF_2 lokaal sterk wordt verhit door een intense gepulste Nd:YAG-laser. Hierbij wordt onder andere SrF gevormd. Door een supersonische expansie met xenongas uit een gepulste klep worden de SrF moleculen gekoeld in de laagste rovibrationele toestanden en krijgen ze een voorwaartse snelheid van ~ 300 m/s naar de afremkamer. De lopendegolf-Starkafremmer gebruikt elektrische velden en het elektrisch dipoolmoment van de moleculen om een fractie van de moleculen tot stilstand af te remmen. Het wolkje afgeremde moleculen heeft een snelheidsverdeling die overeenkomt met een temperatuur van 12 mK. Laserkoeling kan de moleculen nog verder afkoelen. Figuur 7.1 toont een schematische weergave van het experiment. De afgelopen jaren heeft onze groep een vier meter lange molecuulafremmer ontworpen en gebouwd. De afremmer bestaat uit duizenden ring-elektrodes met een diameter van 4 mm die perfect in één lijn met elkaar staan. Een module van 50 cm is te zien in Figuur 7.2.

Door een elektrische hoogspanning op de verschillende elektroden te zetten worden minima en maxima in het elektrische veld tussen de ringen gecreëerd. Een deel van de moleculen met een elektrisch dipoolmoment verliest energie als het uit een minimum van het elektrisch veld komt. Deze moleculen zitten in een laagveldzoekende toestand. Door de spanning te variëren

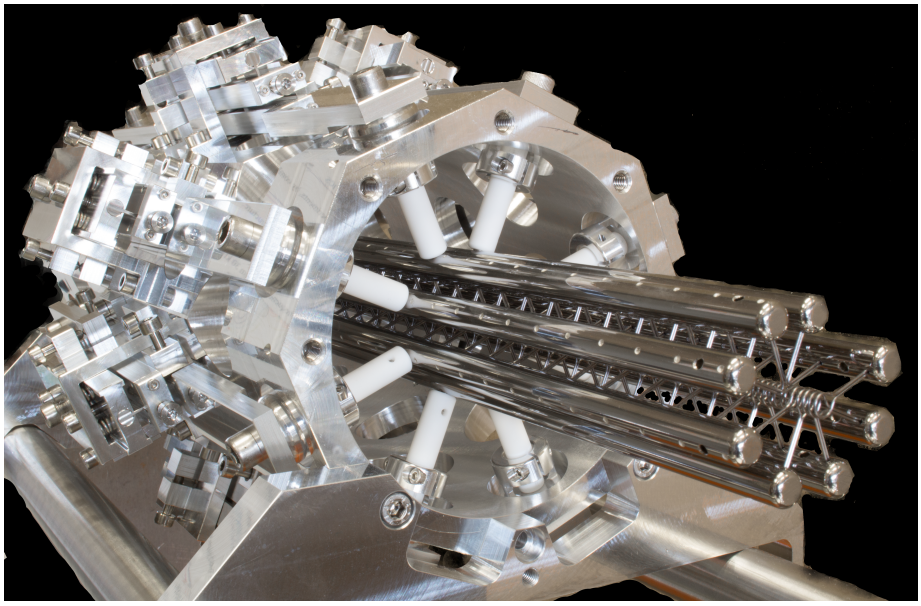

Figuur 7.2: *Een van de modules in de afremmer. De module bevat 42 ringelektrodes en heeft een lengte van 50 cm.*

worden de veldminima door de afremmer bewogen: ze beginnen met dezelfde snelheid als de moleculen (300 m/s) en worden vervolgens afgeremd. Hierbij worden ook de ingevangen moleculen afgeremd.

Als het wolkje moleculen is afgeremd tot stilstand is de temperatuur nog ongeveer 12 mK. Door de moleculen te laserkoelen kan de temperatuur verder naar beneden worden gebracht. Het laserkoelen van atomen wordt al enkele decennia gedaan. Moleculen zijn moeilijker om te laserkoelen omdat er geen gesloten transitie is bij de vibrationele toestanden. Toch zijn er moleculen die laserkoelbaar zijn. Deze moleculen hebben maar een kleine kans om naar hogere vibrationele toestanden te vervallen. Rotationeel kan het systeem gesloten worden door pariteits- en selectieregels. Hierdoor kunnen alle nodige transities gemaakt worden met een beperkt aantal lasers. Voor SrF en andere aardalkali-monohaliden wordt de rotationele $N = 1, J = 1/2, 3/2 \rightarrow J' = 1/2$ overgang gebruikt. Doordat de moleculen na de afremmer al een vrij lage relatieve snelheid hebben (~ 2 m/s) zijn er slechts een paar honderd verstrooiingen nodig voor het berei-

ken van de Dopplertemperatuur. Hierdoor is er slechts één terugpomplaser nodig.

Er zijn bepaalde uitdagingen voor het laserkoelen van moleculen. De laserkoelcyclus van SrF heeft 4 hyperfijntoestanden in de aangeslagen toestand en als we slechts één terugpomplaser gebruiken zijn er 24 hyperfijntoestanden in de grondtoestand. Dit betekent dat het effectieve verstrooiingstempo is gereduceerd tot 2/7 ten opzichte van een tweeniveausysteem. Ook is het kwantumgetal van het impulsmoment hoger in de grondtoestand ($F = 2$) dan in de aangeslagen toestand ($F = 1$). Dit zorgt voor toestanden die niet kunnen worden aangeslagen door lineair of circulair gepolariseerd laserlicht. Dit kan worden verholpen door een magneetveld aan te leggen bij lineair gepolariseerd licht of door snel te schakelen tussen tussen de twee tegenovergestelde circulaire polarisaties. Beide manieren maken het laserkoelen iets minder efficiënt.

In dit proefschrift is een model gebruikt dat de interacties van moleculen met laserlicht beschrijft (hoofdstuk 3). Een groot voordeel van de combinatie van laserkoeling met een afremmer is dat de beginsnelheid voor het laserkoelen al erg laag is, ~ 2 m/s. Met het model hebben we berekend dat het koelen ongeveer 1 ms duurt als we 10 mW laserlicht per hyperfijnovergang gebruiken en een $1/e^2$-bundeldiameter van 40 mm. Dit resulteert in een verstrooiing van $\sim 3 \times 10^3$ fotonen. Met alleen een pomplaser is het verlies naar de hogere orde vibrationele toestanden 7.2 %. Hierbij is alleen gekeken naar de snelheidsafhankelijke kracht, niet naar een plaatsafhankelijkheid, zoals in een magnetisch-optische val (MOT).

Om het laserkoelen met de afremmer te combineren is een elektrische val ontworpen waar plaats is voor laserbundels (hoofdstuk 4). Deze val kan gebruikt worden voor zowel 2D als 3D laserkoeling en er is ook ruimte voor een optische dipoolval.

De afremmer remt alleen moleculen in de laagveldzoekende toestand af. Voor de detectie en het laserkoelen gebruiken we de laagste rotationele toestand die laagveldzoekend is: $N = 1$. Deze toestand bevat twaalf hyperfijne subniveaus, waarvan er slechts vier laagveldzoekend zijn. Het aantal moleculen in de laagveldzoekende toestanden kan worden vergroot door middel

van optisch pompen. Moleculen in hoogveldzoekende toestanden worden aangeslagen met laserlicht en kunnen vervallen naar laagveldzoekende toestanden. In hoofdstuk 5 bestuderen we experimenteel en met behulp van simulaties de optimale condities voor dit proces. Hieruit blijkt dat het aantal moleculen in de laagveldzoekende toestanden met een factor 1,5 verhoogd kan worden.

7.1 Vooruitblik

Simulaties en metingen met een afremmer van 2 meter wijzen uit dat moleculen kunnen worden gestopt met een afremmer van 4,5 meter. De laatste module en de elektrische val zijn gemonteerd en kunnen achter de huidige afremmer van 4 meter geplaatst worden.

Naast de afremmer hebben we een extra bron- en detectiekamer om de hoeveelheid moleculen in de $v = 0, N = 1$ toestand te optimaliseren. De supersonische expansie wordt geanalyseerd voor experimenten met een SrF_2-staaf en met een Sr-staaf en SF_6-gas gemixt met het draaggas. Ook wordt er onderzoek gedaan naar een cryogene buffergascel. De tweede bronkamer kan ook worden gebruikt om andere moleculen te onderzoeken voor toekomstige experimenten.

Met laserkoeling naar een optische dipoolval

In hoofdstuk 3 laten we simulaties zien van laserkoeling van SrF-moleculen aan het eind van de afremmer. Hierbij wordt alleen de dopplerverschuiving van het licht gebruikt om de moleculen te koelen. De kracht is onafhankelijk van de positie van de moleculen en dit resulteert in een vrij groot volume waarover de moleculen zijn verspreid ($\sim 2.6 \times 4.0 \times 4.0$ mm^3). Om de moleculen in een optische dipoolval te vangen moet het wolkje moleculen kleiner zijn ($\sim 500\mu$m $\times$ 2 mm). Een optie om zoveel mogelijk moleculen te vangen is om de elektrische val nog een keer aan te zetten zodat alle laagveldzoekende moleculen weer worden aangetrokken tot het centrum. Als de elektrische val harmonisch is, zijn alle moleculen op een bepaald tijdstip relatief dicht bij elkaar. Wordt de val dan uitgezet en het laserkoelen weer gestart dan kunnen de moleculen wordensamengebracht in een klein volume. Het faseruimtediagram van dit proces is schematisch te zien in Figuur 7.3.

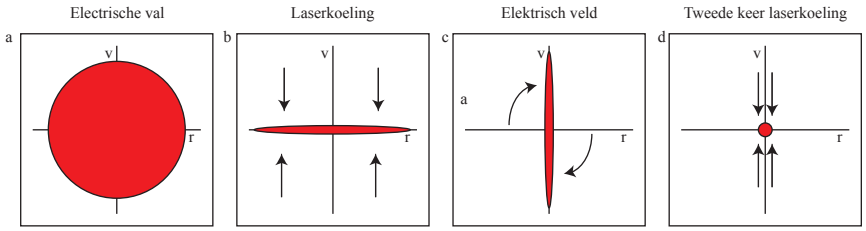

Figuur 7.3: *Eem schematisc faseruimtediagram van de moleculen a) na de elektrische val, b) het laserkoelen, c) als de elektrische val weer aan is en d) de tweede keer laserkoelen.*

Een langzame, koude molecuulbundel voor precisiemetingen

In dit proefschrift beschrijven we een experiment dat profiteert van de combinatie van afremmen en laserkoelen. Op deze manier hebben we goede controle over zowel de interne als externe vrijheidsgraden van de moleculen. De afremmer reduceert de snelheid van de molecuulbundel en laserkoeling vermindert de temperatuur van de moleculen naar ongeveer 1 mK in een beperkte hoeveelheid fotonverstrooiingen.

Recent is aangetoond dat de productie van molecuulbundels in een cryogene buffergascel leidt tot een lagere aanvangssnelheid en hogere molecuuldichtheid in vergelijking met onze supersonische expansie. Dit type bron produceert erg lange pulsen van moleculen die typisch niet goed overlappen met één enkel potentiaalminimum in de afremmer. Daardoor kunnen deze bronnen beperkt gebruikt worden voor het koelen en invangen in een optische dipoolval.

In dit proefschrift hebben we onderzocht hoe de combinatie van een lopendegolf-Starkafremmer met laserkoelen in de transversale richtingen resulteert in een langzame, intense molecuulbundel die transversaal ultrakoud is. Zulke molecuulbundels effenen het pad voor experimenten met een lange coherente interactietijd zonder dat ingeleverd wordt op het grote aantal moleculen. Deze technieken zijn veelbelovend voor de volgende generatie van precisie-experimenten om het Standaardmodel te testen.

Dankwoord

Ik heb de afgelopen jaren met plezier gewerkt in het team van de koude moleculen aan het bouwen van de molecuulafremmer. Het was ontzettend leuk om te zien dat de moleculen eerst door de afremmer worden geleid en daarna steeds verder werden afgeremd! Dit hele project had natuurlijk nooit gekund zonder goed samen te werken met verschillende mensen.

Allereerst wil ik mijn promotor Steven bedanken voor de fijne samenwerking en alle hulp en begeleiding. Je wist altijd de juiste vragen te stellen als ik ergens in vast liep. Vaak kwam ik daarna weer een stukje dichter bij het antwoord.

Daarnaast wil ik ook Klaus, mijn tweede promotor, bedanken voor alle adviezen en enorme kennis van de natuurkunde. Klaus, ook al heb je het altijd druk, de deur stond toch altijd open voor vragen.

Natuurlijk wil ik ook meneer Leo bedanken, niet alleen voor je praktische oplossingen en technische hulp maar ook voor je optimisme, de gezelligheid, je altijd gevulde dropjespot en de lekkere appeltaart.

De afremmer was nooit gebouwd zonder hulp van Imko 'de directeur' Smid en de (tovenaars van de) werkplaats. Imko, André, Sandra, Roelof, Dirk, Henk en Nanko: bedankt voor alle keren dat we eigenlijk gisteren iets nodig hadden en jullie het heel snel konden maken.

Lorenz, bedankt voor je hulp en kennis over de lasers.

Ik wil graag mijn medepromovendi van de koude moleculen, Joost, Sreekanth, Artem en Kevin, bedanken voor de fijne samenwerking. Ik hoop dat jullie in de toekomst nog vele moleculen mogen afremmen, en natuurlijk dat ze op een dag stil komen te staan! Ook is er natuurlijk veel hulp geweest van alle studenten: Samuel, Nathan, Aernout, Tom, Janko, Peter, Jonathan, Joram, Joël, Roel en alle Fransozen. Naast de koude moleculen

heb ik ook veel geleerd van de rest van de Trimp- en later de FIS-groep: Duurt, Oscar, Wilbert, Gouri, Bodha, Mayerlin, Elwin, Amita, Olivier, Nivedya, Auke, Stefan, Otto, Oliver en Andrew.

Ik wil graag computergoeroes Elwin en Joost bedanken voor het helpen bij al mijn "computeruitdagingen". Gerco, jou hoef ik hiervoor niet te bedanken aangezien jij gewoon wordt betaald voor wat je doet. Maar misschien kan ik je toch bij voorbaat bedanken voor de moorkop die ik nu van je krijg :)

Hilde, bedankt voor het regelen van alle administratieve dingen.

Rob Timmermans en Marjan Koopmans wil ik graag bedanken voor de uitstekende organisatie van de FANTOM-weken.

Ik wil natuurlijk ook mijn 'roomies' bedanken voor alle gezelschap, vooral als het wat later op de dag werd: Jordy, Bodha, Olivier, Mayerlin, Janko, Peter, Tom en Faruk. En mijn wandelmaatjes tijdens de lunchpauzes: Boschman, Geri en Keert, Elwin en Joost. En Harry Timersma voor alle levenswijsheden.

Ik wil bij voorbaat mijn paranimfen Keri en Elwin bedanken voor het in goede banen leiden van de verdediging en de oerdegelijke presentatie die ze daarna gaan geven.

Ik wil alle mensen van het KVI bedanken voor de ondersteuning en vooral voor de ontzettend fijne tijd.

I would like to thank the members of the reading committee, Ad van den Berg, Beatriz Noheda and Peter van der Straten, for reading my thesis and giving suggestions for improvements.

Mijn ouders wil ik bedanken voor alle mogelijkheden die ik van hen heb gekregen om te studeren

Als laatste wil ik mijn lieve oud-collega en huisgenoot Joost bedanken voor alle steun, hulp, fijne samenwerking, alle maaltijden als ik weer eens te laat thuis kwam en vertrouwen dat het allemaal goed zou komen. Ik weet niet of het zonder jou wel gelukt was en ik hoop ook nog heel lang je huisgenoot te blijven, waar dat ook maar mag zijn. En dankzij jou is mijn voorkant nog mooier geworden.

List of publications

A. Sytema, J.E. van den Berg, O. Böll, D. Chernowitz, E.A. Dijck, J.O. Grasdijk, S. Hoekstra, K. Jungmann, S.C. Mathavan, **C. Meinema**, A. Mohanty, S.E. Müller, M. Nuñez Portela, C.J.G. Onderwater, C. Pijpker, L. Willmann, H.W. Wilschut. A gas cell for stopping, storing and polarizing radioactive particles. Nuclear Instruments and Methods in Physics Research A **822**, 77–81 (2016).

J.E. van den Berg, S.C. Mathavan, **C. Meinema**, J. Nauta, T.H. Nijbroek, K. Jungmann, H.L. Bethlem, S. Hoekstra (2014). Traveling-wave deceleration of SrF molecules. Journal of molecular spectroscopy **300**, 22-25.

I. Blank, S. Otranto, **C. Meinema**, R.E. Olson, & R. Hoekstra. Angular differential studies of electron transfer in collisions of He-like ions with Na(3s): The role of electron saddle crossings. Physical Review A **87** (3), [032712] (2013).

S.E. Müller, E.A. Dijck, H. Bekker, J.E. van den Berg, O. Böll, S. Hoekstra, K. Jungmann, **C. Meinema**, J.P. Noordmans, M. Nuñez Portela, C.J.G. Onderwater, C. Pijpker, A.P.P. van der Poel, B. Santra, A. Sytema, R.G.E. Timmermans, O.O. Versolato, L. Willmann, H.W. Wilschut, and K. Yai. First test of Lorentz invariance in the weak decay of polarized nuclei. Physical Review D **88** (7), [071901] (2013).

I. Blank, S. Otranto, **C. Meinema**, R.E. Olson, & R. Hoekstra. State-selective electron transfer and ionization in collisions of highly charged ions with ground-state Na(3s) and laser-excited Na*(3p). Physical Review A **85** (2), [022712] (2012).

Bibliography

[1] S.L. Glashow, Rev. Mod. Phys. 52, **539**, (1980).
[2] S.L. Glashow, Nucl. Phys. **22**, 579 (1961).
[3] S. Weinberg, Phys. Rev. Lett. **19**, 1264 (1967).
[4] A. Salam, N. Svartholm, ed. Elementary Particle Physics: Relativistic Groups and Analyticity. Eighth Nobel Symposium. Stockholm: Almquvist and Wiksell (1968).
[5] M.J.G. Veltman, Rev. Mod. Phys. **72**, 341 (2000).
[6] G.'t Hooft, Nucl. Phys. B **33**, 173 (1971).
[7] K. Becker, M. Becker, J.H. Schwarz, String theory and M-theory: A modern introduction. Cambridge University Press. (2007).
[8] N. Fortson, P.G.H. Sandars, S. Barr, Physics Today **56**, 33 (2003);
[9] W. Bernreuther and M. Suzuki, Rev. Mod. Phys. **63**, 313 (1991); Erratum Rev. Mod. Phys. **64**, 633 (1992).
[10] K. Jungmann, Annalen der Physik **525**, 550 (2013).
[11] B.L. Roberts and W.J. Marciano (eds.), 'Lepton Dipole Moments', World Scientific (2009).
[12] J.J. Hudson, D.M. Kara, I.J. Smallman, B.E. Sauer, M.R. Tarbutt, and E.A. Hinds, Nature (London) **473**, 493 (2011).
[13] The ACME Collaboration, J. Baron, W.C. Campbell, D. DeMille, J.M. Doyle, G. Gabrielse, Y.V. Gurevich, P.W. Hess, N.R. Hutzler, E. Kirilov, I. Kozyryev, B.R. O'Leary, C.D. Panda, M.F. Parsons, E.S. Petrik, B. Spaun, A.C. Vutha, A.D. West, Science **343**, 269 (2014).
[14] A. Salam, Rev. Mod. Phys. **52**, 525 (1980).
[15] C.S. Wu, E. Ambler, R.W. Hayward, D.D. Hoppes, and R.P. Hudson, Phys. Rev. **105**, 1413 (1957).
[16] M.A. Bouchiat and C.C. Bouchiat, Phys. Lett B **48**, 111 (1974).
[17] C.S. Wood, S.C. Bennett, D. Cho, B.P. Masterson, J.L. Robers, C.E. Tanner, C.E. Wieman, Science **275**, 1759 (1997).
[18] V.V. Flambaum and I.B. Khriplovich, Sov. Phys. JETP **52**, 835 (1980).
[19] D. DeMille, S.B. Cahn, D. Murphree, D.A. Rahmlow, and M.G. Kozlov, Phys. Rev. Lett. **100**, 023003 (2008).
[20] L.D. Carr, D. DeMille, R.V. Krems and J. Ye, New J. Phys. **11**, 055049 (2009).
[21] L.W. Wansbeek, PhD thesis, University of Groningen (2011).
[22] L.W. Wansbeek, B.K. Sahoo, R.G.E. Timmermans, K. Jungmann, B.P. Das, and D. Mukherjee, Phys. Rev. A **78**, 050501(R) (2008).

[23] O. Versolato, L. Wansbeek, G. Giri, J.E. van den Berg, D.J. van der Hoek, K.P. Jungmann, W. Kruithof, C.J.G. Onderwater, B.K. Sahoo, B. Santra, P. Shidling, R.G.E. Timmermans, L. Willmann and H.W.E.M. Wilschut, Can. J. Phys **89**, 65 (2011).
[24] V.V. Flambaum, Sov. J. Nucl. Phys. **24**, 199 (1976).
[25] A.V. Titov, N.S. Mosyagin, A.N. Petrov, T.A. Isaev, and D. DeMille, Recent Advances in the Theory of Chemical and Physical Systems, Progress in Theoretical Chemistry and Physics, **15**, II, 253-283 (2006).
[26] A.T. Nguyen, D. Budker, D. DeMille, and M. Zolotorev, Phys. Rev. A **56**, 3453 (1997).
[27] S.B. Cahn, J. Ammon, E. Kirilov, Y.V. Gurevich, D. Murphree, R. Paolino, D.A. Rahmlow, M.G. Kozlov, and D. DeMille, Phys. Rev. Lett. **112**, 163002 (2014).
[28] R.A. Hegstrom, D.W. Rein, P.G.H. Sandars, J. Chem. Phys. **73**, 2329 (1980).
[29] R. Berger, Theoretical and Computational Chemistry, chapter 4, 2009.
[30] M. Quack, Angew. Chem. Int. Ed. **41**, 4618 (2002).
[31] P. Frank, W.A. Bonner, R.N. Zare, in: E. Keinan, I. Schecher (ed.), Chemistry for the 21st Century, Wiley-VCH, Weinheim, Chapter 11, p 175 (2001).
[32] W.L. Noordduin, E. Vlieg et al., Nature Chemistry **1**, 729 (2009).
[33] A. Bakasov, T.K. Ha, M. Quack, J. Chem. Phys. **109**, 7263 (1998).
[34] G.E. Harrison, P.G.H. Sandars, and S.J. Wright, Phys. Rev. Lett. **22**, 1263 (1969); Erratum Phys. Rev. Lett. **23**, 274 (1969).
[35] D.N. Gresh, K.C. Cossel, Y. Zhou, J. Ye, E.A. Cornell, J. of Mol. Spec. **319**, 1 (2016).
[36] P.G.H. Sandars, in Atomic Physics 4, Eds. G. zu Putlitz, E.W. Weber, and A. Winnacker, p71 - 103, Plenum Press, New York (1975).
[37] M.R. Tarbutt, B.E. Sauer, J.J. Hudson and E.A. Hinds, New J. of Phys. **15**, 053034 (2013).
[38] http://gabrielse.physics.harvard.edu/gabrielse/overviews/ElectronEDM/Electron EDM.html.
[39] C. Chin, V.V. Flambaum and M.G. Kozlov, New J Phys **11**, 055048 (2009).
[40] J.P. Uzan, Living Rev. Relativ. **14**, 2 (2011).
[41] S. Ray, U. Mukhopadhyay, P. P. Ghosh, arXiv:0705.1836 (2007).
[42] M. Quintero-Pérez, P. Jansen, T.E. Wall, J.E. van den Berg, S. Hoekstra, H.L. Bethlem, Phys. Rev. Lett. **110**, 133003 (2013).
[43] P. Jansen, M. Quintero-Pérez, T.E. Wall, J.E. van den Berg, S. Hoekstra, H.L. Bethlem, Phys. Rev. A **88**, 043424 (2013).
[44] J.E. van den Berg, PhD thesis, University of Groningen 2015.
[45] E.S. Shuman, J.F. Barry, D.R. Glenn, and D. DeMille, Phys. Rev. Lett. **103**, 223001 (2009).
[46] E.B. Norrgard, D.J. McCarron, M.H. Steinecker, M.R. Tarbutt, D. DeMille, Phys. Rev. Lett. **116**, 063004 (2016) ; see also references therein.
[47] W. Ketterle and D.E. Pritchard, Phys. Rev. A **46**, 4051 (1992).
[48] J.E. van den Berg, S.H. Turkesteen, E.B. Prinsen, S. Hoekstra, Eur. Phys. J. D, **66** 9, 235 (2012).
[49] D.M. Kara, I.J. Smallman, J.J. Hudson, B.E. Sauer, M.R. Tarbutt and E.A. Hinds, New J. Phys. **14**, 103051 (2012).

[50] S. Eckel, P. Hamilton, E. Kirilov, H.W. Smith, and D. DeMille, Phys. Rev. A **87**, 052130 (2013).
[51] T.A. Isaev, S. Hoekstra, R. Berger, Phys. Rev. A **82**, 052521 (2010).
[52] M. Quintero-Pérez, PhD thesis, VU University Amsterdam (2014).
[53] J.F. Barry, E.S. Shuman, E.B. Norrgard, and D. DeMille, Phys. Rev. Lett. **108**, 103002 (2012).
[54] H.L. Bethlem, G. Berden and G. Meijer, Phys. Rev. Lett. **83**, 1558 (1999).
[55] A. von Zastrow, J. Onvlee, S.N. Vogels, G.C. Groenenboom, A. van der Avoird, and S.Y.T. van de Meerakker, Nature Chemistry **6**, 216 (2014).
[56] J.R. Bochinski, E.R. Hudson, H.J. Lewandowski, G. Meijer and J. Ye, Phys. Rev. Lett. **91**, 243001 (2003).
[57] J.E. van den Berg, S.C. Mathavan, C. Meinema, J. Nauta, T.H. Nijbroek, K. Jungmann, H.L. Bethlem, S. Hoekstra, J. Mol. Spectr. **300**, 22 (2014).
[58] N.E. Bulleid, R.J. Hendricks, E.A. Hinds, S.A. Meek, G. Meijer, A. Osterwalder, M.R. Tarbutt, Phys.l Rev. A **86**, 021404(R) (2012).
[59] J. Doyle, B. Friedrich, R.V. Krems, and F. Masnou-Seeuws, Eur. Phys. J. D **31**, 149 (2004).
[60] G. Sanna and G. Tomassetti, *Introduction to Molecular Beams Gas Dynamics*, Imperial College Press, (2005).
[61] S.E. Maxwell, N. Brahms, R. deCarvalho, D.R. Glenn, J.S. Helton, S.V. Nguyen, D. Patterson, J. Petricka, D. DeMille and J. M. Doyle, Phys. Rev. Lett. **95**, 173201 (2005).
[62] D. Patterson and J.M. Doyle, Phys. Chem. Chem. Phys. **17**, 5372 (2015).
[63] L. Scharfenberg, H. Haak, G. Meijer, and S.Y.T. van de Meerakker, Phys. Rev. A **79**, 023410 (2009).
[64] S.Y.T. van de Meerakker, N. Vanhaecke, H.L. Bethlem, and G. Meijer, Phys. Rev. A **73**, 023401 (2006).
[65] S.Y.T. van de Meerakker, H.L. Bethlem, and G. Meijer, Nature Physics **4**, 595 (2008).
[66] C. Meng, A.P.P. van der Poel, C. Cheng, and H.L. Bethlem, Phys. Rev. A **92**, 023404 (2015).
[67] J.J. Gilijamse, S. Hoekstra, S.Y.T. van de Meerakker, G.C. Groenenboom and G. Meijer, Science, **313**, 1617 (2006).
[68] M. Kirste, X. Wang, H.C. Schewe, G. Meijer, K. Liu, A. van der Avoird, L.M.C. Janssen, K.B. Gubbels, G.C. Groenenboom, S.Y.T. van de Meerakker, Science **338**, 6110 (2012).
[69] A. Osterwalder, S.A. Meek, G. Hammer, H. Haak, G. Meijer, Phys. Rev. A **81**, 051401(R) (2010).
[70] S.A. Meek, M.F. Parsons, G. Heyne, V. Platschkowski, H. Haak, G. Meijer, A. Osterwalder, Rev. Sci. Instrum. **82** 093108 (2011).
[71] N. Vanhaecke, U. Meier, M. Andrist, B.H. Meier, and F. Merkt, Phys. Rev. A **75**, 031402(R) (2007).
[72] K. Dulitz, A. Tauschinsky, T.P. Softley, arXiv:1501.04589 (2015).
[73] E. Narevicius, A. Libson, C.G. Parthey, I. Chavez, J. Narevicius, U. Even, and M.G. Raizen, Phys. Rev. A **77**, 051401 (2008).

[74] A. W. Wiederkehr, H. Schmutz, M. Motsch, and F. Merkt, Mol. Phys. **110**, 1807 (2012).
[75] T. Momose, Y. Liu, S. Zhou, P. Djuricanin, and D. Carty, Phys. Chem. Chem. Phys. **15**, 1772 (2013).
[76] M.H. Anderson, J.R. Ensher, M.R. Matthews, C.E. Wieman and E.A. Cornell, Science **269**, 198 (1995)
[77] M.D. DiRosa, Eur. Phys. J. D **31**, 395 (2004).
[78] B.K. Stuhl, B.C. Sawyer, D. Wang, and J. Ye, Phys. Rev. Lett. **101**, 243002 (2008).
[79] E.S. Shuman, J.F. Barry and D. DeMille, Nature **467**, 820 (2010).
[80] M.T. Hummon, M. Yeo, B.K. Stuhl, A.L. Collopy, Y. Xia, and J. Ye, Phys. Rev. Lett. **110**, 143001 (2013).
[81] V. Zhelyazkova, A. Cournol, T.E. Wall, A. Matsushima, J.J. Hudson, E.A. Hinds, M.R. Tarbutt, and B.E. Sauer, Phys. Rev. A **89**, 053416 (2014).
[82] J.F. Barry, D.J. McCarron, E.B. Norrgard, M.H. Steinecker and D. DeMille, Nature **512**, 286 (2014).
[83] D.J. McCarron, E.B. Norrgard, M H. Steinecker, D. DeMille, New J. Phys. **17**, 035014 (2015).
[84] E. Narevicius, S.T. Bannerman, & M.G. Raizen, N. J. Phys. **11**, 055046 (2009).
[85] J. Riedel, S. Hoekstra, W. Jäger, J.J. Gilijamse , S.Y.T. van de Meerakker, and G. Meijer, Eur. Phys. J. D **65** 161, (2011).
[86] M. Zeppenfeld, B.G.U. Englert, R. Glöckner, A. Prehn, M. Mielenz, C. Sommer, L.D. van Buuren, M. Motsch, G. Rempe, Nature **491**, 570 (2012).
[87] J.F. Barry and D. DeMille, Nature **491**, 539 (2012).
[88] S.K. Tokunaga, W. Skomorowski, P.S. Żuchowski, R. Moszynski, J.M. Hutson, E.A. Hinds and M.R. Tarbutt, Eur. Phys. J. D **65**, 141 (2011).
[89] P. Soldan, P.S. Żuchowski and J.M. Hutson, Faraday Discuss., **142**, 191 (2009).
[90] J. Lim, M.D. Frye, J.M. Hutson, and M.R. Tarbutt, Phys. Rev. A **92**, 053419 (2015).
[91] B.K. Stuhl, M.T. Hummon, M. Yeo, G. Quéméner, J.L. Bohn & J. Ye, Nature **492**, 396 (2012).
[92] S. Ospelkaus, K.-K. Ni, M.H.G. de Miranda, B. Neyenhuis, D. Wang, S. Kotochigova, P.S. Julienne, D.S. Jin and J. Ye, Faraday Discuss. **142**, 351 (2009).
[93] K.-K. Ni, S. Ospelkaus, M.H.G. de Miranda, A.Pe'er, B. Neyenhuis, J.J. Zirbel, S. Kotochigova, P.S. Julienne, D.S. Jin, J. Ye, Science **322**, 231 (2008).
[94] B. Roth and S. Schiller, in: R.V. Krems, B. Friedrich and W.C. Stwalley (ed.) *Cold Molecules:Creation and Applications*, Boca Raton, FL:CRC Press (2009).
[95] S. Willitsch, Nature Physics **6**, 240 (2010) .
[96] J.H.V. Nguyen, C.R. Viteri, E.G. Hohenstein, C.D. Sherrill, K.R. Brown, and B. Odom, New J. Phys. **13**, 063023 (2011).
[97] A. Borschevsky, M. Iliaš, V.A. Dzuba, K. Beloy, V.V. Flambaum and P. Schwerdtfeger, Phys. Rev. A **86**, 050501(R) (2012).
[98] J. Onvlee, S.N. Vogels, A. von Zastrow, D.H. Parker, and S.Y.T. van de Meerakker, Phys. Chem. Chem. Phys. **16**, 15768 (2014).
[99] G. Quéméner and P.S. Julienne, Chem. Rev. **112**, 4949 (2012).
[100] C. Trefzger, C. Menotti, B. Capogrosso-Sansone, and M. Lewenstein, J. Phys. B: At., Mol. Opt. Phys. **44**, 193001 (2011).
[101] J. Nauta, Master thesis, University of Groningen (2014).

[102] J. Brown and Alan Carrington, Rotational Spectroscopy of Diatomic Molecules, Cambridge Molecular Science, Cambridge University press 2003.
[103] W. Demtröder, Molecular Physics. Theoretical Prinstiples and Experimental Methods, Wiley-VCH Verlag GmbH&Co. KGaA, Weinheim 2005.
[104] G. Herzberg, Molecular Spectra and Molecular Structrue - Vol 1, D. Van Nostrand Company, INC 1950
[105] A.T. Le, H. Wang and T.C. Steimle, Phys. Rev. A **80**, 062513 (2009).
[106] J.J. Metcalf and P. van der Straten, Laser cooling and trapping, Springer-Verlag, 1999.
[107] L.B. Knight Jr., W.C. Easley, W. Weltner Jr. and M. Wilson, J. Chem. Phys. **54**, 322 (1971).
[108] J.F. Barry, PhD thesis, Yale University, webversion (2013).
[109] R.J. Hendricks, D.A. Holland, S. Truppe, B.E. Sauer, M.R. Tarbutt, Front. Phys **2**, 51 (2014).
[110] Y. Gao and T. Gao, Phys. Chem. Chem. Phys. **17**, 10830 (2015).
[111] N. Wells and I.C. Lane Phys. Chem. Chem. Phys., **13**, 19018 (2011).
[112] C.J. Foot, Atomic Physics, Oxford University Press 2005.
[113] M.R. Tarbutt, New J. Phys **17**, 015007 (2015).
[114] W.E. Ernst, J. Kändler, S. Kindt, T. Törring, Chem. Phys. Lett. **113**, 351 (1985).
[115] Y. Azuma, W.J. Childs, G.L. Goodman and T.C. Steimle, J. Chem. Phys. **93**, 5533 (1990).
[116] http://pgopher.chm.bris.ac.uk
[117] G. Grynberg, A. Aspect, C. Fabre, An Introduction to Quantum Optics: From the Semi-classical Approach to Quantized Light, Cambridge University Press (2010).
[118] R. Höppner, E. Roldán and G.J. de Valcárcel, Am. J. Phys. **80**, 882 (2012).
[119] D. Budker, D.F. Kimball, D.P. DeMille, Atomic physics: An exploration through problems and solutions, Oxford university press 2004.
[120] T.E. Wall, J.F. Kanem, J.J. Hudson, B.E. Sauer, D. Cho, M.G. Boshier, E.A. Hinds and M.R. Tarbutt, Phys. Rev A **78**, 062509 (2008).
[121] D.J. Berkeland, M.G. Boshier, Phys. Rev. A **65**, 033413 (2002).
[122] V. Zhelyazkova, PhD thesis, Imperial college London (2014).
[123] P.J. Dagdigian, H.W. Cruse, R.N. Zare, J. Chem. Phys. **60**, 230 (1974).
[124] L.-E. Berg, N. Gador, D. Husain, H. Ludwigs, and P. Royen, Chem. Phys. Lett. **287**, 89 (1998).
[125] T.C. Steimle, S. Frey, A. Le, D. DeMille, D.A. Rahmlow, and C. Linton, Phys. Rev. A **84**, 012508 (2011).
[126] B. Karthikeyan, K. Balachandrakumar, V. Raja and N. Rajamanickam, J. Appl. Spectrosc. **80**, 790 (2013).
[127] A.P.P. van der Poel, Master thesis, University of Groningen (2012).
[128] S. Hoekstra et al., Proposal for an eEDM experiment using a cold, slow and intense beam of BaF molecules, (2016).
[129] T.H. Nijbroek, Master thesis, University of Groningen (2013).
[130] D. Comparat, Phys. Rev. A **89**, 043410 (2014).
[131] Private communication, M. Tarbutt.
[132] M.A. Chieda and E.E. Eyler, Phys. Rev. A **84**, 063401 (2011).
[133] E. Ilinova, J. Weinstein and A. Derevianko, New J. Phys **17**, 055003 (2015).

[134] A.L. Collopy, M.T. Hummon, M. Yeo, B. Yan, J. Ye, New J. Phys **17** 055008 (2015).
[135] I.C. Lane, Phys. Chem. Chem. Phys., **14**, 15078 (2012).
[136] T. Wentink and R.J. Spindler, J. Quant. Spectrosc. Radiat. Transfer. **10**, 609 (1970).
[137] http://webbook.nist.gov/chemistry/
[138] Y. Gao and T. Gao, Phys. Rev. A **90**, 052506 (2014).
[139] L.-E. Berg, L. Klynning, Phys. Scr. **10**, 331 (1974)
[140] M. Liu, T. Pauchard, M. Sjödin, O. Launila, P. van der Meulen, L.-E. Berg, J. Mol. Spectrosc., **257**, 105 (2009),
[141] M.V. Ramanaiah and S.V.J. Lakshman, Physica B+C **113**, 263 (1982).
[142] J.W.C. Johns, F.A. Grimm, and R.F. Porter, J. Mol. Spectrosc. **22**, 435 (1967).
[143] W.T.M.L. Fernando and P.F. Bernath, J. Mol. Spectrosc. **145**, 392 (1991).
[144] C.H. Douglass, H.H. Nelson, and J.K. Rice, J. Chem. Phys. **90**, 6940, (1989).
[145] P. Baltayan and O. Nedelec, J. Chem. Phys. **70**, 2399 (1979).
[146] M. Pelegrini, C.S. Vivacqua, O. Roberto-Neto, F.R. Ornellas, and F.B.C. Machado, Braz. J of Phys **35**, 950 (2005).
[147] Guntsch, Dissertation, Stockholm, 1939.
[148] I.J. Smallman, F. Wang, T.C. Steimle, M.R. Tarbutt, E.A. Hinds, J. Mol. Spectrosc. **300**, 3 (2014).
[149] F.A. Jenkins and A. Harvey, Phys. Rev. **39**, 922 (1932).
[150] X. Zhuang, A. Le, T.C. Steimle, N.E. Bulleid, I.J. Smallman, R.J. Hendricks, S.M. Skoff, J.J. Hudson, B.E. Sauer, E.A. Hinds, M.R. Tarbutt, Phys. Chem. Chem. Phys. **13**, 19013 (2011).
[151] L.R. Hunter, S.K. Peck, A.S. Greenspon, S. Saad Alam, and D. DeMille, Phys. Rev. A **85**, 012511 (2012).
[152] R. Yang, Y. Gao, B. Tang and T. Gao, Phys. Chem. Chem. Phys. **17**, 1900 (2015).
[153] M.L.P. Rao, D.V.K. Rao, P.T. Rao, Physica B+C **81**, 392 (1976).
[154] F.S. Ortenberg, V.B. Glasko, A.I. Dmitriev, Soviet Astronomy - AJ **8**, 258 (1964).
[155] P. Sriramachandran, S.P. Bagare, N. Rajamanickam, K. Balachandrakumar, Solar Physcis **252**, 267 (2008).
[156] K. Liu and J.M. Parson, J. Chem. Phys. **67**, 1814 (1977).
[157] K. Kobayashi, G.E. Hall, J.T. Muckerman, T.J. Sears, A.J. Merer, J. Mol. Spectrosc. **212**, 133 (2002).
[158] C. Lundevall, J. Mol. Spec. **191**, 93 (1998).
[159] T. Wentink, jr, R. Spindler, jr., J. Quant. Spectrosc. Radiat. Transfer. **12**, 1569 (1972).
[160] D.R. Yarkony, J. Chem. Phys. **91**, 4745 (1989).
[161] R.D. Kenner, A. Kaes, R.K. Browarzik, F. Stuhl, J. Chem. Phys. **91**, 1440 (1989).
[162] G.W. Funke, Z. Phys. **96**, 787 (1935).
[163] W.H. Smith and H.S. Liszt, J. Quant. Spectrosc. Radiat. Transfer. **11**, 45 (1971).
[164] A.E. Douglas, Can. J. Phys. **35**, 71 (1957).
[165] W. Bauer, K.H. Becker, R. Düren, C. Hubrich, R. Meuser, Chem. Phys. Lett. **108**, 560 (1984).
[166] E.H. Eyster, Phys. Rev. **51**, 1078 (1937).
[167] J.W.C. Johns, R.F. Barrow, Proc. Phys. Soc. **71**, 476 (1958).

[168] S. J. Davis and S. G. Hadley, Phys. Rev. A **14**, 1146 (1976).
[169] K.D. Carlson, E. Ludena, C.Moser, J. Chem. Phys. **43**, 2408 (1965).
[170] J.F. Barry, E.S. Shuman and D. DeMille, Phys. Chem. Chem. Phys. **13** 18936 (2011).
[171] S.N. Hoekman, Master thesis, University of Groningen/KVI (2011).
[172] M.F. Tu, J.J. Ho, C.C. Hsieh and Y.C. Chen, Rev. Sci. Instrum. **80**, 113111 (2009).
[173] B.G.U. Englert, M. Mielenz, C. Sommer, J. Bayerl, M. Motsch, P.W.H. Pinkse, G. Rempe, and M. Zeppenfeld, Phys. Rev. Lett. **107**, 263003 (2011).
[174] M. Quintero-Pérez, T.E. Wall, S. Hoekstra, H.L. Bethlem, J. Mol. Spectrosc. **300**, 112 (2014).
[175] V. Bagnato, D.E. Pritchard and D. Kleppner, Phys. Rev A **35**, 4354 (1987).
[176] D.M.S. Johnson, J.M. Hogan, S.-w. Chiow, and M.A. Kasevich, Optics letters **35**, 745 (2010).
[177] C.E. Rogers III, J.L. Carini, J.A. Pechkis, and P.L. Gould, Rev. Sci. Instrum. **82**, 073107 (2011).
[178] E.B. Prinsen, Master thesis, University of Groningen/KVI (2011).